

Copyright
by
Min Kyoo Kang
2010

**The Dissertation Committee for Min Kyoo Kang Certifies that this is the approved
version of the following dissertation:**

**SWELLING INDUCED DEFORMATION AND INSTABILITY OF
HYDROGELS**

Committee:

Rui Huang, Supervisor

Stelios Kyriakides

Krishnaswamy Ravi-Chandar

Chad M. Landis

Paul S. Ho

**SWELLING INDUCED DEFORMATION AND INSTABILITY OF
HYDROGELS**

by

Min Kyoo Kang, B.S., M.S.

Dissertation

Presented to the Faculty of the Graduate School of

The University of Texas at Austin

in Partial Fulfillment

of the Requirements

for the Degree of

Doctor of Philosophy

The University of Texas at Austin

August, 2010

Dedication

To my parents, Jae Won Kang and Keun Sook Lee

Acknowledgements

On completion of this dissertation, I owe my gratitude to the following people.

Foremost, I would like to express my sincere gratitude to my advisor, Dr. Rui Huang, for his teaching and guidance during my Ph.D. study. I have been very fortunate to work with him, with a positive attitude and a constant desire to explore new fields of study. I am honored to have Dr. Stelios Kyriakides, Dr. Krishnaswamy Ravi-Chandar, Dr. Chad M. Landis, and Dr. Paul S. Ho as the members of my Ph.D. committee, and I am grateful for their commitment and helps. I am also thankful to the faculty in Department of Aerospace Engineering and Engineering Mechanics for their outstanding teaching.

I would like to thank my friends, Yaoyu Pang, Se-hyuk Im, Haixia Mei, Sukkyu Ryu, Nicholas Bouklas, Changwan Kim, Jaeyoung Lim, Yannis Korkolis, Jonathan Niemczura, Han Tran, Seung Ryul Na, Hee Jae Lee, Hyun Wook Kang, Justin Olmanson and many others for making my graduate study a precious chapter of my life.

I cannot overstate how much I owe my gratitude to my parents and brother. They have been showing endless support and trust through my entire life. Without them, I could not be who I am now.

There is one person whom I should show my deepest gratitude, my old friend, Donna Eunkyung Chung. She has been more than just a friend. She has been giving me

peaceful consolation, support, and encouragement during Ph.D. study. She has been someone I can rely on.

I gratefully acknowledge the financial assistance from the National Science Foundation in support of my Ph.D. study.

Min Kyoo Kang

The University of Texas at Austin

August 2010

SWELLING INDUCED DEFORMATION AND INSTABILITY OF HYDROGELS

Publication No. _____

Min Kyoo Kang, Ph.D.

The University of Texas at Austin, 2010

Supervisor: Rui Huang

A hydrogel consists of a cross-linked polymer network and solvent molecules, capable of large, reversible deformation in response to a variety of external stimuli. In particular, diverse instability patterns have been observed experimentally in swelling hydrogels under mechanical constraints. The present study develops a general theoretical framework based on a variational approach, which leads to a set of governing equations coupling mechanical and chemical equilibrium conditions for swelling deformation of hydrogels, along with proper boundary conditions. A specific material model is employed for analytical and numerical studies, for which the nonlinear constitutive behavior of the hydrogel is derived from a free energy function combining rubber elasticity with a polymer solution theory. A finite element method is then developed and implemented as a user-defined material (UMAT) in the commercial package, ABAQUS. By numerical simulations, the effect of constraint on inhomogeneous swelling of substrate-attached

hydrogel lines is elucidated. It is found that crease-like surface instability occurs when the width-to-height aspect ratio of the hydrogel line exceeds a critical value.

Next, by considering a hydrogel layer on a rigid substrate, swell-induced surface instability is studied in details. A linear perturbation analysis is performed to predict the critical condition for onset of the surface instability. In contrast to previously suggested critical conditions, the present study predicts a range of critical swelling ratios, from about 2.5 to 3.4, depending on the material properties of the hydrogel system. A stability diagram is constructed with two distinct regions for stable and unstable hydrogels with respect to two dimensionless material parameters. Numerical simulations are presented to show the swelling process, with evolution of initial surface perturbations followed by formation of crease-like surface patterns. Furthermore, with combined swelling and mechanical compression, the stability analysis is extended to predict a general critical condition that unifies the swell-induced surface instability of hydrogels with mechanically induced surface instability of rubbers.

The effect of surface tension is found to be critical in suppressing short-wavelength modes of surface instability, while the substrate confinement suppresses long-wavelength modes. With both surface tension and substrate confinement, an intermediate wavelength is selected at a critical swelling ratio for onset of surface instability. Both the critical swelling ratio and the characteristic wavelength depend on the initial thickness of the hydrogel layer as well as other material properties of the hydrogel. It is found that the hydrogel layer becomes increasingly stable as the initial

layer thickness decreases. A critical thickness is predicted, below which the hydrogel layer swells homogeneously and remains stable at the equilibrium state.

Finally, three-dimensional finite element models are developed to simulate swelling deformation of hydrogel lines. Depending on the aspect ratio of the cross section as well as the material properties of the hydrogel, two types of swell-induced instability patterns are envisaged, i.e., localized surface instability versus global buckling.

Table of Contents

List of Figures	xi
Chapter 1 Introduction	1
1.1. Hydrogels and applications	1
1.2. Theory of polymer gels	4
1.3. Deformation instability of hydrogels	7
1.4. Scope of study.....	9
Chapter 2 Inhomogeneous swelling of hydrogels.....	12
2.1. A variational approach.....	12
2.1.1. General statements	12
2.1.2. Nominal quantities	15
2.1.3. Equilibrium equations	17
2.2. A free energy function for hydrogels.....	20
2.3. Analytical solutions for homogeneous swelling of hydrogel	24
2.3.1. Free, isotropic swelling	25
2.3.2. Anisotropic, homogeneous swelling of a hydrogel film	27
2.3.3. Anisotropic, homogeneous swelling of a hydrogel line	29
2.3.4. Effect of environmental pressure	30
2.4. A nonlinear finite element method	34
2.5. Numerical examples	40
2.5.1. Free, isotropic swelling	41
2.5.2. Homogeneous swelling of a hydrogel film	42
2.5.3. Homogeneous swelling of a hydrogel line	45
2.5.4. Inhomogeneous swelling of surface-attached hydrogel lines ..	45
2.6. Summary	56
Chapter 3 Swell-induced surface instability of confined hydrogel layers.....	57
3.1. Homogeneous swelling of a confined hydrogel layer.....	57
3.2. Linear perturbation analysis.....	60

3.3. Numerical simulations	77
3.4. Summary	81
Chapter 4 Effect of pre-stretch on swelling of hydrogels	83
4.1. Effect of pre-stretch on homogeneous swelling.....	83
4.2. Three-dimensional linear perturbation analysis.....	90
4.3. Effect of equi-biaxial pre-stretch on surface instability.....	97
4.4. Effect of plane-strain pre-stretch on surface instability	105
4.5. Summary	111
Chapter 5 Effect of surface tension on swell-induced surface instability of hydrogels.....	113
5.1. Effect of surface tension on homogeneous swelling.....	113
5.2. Linear perturbation analysis.....	116
5.3. Results and discussions.....	120
5.4. Summary	127
Chapter 6 Swell-induced buckling of hydrogel lines	129
6.1. Experiment.....	129
6.2. Three-dimensional finite element models.....	131
6.3. Results and discussions.....	133
6.4. Summary	138
Chapter 7 Conclusions	139
Appendix A ABAQUS user subroutines - UMAT and SIGNI.....	142
Appendix B Degenerated cases in 2-D perturbation analysis.....	148
Appendix C Degenerated cases in 3-D perturbation analysis.....	151
REFERENCES	153
Vita	166

List of Figures

Figure 1.1: Applications of hydrogels in biotechnology; (a) microencapsulation (b)tissue scaffolds [10].....	2
Figure 1.2: A shut-off valve. The arrows in a denote the direction of fluid flow. The fluid in the horizontal path controls the volume of the hydrogel and as a result, the hydrogel works as a shut-off valve for the fluid in the purple-colored path. b and d are top views and c and e are side views. In b and c the hydrogel is in the swollen state and press the membrane down and block the fluid flow. In d and e the hydrogel is in the shrunken state and the fluid flows. (Membranes are highlighted with yellow.) [13].....	3
Figure 1.3: Instability patterns in gels. (a) Creasing of a surface-attached hydrogel film [81], (b) Top view of the buckling of supported lines [78], (c) Wrinkling of a bilayered structure [80], (d) Bubble pattern evolution during shrinking process [77]	8
Figure 2.1: Schematic illustration of the reference state and the current state....	13
Figure 2.2: Three representative cases of homogeneous swelling of a hydrogel with $Nv = 0.001$ and $\chi = 0.1$	27
Figure 2.3: Effect of external solvent pressure on homogeneous swelling of a hydrogel film; (a) The swelling ratio, (b) The normalized in-plane true stress.....	32
Figure 2.4: Schematic illustration of the reference state (dry) and the equilibrium state (swollen) of a hydrogel, along with an auxiliary initial state used in numerical simulations	36

Figure 2.5: Comparison of numerical results with the analytical solution for free, isotropic swelling of a hydrogel.....	41
Figure 2.6: Anisotropic swelling of a hydrogel film under lateral constraint: (a) the swelling ratio in the thickness direction; (b) swelling-induced true stress in the lateral direction. Numerical results from two different implementations (UMAT and UHYPER) are compared to the analytical solution in Eqs. (2.36) and (2.37)	43
Figure 2.7: Anisotropic swelling of a hydrogel line under longitudinal constraint: (a) the swelling ratio in the lateral direction; (b) swelling-induced true stress in the longitudinal direction	44
Figure 2.8: Numerical steps to simulate inhomogeneous swelling of a hydrogel line ($W/H = 1$) attached to a rigid substrate: (a) the dry state; (b) the initial state; (c) deformation after releasing the side pressure in (b); (d) equilibrium swelling at $\mu = 0$, with the dashed box as the scaled dry state	46
Figure 2.9: Inhomogeneous swelling of surface-attached hydrogel lines: (a) average longitudinal stress; (b) volume ratio of swelling. The solid and dashed lines are analytical solutions for the homogeneous limits with $W/H \rightarrow \infty$ and $W/H \rightarrow 0$, respectively	50
Figure 2.10: Simulated swelling deformation and longitudinal stress distribution in surface-attached hydrogel lines of different aspect ratios: (a) $W/H = 1$; (b) $W/H = 5$; (c) $W/H = 10$. The rectangular boxes outline the cross sections in the dry state	52

Figure 2.11: Equilibrium volume ratio as a function of the dry-state width-to-height aspect ratio for inhomogeneous swelling of surface-attached hydrogel lines	53
Figure 2.12: Formation of surface creases in a surface-attached hydrogel line with $W/H = 12$ as the chemical potential increases: (a) $\bar{\mu} = -0.00075$, (b) $\bar{\mu} = -0.0003$, and (c) $\bar{\mu} = 0$	55
Figure 3.1: Schematic illustrations for (a) homogeneous swelling of a hydrogel layer, and (b) a perturbation of the swollen hydrogel layer	58
Figure 3.2: (a) Critical swelling ratio and (b) the corresponding chemical potential, predicted by the linear perturbation analysis, versus the perturbation wave number for $N\nu = 0.001$	67
Figure 3.3: (a) Critical swelling ratio and (b) critical chemical potential, predicted by the linear perturbation analysis at an infinite wave number (short-wavelength limit), versus $N\nu$ for different values of χ	70
Figure 3.4: A stability diagram for substrate-confined hydrogel layers.....	71
Figure 3.5: (a) Critical compressive stress and (b) critical linear strain, versus $N\nu$ for different values of χ . The dashed lines in (b) show the effective strain for homogeneous swelling at $\mu = 0$. The horizontal dash-dotted lines in (a) and (b) indicate the critical stress ($3.08Nk_B T$) and the critical strain (0.33) for a semi-infinite rubber, respectively	74

Figure 3.6: Numerical simulation of swell-induced surface instability of a substrate-confined hydrogel layer ($N\nu = 0.001$ and $\chi = 0.4$). Contours show distribution of the compressive true stress in the lateral direction (σ_{11}). (a) Initial perturbation at $\bar{\mu} = -0.0916$; (b) $\bar{\mu} = -0.00456$; (c) $\bar{\mu} = -0.00126$; (d) $\bar{\mu} = -0.000713$; and (e) $\bar{\mu} = 0$. The stress magnitude in the scale bar is normalized by the initial shear modulus of the polymer network ($Nk_B T$).78

Figure 3.7: Evolution of the surface profile of a substrate-confined hydrogel layer ($N\nu = 0.001$ and $\chi = 0.4$). (a) Initial perturbation at $\bar{\mu} = -0.0916$; (b) $\bar{\mu} = -0.00456$; (c) $\bar{\mu} = -0.00126$; (d) $\bar{\mu} = -0.000713$; and (e) $\bar{\mu} = 0$ 80

Figure 4.1: Swelling of a hydrogel layer with prescribed in-plane stretches λ_1 and λ_3 ; (a) Reference state (dry, no stress), (b) Pre-stretched dry state, (c) Swollen state with pre-stretch.84

Figure 4.2: Homogeneous swelling of hydrogel films at equilibrium vapor pressure with prescribed lateral stretches for equi-biaxial pre-stretch and for plane-strain pre-stretch ($N\nu = 0.01$, $\chi = 0.1$, and $\bar{p}_0 = 0.000023$)...86

Figure 4.3: Nominal in-plane stress components with respect to the prescribed in-plane stretches at equilibrium state. ($N\nu = 0.01$ and $\chi = 0.1$) ; (a) Equi-biaxial pre-stretch ($\lambda_1 = \lambda_3$), (b) Plane-strain pre-stretch ($\lambda_3 = 1$). ...89

Figure 4.4: Color contours of critical swelling ratio (λ_2) vs. wavenumbers (k_1 and k_3) for $N\nu = 0.01$, $\chi = 0.1$, $\bar{p}_0 = 0.000023$, and $\lambda_1 = \lambda_3 = 0.9$98

Figure 4.5: A stability map for hydrogels under equi-biaxial pre-stretch ($N\nu = 0.01$, $\chi = 0.1$).....100

Figure 4.6: (a) Critical swelling ratio, and (b) critical in-plane true stress ($\sigma_{11} = \sigma_{33}$) for hydrogels under equi-biaxial pre-stretch ($\lambda_1 = \lambda_3$), with $\chi = 0.1$	103
Figure 4.7: Critical pre-stretch at zero chemical potential (equilibrium vapor pressure) with respect to varying Nv for the equi-biaxial case	104
Figure 4.8: Color contours of critical swelling ratio (λ_2) vs. wavenumbers (k_1 and k_3) for $Nv = 0.01$, $\chi = 0.1$, $\bar{p}_0 = 0.000023$; (a) $\lambda_1 = 0.6$, $\lambda_3 = 1$, (a) $\lambda_1 = 1.5$, $\lambda_3 = 1$	106
Figure 4.9: A stability map for hydrogels under plane strain pre-stretch ($Nv = 0.01$, $\chi = 0.1$).....	107
Figure 4.10: (a) Critical swelling ratio, and (b) critical in-plane true stress ($\sigma_c = \sigma_{11}$ for $\lambda_1 < 1$, $\sigma_c = \sigma_{33}$ for $\lambda_1 > 1$) for hydrogels under plane-strain pre-stretch ($\lambda_3 = 1$), with $\chi=0.1$	109
Figure 4.11: Critical pre-stretch at zero chemical potential (equilibrium vapor pressure) with respect to varying Nv for the plane-strain state	110
Figure 5.1: Equilibrium swelling ratio of a spherical hydrogel particle under surface tension effect.....	115
Figure 5.2: Schematic illustrations of substrate-confined hydrogel layers: (a) homogeneous swelling; (b) onset of swell-induced surface instability; (c) formation of surface creases	117

Figure 5.3: (a) Critical swelling ratio and (b) critical chemical potential, versus the perturbation wavelength for swell-induced surface instability of substrate-confined hydrogel layers with $N\nu = 10^{-3}$, $\chi = 0.4$, and $L = 0.53 \mu\text{m}$. The thick dashed lines show the results without the effect of surface tension, and the thin dashed line in (a) indicates the homogeneous swelling ratio at the equilibrium121

Figure 5.4: (a) The minimum critical swelling ratio and (b) the corresponding characteristic wavelength, versus the initial thickness of the substrate-confined hydrogel layers with $N\nu = 10^{-3}$ and $\chi = 0.4$. The lower dashed line in (a) shows the thickness-independent critical swelling ratio without the effect of surface tension, and the upper dashed line indicates the homogeneous swelling ratio at the equilibrium. The dashed line in (b) shows the power-law scaling of the characteristic wavelength ($S^* h_0 \sim h_0^{0.9}$).....122

Figure 5.5: The critical thickness of substrate-confined hydrogel layers, predicted as a function of $N\nu$ for various values of χ . The length scale L' is assumed to be a constant ($L' = 0.53 \text{ nm}$).....124

Figure 6.1: A fabrication process of hydrogel lines: (a) spin-coat, (b) e-beam exposure, (c) develop in water [78]130

Figure 6.2: Atomic force micrographs of swollen polymer lines with the dry-state width:height dimensions as labeled in the panels. The lines were $5 \mu\text{m}$ long before swelling. (*Courtesy of Tirumala*).....131

Figure 6.3: A three-dimensional finite element model of a hydrogel line attached to a rigid substrate (initially swollen state by λ_0).....132

Figure 6.4: Buckling of hydrogel lines bonded to a rigid substrate for different $N\nu$ (width-to-height ratio 1). (A detail view of A is shown in Fig. 6.6)	133
Figure 6.5: Normalized buckling amplitude as a function of $N\nu$. ($W/H = 1$, $\chi = 0.55$)	134
Figure 6.6: A crease-like fold evolution inside the circle, at A in Fig. 6.4 ($N\nu = 0.001$, $\chi=0.55$, $W/H = 1$).	136
Figure 6.7: Buckling of hydrogel lines bonded to a rigid substrate for various width-to-height ratios ($N\nu = 0.01$ and $\chi = 0.55$).	137
Figure 6.8: Normalized buckling amplitude as a function of W/H . ($N\nu = 0.01$, $\chi = 0.55$)	138

Chapter 1

Introduction

1.1. HYDROGELS AND APPLICATIONS

An aggregate of a polymer network and small solvent molecules (e.g., water) forms a polymeric gel. When the polymer network is swollen in water, it is referred to as a hydrogel. In response to various environmental stimuli (e.g., temperature [1], pH [2], electric field [3], light [4]), a hydrogel can swell or shrink dramatically by absorbing or desorbing the solvent molecules. Since the first observation of large volume change in a gel was reported in 1950 by Kuhn et al. [5], there has been extensive amount of studies on gels, both experimentally and theoretically, as reviewed by Li and Tanaka [6] and more recently by Tokarev and Minko [7].

In addition to their large volumetric change, biocompatibility and physical similarity to natural tissues make hydrogels attractive for applications in biotechnology and medicine, such as drug delivery, tissue engineering, and biosensors[6-12]. Figure 1.1 (a) illustrates an immunoisolation barrier for microencapsulation where the cells inside the hydrogel are protected from the host's immune system and delivered safely to a target place. A hydrogel can be used as a scaffold which mimics the extracellular matrix and serves as a base for cell adhesion, migration, and growth as illustrated in Fig 1.1 (b).

Large and reversible volumetric change of hydrogels has also made hydrogels attractive for sensors and actuators applications. The relatively slow process of long range migration of molecules can be an obstacle for these applications. But miniaturization in microdevices can potentially resolve such a problem. For example, an

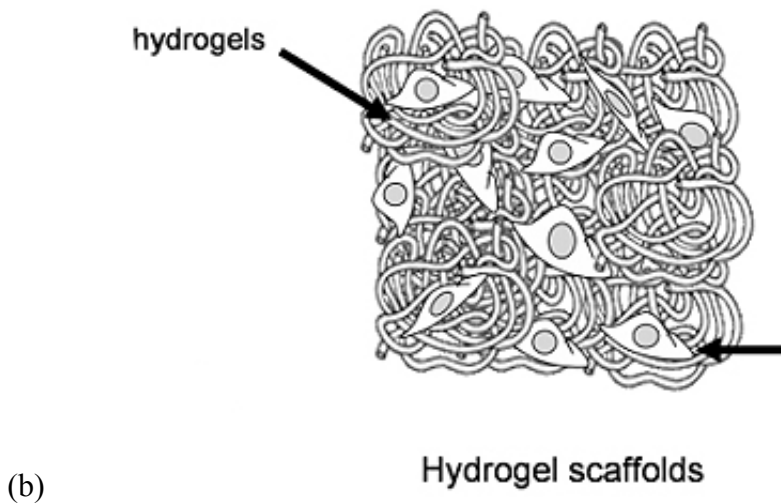
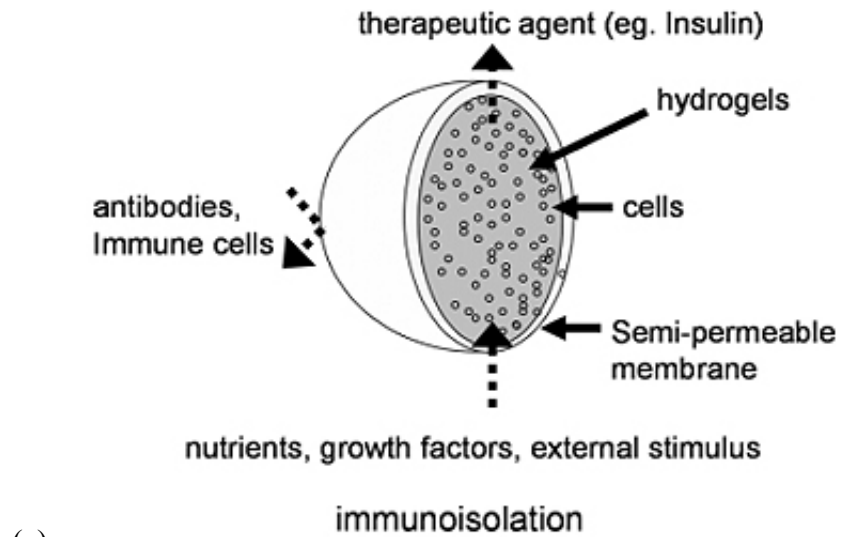


Figure 1.1: Applications of hydrogels in biotechnology; (a) microencapsulation (b) tissue scaffolds [10].

autonomous flow control in microfluidics using hydrogel is envisioned by Beebe et al. [13]. As shown in Fig. 1.2, a hydrogel body is located on top of a membrane connected to the adjacent flow channel. The hydrogel is controlled by the solution that passes along

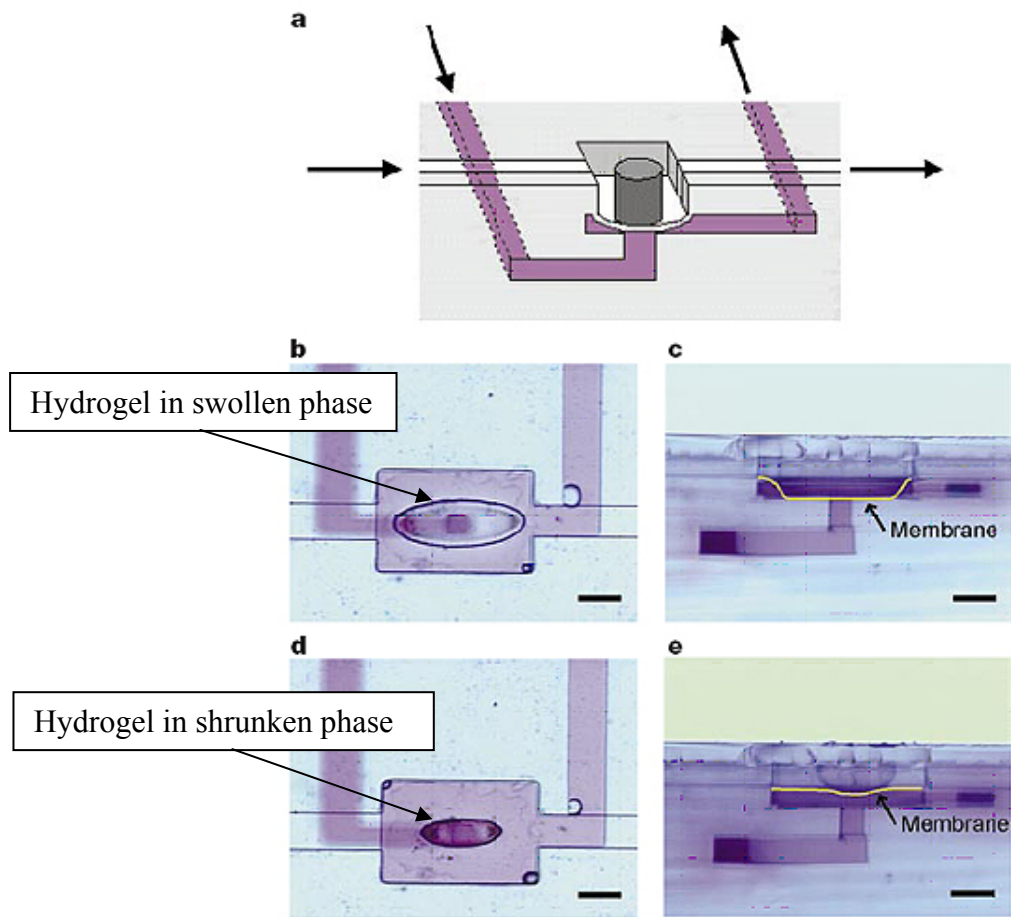


Figure 1.2: A shut-off valve. The arrows in **a** denote the direction of fluid flow. The fluid in the horizontal path controls the volume of the hydrogel and as a result, the hydrogel works as a shut-off valve for the fluid in the purple-colored path. **b** and **d** are top views and **c** and **e** are side views. In **b** and **c** the hydrogel is in the swollen state and press the membrane down and block the fluid flow. In **d** and **e** the hydrogel is in the shrunken state and the fluid flows. (Membranes are highlighted with yellow.) [13]

the horizontal path in **a**. If the hydrogel is swollen then the hydrogel presses the membrane down, which in turn blocks the flow channel described in **b** and **c**. When the hydrogel is in the shrinking state, the membrane goes back to the original position and the

flow channel is opened as in **d** and **e**. Then the fluid can flow. As described, the hydrogel works as a shut-off valve.

Another intriguing application of hydrogels is for energy storage devices. Generally, the conductivity of solvent-free gel is poor at room temperature, but high fraction of water in hydrophilic hydrogels increases, in general, the mobility of molecules [14-15]. In particular, the electrical conductivity is related to ionic mobility in the water-swollen gel. Conducting hydrogels, compared with other charge transport materials, have some merits including high ionic conductivity, reliability, and easy handling and designing [15-16]. With these advantages, hydrogels show possible applications for solar cell [17], supercapacitor [18-19], and rechargeable lithium battery [20] by replacing the conventional liquid electrolytes.

Other potential applications of hydrogel-based materials are organic bioelectronics [21-22], adaptive microlenses [23], micropatterning [24-26], and microgravimetric, electronic, and optical transducers [7].

1.2. THEORIES OF POLYMER GELS

The study of polymer network systems can be traced back to the series of experiments on rubbers by Gough in 1805 [27]. The thermodynamics of elastic deformation as well as the observed thermoelastic effects in vulcanized rubber was first treated in 1850s by Lord Kelvin [28] and his associate, Joule [29]. However, only after the polymeric structure of rubber was correctly established by Staudinger in 1920 [30], the structural mechanism and entropic nature of the rubber elasticity was revealed by

Meyer et al. [31] in 1932. Meanwhile, a thorough analysis of the general conditions necessary for the rubber-like elasticity was carried out by Busse [32]. With the advent of a wide range of synthetic rubbers, the kinetic theory of rubber elasticity by Meyer et al. became rapidly significant and generally accepted.

Quantitative treatment of the interconnected polymer network was started in 1930s by Kuhn [33], and was extended later by James and Guth [34], Wall [35], Flory and Rehner [36], and Treloar [37]. Based on either an affine network [35-36] or a phantom network model [34], the statistical theories of polymer network were developed. By 1943, a comprehensive theory capable of giving a quantitative description of the elastic properties of a rubberlike material in any type of strain was in place [38]. By adopting the statistical thermodynamics of polymer solutions as developed by Flory [39] and Huggins [40], the theory had also been applied to the treatment of swelling phenomena of polymer networks [41-42].

Continual improvements on the statistical network models have been pursued by many, e.g., [41, 43-47]. On the other hand, a set of phenomenological theories have also been developed to mathematically describe large elastic deformation of rubberlike materials since 1940s. Notable works of this kind are due to Mooney [48], Rivlin [49], Ogden [50], Yeoh [51], and Gent [52]. A relatively recent review on the constitutive models of rubberlike materials was given by Arruda and Boyce[53].

A polymer gel is a three-dimensional polymer network swollen with a solvent. The equilibrium swelling of isotropic, neutral polymer network is generally well described by the Flory-Rehner theory [42, 54], which is a combination of the Flory-

Huggins polymer solution theory [39-40] and the statistical network theory of rubber elasticity . A single-chain mean-field theory of polymer gels was proposed by Huang et al. [55]. These mean-field theories are typically concerned with homogeneous swelling phenomena [38]. However, under mechanical or geometric constraints, inhomogeneous swelling commonly occurs. Based on a thermodynamic theory of nonlinear heterogeneous fields due to Gibbs [56], a theoretical framework for inhomogeneous equilibrium swelling of polymer gels was developed recently [57]. This theory treats the gel as a single continuum phase with its constitutive behavior described by the thermodynamics of swelling, thus coupling the mechanical deformation of the polymer network with the solvent distribution (absorption) at the constitutive level. The same approach is adopted in the present study.

Deformation of polymer gels necessarily involves the kinetics of molecular transport during swelling or shrinking. Several different approaches have been taken to model the kinetic processes in gels. From phenomenological arguments Tanaka et al. [58-59] derived a linear diffusion equation assuming a coefficient of friction between the network and the liquid. A similar theory was later developed by Durning and Morman [60] for nonlinear swelling of polymer gels. Other forms of diffusion equations have also been proposed for the study of gel dynamics, e.g., [61-65]. A similarity between the gel theories and poroelasticity has been noticed by several authors, although the latter is mostly concerned with geomechanics [66-67] and metallurgy [68]. A different approach, known as the mixture theory, has also been developed for polymer gels e.g., [69-70], based on a thermodynamic framework of multi-component mixtures due to Truesdell

[71]. As another approach, Dolbow et al. [72-73] developed a sharp-interface theory for chemically and thermally induced swelling of hydrogels, following a phase-transition theory by Gurtin and Struthers [74].

1.3. DEFORMATION INSTABILITY OF HYDROGELS

Experimental studies have shown complex material behaviors of gels [6-7]. Subject to geometric confinement and/or mechanical constraint, a variety of deformation instability patterns have been observed in gel-like materials [75-82]. Figure 1.3 shows a few examples. In Fig. 1.3 (a), swelling of a hydrogel film attached to a rigid substrate resulted in the formation of surface creases [81]. In Fig. 1.3 (b), patterned hydrogel nanolines on a rigid substrate were swollen in a solvent. Confined by the substrate at the bottom by chemical bonding, the upper portion of the hydrogel lines buckled to form a wavy structure [78]. In Fig. 1.3 (c), a relatively hard gel layer was placed on top of a soft gel. Immersed in a solvent, the top layer swelled and formed wrinkles [80]. In Fig. 1.3 (d), a bubble patterned was observed during the shrinking process of a hydrogel cylinder [77].

Of particular interest to the present study is the formation of surface creases in hydrogels as shown in Fig. 1.3 (a). Surface instability of swollen rubber vulcanizates was first observed by Southern and Thomas [75], who reported a critical swelling ratio of about 2.5 due to the effect of substrate constraint. Later, a wide range of critical swelling ratios were observed for different gel systems, between 2.46 and 3.72 by H. Tanaka et al. [83] and around 2 by Trujillo et al. [81]. T. Tanaka et al. [76] found that many gels

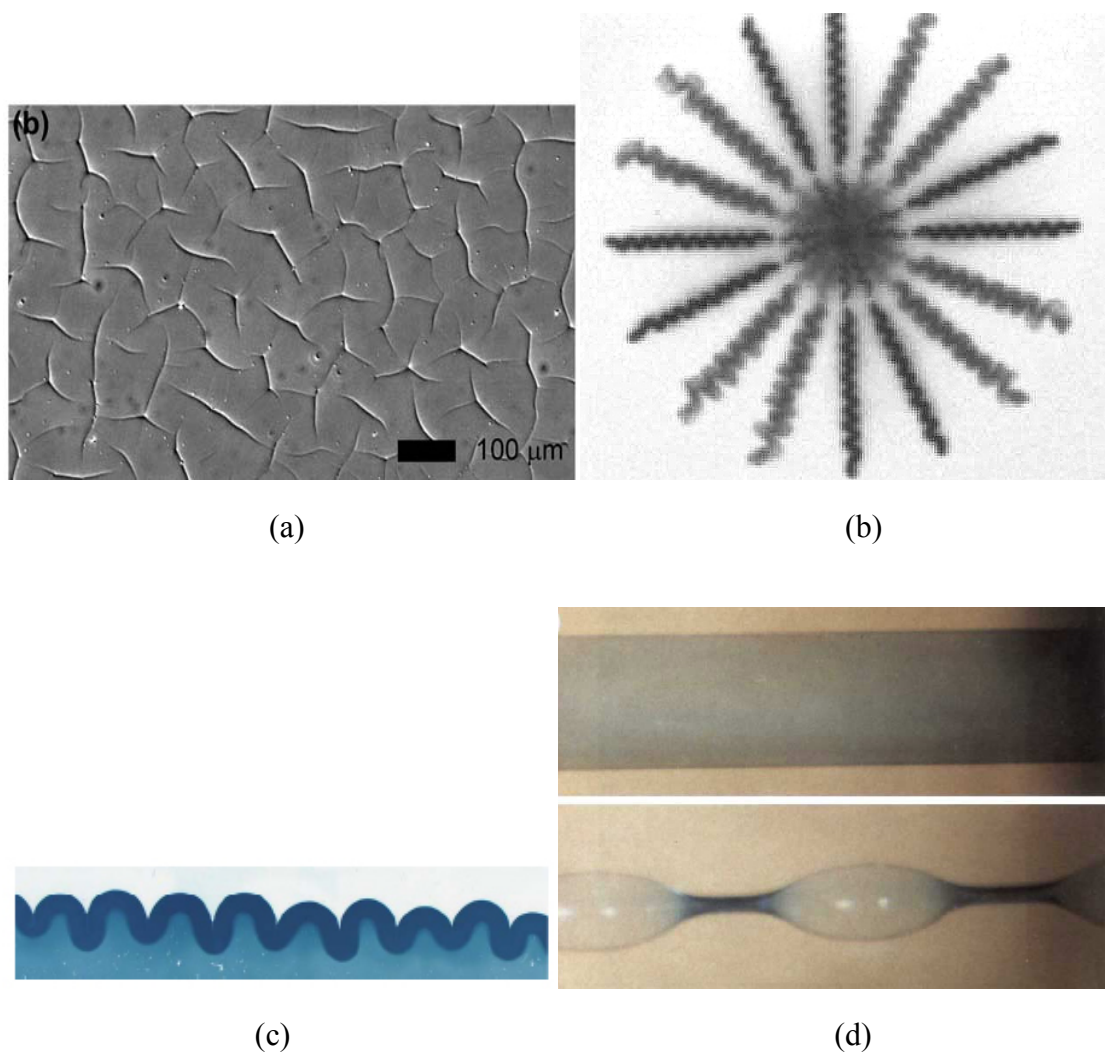


Figure 1.3: Instability patterns in gels. (a) Creasing of a surface-attached hydrogel film [81], (b) Top view of the buckling of supported lines [78], (c) Wrinkling of a bilayered structure [80], (d) Bubble pattern evolution during shrinking process [77].

formed surface patterns during swelling process, and they suggested a critical osmotic pressure for the surface instability, although their analysis implied a critical compressive stress. More recently, Trujillo et al. [81] showed that the critical condition for surface creasing in their experiments with a model hydrogel system agreed well with the

prediction by a linear perturbation analysis for rubber under equi-biaxial compression [84], with a critical linear compressive strain $\sim 33\%$ relative to the state of free swelling for unconstrained hydrogels. On the other hand, Gent and Cho [85] found that Biot's prediction considerably overestimated the critical strain for surface creasing in their experiments with rubbers compressed by mechanical bending. A recent work by Hong et al. [86] argued that surface creasing is a different mode of surface instability in contrast with Biot's linear perturbation analysis, and they predicted a critical swelling ratio at 2.4 for surface creasing of gels based on an energetic consideration and numerical calculations for neo-Hookean elastomers. Several other theoretical models have also been proposed for swelling induced surface instability in gels, e.g., [87-89]. However, it remains elusive how the critical swelling ratio varies from around 2 to 3.72 as reported by experimental studies [75, 81, 83].

1.4. SCOPE OF STUDY

The present study focuses on inhomogeneous swelling of hydrogels under mechanical constraints, with an emphasis on swell induced surface instability. This dissertation is organized as follows.

Chapter 1 presents a brief introduction to the background of this study, motivated by exciting applications of hydrogel materials as well as the fundamental challenges from a theoretical perspective

Chapter 2 is dedicated to the development of a theoretical framework for swelling deformation of hydrogels. By a variational method, the equilibrium equations and the

corresponding boundary conditions are obtained. With a specific free energy density function, a finite element method (FEM) is developed, which is implemented as a user material subroutine (UMAT) in ABAQUS. Numerical results are presented for several examples.

Chapter 3 presents a theoretical analysis on swell-induced surface instability of hydrogel layers. A linear perturbation analysis is performed to predict the critical instability conditions. As a result, critical swelling ratios and the corresponding critical compressive stresses and critical strain are calculated, and a stability diagram is constructed.

Chapter 4 extends the linear perturbation analysis to study the effects of pre-stretch on surface instability of hydrogels. Equi-biaxial and plane strain compression are considered. A general critical condition for surface instability is obtained, unifying swell-induced instability with Biot's analysis on mechanically induced surface instability in rubber [84].

In Chapter 5, the effect of surface tension on swell-induced surface instability of hydrogel is studied. As a result, the hydrogel layer becomes increasingly stable as the layer thickness decreases, and a critical thickness is predicted. In addition, a characteristic wavelength for the surface instability is obtained.

In Chapter 6, three-dimensional models of surface-attached hydrogel lines are simulated with a finite element method. Depending on the material properties and width-to-height aspect ratio, numerical simulations show two types of instability patterns during swelling – creasing and buckling.

Finally, Chapter 7 concludes the present study with a summary and an outlook for further studies.

Chapter 2

Inhomogeneous swelling of hydrogels

This chapter derives governing equations and corresponding boundary conditions for equilibrium swelling deformation of hydrogels, and serves as the basis for the studies in the subsequent chapters. A finite element method is developed for numerical simulations of complicated inhomogeneous problems. As an example, inhomogeneous swelling of hydrogel lines attached to a rigid substrate is studied. By following the previously developed theory by Hong et al.[57, 63], a general variational approach is presented here and an alternative method for finite element analysis is developed.

2.1. A VARIATIONAL APPROACH

2.1.1. General statements

Consider a hydrogel body (current state) of volume Ω enclosed by a surface Γ , subjected to a distributed body force, b_i , and surface traction, t_i . In addition, the hydrogel is immersed in a solvent environment of chemical potential $\hat{\mu}$ (per solvent molecule), and transport of the solvent molecules occurs within the hydrogel body and across the interface Γ as illustrated in Fig. 2.1. Part of the surface Γ may be mechanically constrained (e.g., attached to a rigid body) and/or chemically isolated from the solvent.

With an infinitesimal variation to the current state in terms of both mechanical displacement and molecular transport, the total work done to the hydrogel includes the

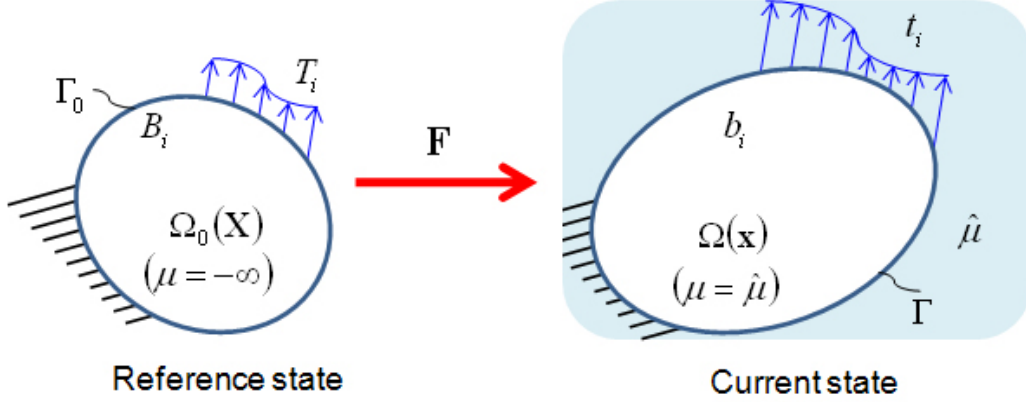


Figure 2.1: Schematic illustration of the reference state and the current state

mechanical work by the body force and the surface traction and the chemical work via absorption of solvent molecules, namely,

$$\delta W = \int_{\Omega} b_i \delta x_i dV + \oint_{\Gamma} t_i \delta x_i dS - \oint_{\Gamma} \hat{m}_k \delta \tilde{i}_k dS, \quad (2.1)$$

where δx_i is the variation of the current position and $\delta \tilde{i}_k$ is the variation of the molecular flux, defined as the number of solvent molecules across per unit area of a surface element with the surface normal in the direction x_k . The product $-n_k \delta \tilde{i}_k$ gives the number of solvent molecules entering the gel per unit area of its surface, where n_k is the unit normal vector on the surface (positive outwards). We ignore the injection of solvent molecules by distributed pump that was included in the theory by Hong et al. [63]. Additional terms may be added in Eq. (2.1) to include works done by other fields (e.g., temperature, electric field).

Assuming a free energy density function for the hydrogel, u , the variation of the total free energy of the hydrogel is

$$\delta\Phi = \delta\left(\int_{\Omega} u dV\right). \quad (2.2)$$

The functional form of u determines the constitutive behavior of the hydrogel, which will be discussed later with a specific material model.

The variation of the free energy for the thermodynamic system including the hydrogel and its mechanical/chemical environment is

$$\delta G = \delta\Phi - \delta W. \quad (2.3)$$

For all thermodynamically permissible variations, $\delta G \leq 0$ [90]. If the current state is a thermodynamic equilibrium state, $\delta G = 0$ for any arbitrary variation. Otherwise, the system evolves to reduce its free energy ($\delta G < 0$).

Furthermore, mass conservation of the solvent molecules requires that

$$\delta\left(\int_{\Omega} c dV\right) = -\oint_{\Gamma} n_k \delta i_k dS, \quad (2.4)$$

where c is the concentration of the solvent molecule in the hydrogel (i.e., number of molecules per unit volume). Equation (2.4) simply states that the total number of solvent molecules in the gel changes only as the molecules enter or leave the gel through the boundary (Γ), assuming no sources or distributed pumps inside the body (Ω). We emphasize that this statement does not assume incompressibility of the solvent molecules or the polymer network.

The left-hand side of Eq. (2.4) can be decomposed into two parts, namely,

$$\delta\left(\int_{\Omega} c dV\right) = \int_{\Omega} \delta c dV + \int_{\Omega} c \delta x_{k,k} dV, \quad (2.5)$$

where the second term on the right-hand side of Eq. (2.5) represents the contribution from the volume change in the gel, with $\delta x_{k,k}$ being the linear volumetric strain for an infinitesimal variation from the current state.

By substituting Eq. (2.5) into Eq. (2.4) and applying the divergence theorem on the right-hand side, we obtain that

$$\int_{\Omega} (\delta c + c \delta x_{k,k}) dV = - \int_{\Omega} \delta i_{k,k} dV. \quad (2.6)$$

For Eq. (2.6) to hold everywhere inside the gel, it necessarily requires that

$$\delta c = -\delta i_{k,k} - c \delta x_{k,k} \quad \text{in } \Omega \quad (2.7)$$

Therefore, the general statements of the variational principle for the hydrogel include one for the variation of free energy (Eq. (2.3)) and one for the mass conservation (Eq. (2.4) or Eq. (2.7)).

2.1.2. Nominal quantities

It is often convenient to use nominal quantities referring to a reference configuration with fixed volume Ω_0 and surface Γ_0 . As illustrated in Fig. 2.1, a deformation gradient tensor maps the reference configuration to the current state, namely,

$$dx_i = F_{iK} dX_K \quad \text{and} \quad F_{iK} = \frac{\partial x_i}{\partial X_K}, \quad (2.8)$$

where X_K refers to the fixed coordinates in the reference state. While the choice of the reference state is arbitrary in general, we choose the dry state of the hydrogel as the reference state in the present study. As will be discussed later, such a choice is necessary

for the use of a specific free energy function. On the other hand, it poses a numerical challenge that has to be circumvented in finite element analysis.

The differential volume and surface area in the current state are related to those in the reference state by

$$dV = JdV_0 \quad \text{and} \quad n_i dS = A_{iJ} N_J dS_0, \quad (2.9)$$

where N_J is the unit normal of the surface in the reference state, and

$$J = \det(\mathbf{F}), \quad A_{iJ} = \frac{1}{2} e_{ijk} e_{JKL} F_{jK} F_{kL}. \quad (2.10)$$

Thus, a set of nominal quantities (in upper cases) can be defined as follows:

- Nominal body force \mathbf{B} : $B_i dV_0 = b_i dV$;
- Nominal surface traction \mathbf{T} : $T_i dS_0 = t_i dS$;
- Nominal molecular flux \mathbf{I} : $N_K I_K dS_0 = n_k i_k dS$;
- Nominal free energy density U : $U dV_0 = u dV$;
- Nominal molecular concentration C : $C dV_0 = c dV$.

In terms of the nominal quantities, the variational statements in Eq. (2.1), (2.2), and (2.4) are re-written as

$$\delta W = \int_{\Omega_0} B_i \delta x_i dV_0 + \oint_{\Gamma_0} T_i \delta x_i dS_0 - \oint_{\Gamma_0} \hat{\mu} N_K \delta I_K dS_0, \quad (2.11)$$

$$\delta \Phi = \int_{\Omega_0} \delta U dV_0, \quad (2.12)$$

$$\int_{\Omega_0} \delta C dV_0 = - \oint_{\Gamma_0} N_K \delta I_K dS_0. \quad (2.13)$$

Applying the divergence theorem to Eq. (2.13) leads to

$$\delta C = -\frac{\partial}{\partial X_K}(\delta I_K) \quad \text{in } \Omega_0. \quad (2.14)$$

2.1.3. Equilibrium equations

In the equilibrium state, $\delta G = \delta \Phi - \delta W = 0$, and thus

$$\int_{\Omega_0} \delta U dV_0 = \int_{\Omega_0} B_i \delta x_i dV_0 + \oint_{\Gamma_0} T_i \delta x_i dS_0 - \oint_{\Gamma_0} \hat{\mu} N_K \delta I_K dS_0. \quad (2.15)$$

Assume a general form of the nominal free energy density function, $U(\mathbf{F}, C)$.

Variation of the free energy at the left hand side of Eq. (2.15) can be carried out as follows:

$$\begin{aligned} \int_{\Omega_0} \delta U dV_0 &= \int_{\Omega_0} \frac{\partial U}{\partial F_{iK}} \delta F_{iK} dV_0 + \int_{\Omega_0} \frac{\partial U}{\partial C} \delta C dV_0 \\ &= \int_{\Omega_0} \frac{\partial U}{\partial F_{iK}} \frac{\partial}{\partial X_K} (\delta x_i) dV_0 - \int_{\Omega_0} \frac{\partial U}{\partial C} \frac{\partial}{\partial X_K} (\delta I_K) dV_0 \end{aligned} \quad (2.16)$$

By applying the divergence theorem, we obtain that

$$\begin{aligned} \int_{\Omega_0} \delta U dV_0 &= \oint_{\Gamma_0} \frac{\partial U}{\partial F_{iK}} N_K \delta x_i dS_0 - \int_{\Omega_0} \frac{\partial}{\partial X_K} \left(\frac{\partial U}{\partial F_{iK}} \right) \delta x_i dV_0 \\ &\quad - \oint_{\Gamma_0} \frac{\partial U}{\partial C} N_K \delta I_K dS_0 + \int_{\Omega_0} \frac{\partial}{\partial X_K} \left(\frac{\partial U}{\partial C} \right) \delta I_K dV_0 \end{aligned} \quad (2.17)$$

Thus, the equilibrium condition in Eq. (2.15) becomes

$$\begin{aligned} &\oint_{\Gamma_0} \left(\frac{\partial U}{\partial F_{iK}} N_K - T_i \right) \delta x_i dS_0 - \int_{\Omega_0} \left[\frac{\partial}{\partial X_K} \left(\frac{\partial U}{\partial F_{iK}} \right) + B_i \right] \delta x_i dV_0 \\ &- \oint_{\Gamma_0} \left(\frac{\partial U}{\partial C} - \hat{\mu} \right) N_K \delta I_K dS_0 + \int_{\Omega_0} \frac{\partial}{\partial X_K} \left(\frac{\partial U}{\partial C} \right) \delta I_K dV_0 = 0 \end{aligned} \quad (2.18)$$

For Eq. (2.18) to hold for arbitrary variations, it necessarily requires that

$$\begin{cases} \frac{\partial}{\partial X_K} \left(\frac{\partial U}{\partial F_{iK}} \right) + B_i = 0 \\ \frac{\partial}{\partial X_K} \left(\frac{\partial U}{\partial C} \right) = 0 \end{cases} \quad \text{in } \Omega_0, \quad (2.19)$$

and

$$\begin{cases} \frac{\partial U}{\partial F_{iK}} N_K = T_i \text{ or } \delta x_i = 0 \\ \frac{\partial U}{\partial C} = \hat{\mu} \text{ or } N_K \delta I_K = 0 \end{cases} \quad \text{on } \Gamma_0. \quad (2.20)$$

The governing equations for the equilibrium state of the hydrogel are thus established in Eq. (2.19), along with the boundary conditions in Eq. (2.20). It is noted that, in the variational analysis, the deformation gradient (\mathbf{F}) and the concentration (C) have been taken as the state variables in the definition of free energy function (U), while the mechanical displacement of the polymer network (δx_i) and the molecular flux of the solvent (δI_k) are the physical processes that change the current state of the hydrogel. In the equilibrium state, the free energy G is minimized with respect to arbitrary variations in both displacement and flux.

Now we may define the nominal stress and chemical potential as work conjugates of the deformation gradient and solvent concentration, respectively:

$$s_{iK} = \frac{\partial U}{\partial F_{iK}} \quad \text{and} \quad \mu = \frac{\partial U}{\partial C}. \quad (2.21)$$

The equilibrium equations and the boundary conditions are then re-written as

$$\begin{cases} \frac{\partial s_{iK}}{\partial X_K} + B_i = 0 \\ \frac{\partial \mu}{\partial X_K} = 0 \end{cases} \quad \text{in } \Omega_0, \quad (2.22)$$

and

$$\begin{cases} s_{iK} N_K = T_i \quad \text{or} \quad \delta x_i = 0 \\ \mu = \hat{\mu} \quad \text{or} \quad N_K \delta I_K = 0 \end{cases} \quad \text{on } \Gamma_0. \quad (2.23)$$

We note that, in addition to the familiar boundary conditions for the mechanical traction (natural) and displacement (essential), the chemical boundary condition can be specified either by the chemical potential of the external solvent or by zero flux (e.g., surface isolated or blocked from the solvent). It is also possible to have mixed boundary conditions.

Although the two field equations in Eq. (2.22) appear to be uncoupled, both the nominal stress s_{iK} and the chemical potential μ are derived from the same free energy density function U , and are coupled in general through the constitutive behavior of the hydrogel. The second equation (chemical equilibrium) dictates that the chemical potential be a constant in the equilibrium state (if an equilibrium state exists). This is only possible when the hydrogel is in contact with a homogeneous solvent of a constant chemical potential, i.e., $\mu = \hat{\mu} = \text{const.}$ The constant chemical potential in the hydrogel as an equilibrium condition is analogous to the constant temperature as an equilibrium condition for heat transfer.

The chemical potential of the external solvent ($\hat{\mu}$) in general depends on the temperature (T) and pressure (p). Assuming an ideal gas phase ($p < p_0$) and an incompressible liquid phase ($p > p_0$), the chemical potential is given by [63]:

$$\hat{\mu} = \begin{cases} (p - p_0)v, & \text{if } p > p_0; \\ k_B T \log(p / p_0), & \text{if } p < p_0, \end{cases} \quad (2.24)$$

where p_0 is the equilibrium vapor pressure, v is the volume per solvent molecule, and k_B is the Boltzmann constant. At the equilibrium vapor pressure ($p = p_0$), the external chemical potential $\hat{\mu} = 0$. For a specific solvent, the equilibrium vapor pressure depends on temperature (T). For water at 25°C ($T = 298\text{K}$), $p_0 \sim 3.2\text{kPa}$ and $v \sim 3 \times 10^{-29} \text{m}^3$.

In a non-equilibrium state, the solvent molecules migrate within the gel and the polymer network deforms to reduce the potential energy G , i.e., $\delta G < 0$. Assuming self diffusion as the dominant kinetic process, Hong et al. [63] developed a kinetic model, based on which a finite element method was developed for transient analysis of swelling polymeric gels [82]. The present study focuses on analysis of equilibrium states only.

2.2. A FREE ENERGY FUNCTION FOR HYDROGELS

In addition to the governing equations, a specific functional form of the free energy density, $U(\mathbf{F}, C)$, is needed for analysis of the swelling deformation of hydrogels. Following the approach of Flory [42], we adopt a free energy function that consists of two parts, one for elastic deformation of the polymer network and the other for mixing of the solvent molecules with the polymer chains, namely

$$U(\mathbf{F}, C) = U_e(\mathbf{F}) + U_m(C). \quad (2.25)$$

Based on a statistical mechanics model of rubber elasticity, the elastic free energy density was obtained by Flory [42, 91] as

$$U_e(\mathbf{F}) = \frac{1}{2} N k_B T [\lambda_1^2 + \lambda_2^2 + \lambda_3^2 - 3 - \ln(\lambda_1 \lambda_2 \lambda_3)], \quad (2.26)$$

where λ_1 , λ_2 , and λ_3 are the principal stretches in the principal directions of the deformation gradient tensor \mathbf{F} , and N is the effective number of polymer chains per unit volume of the hydrogel in the dry state which in turn is related to the crosslink density of the polymer network. It is well known that $N k_B T$ defines the initial shear modulus of an elastomer. As noted by Flory [42], the only quantity pertaining to the molecular structure of the network in Eq. (2.26) is N , under the assumption of Gaussian distribution for the end-to-end vectors of the polymer chains. The quantity N is determined by the degree of cross-linking. For normal cross-linking (in which four chains meet at each junction point) it is simply equal to twice the number of cross links per unit volume. As the degree of cross-linking is increased the mean chain contour length becomes smaller, hence N may be expressed alternatively in terms of the number average chain molecular weight M_c . The appropriate relationship is [38]

$$N k_B T = \rho R T / M_c, \quad (2.27)$$

in which ρ is the density of the polymer and R is the gas constant per mole. Furthermore, by considering the effect of network defects (e.g, presence of “terminal” chains), Flory showed that the effective number of chains is [42]

$$N = N_0 \left(1 - \frac{2M_c}{M} \right), \quad (2.28)$$

where $N_0 = N_A \rho / M_c$, M is the molecular weight of the linear polymer chains before cross-linking, and $N_A = R / k_B$ is Avogadro's number.

When the deformation does not change volume (i.e., $\lambda_1 \lambda_2 \lambda_3 = 1$), Eq. (2.26) reduces to the familiar strain energy density function for incompressible neo-Hookean materials [49]. During swelling deformation of a hydrogel, however, the volume changes dramatically. The last term in the bracket of Eq. (2.26), resulting from the entropy change associated with the volume change, is however problematic from a mechanics standpoint [38, 92]. To account for the volume change in rubber elasticity, many other forms of the free energy function have been suggested [38, 53, 92-94]. In the present study, following Hong et al. [63], we take the elastic free energy function as

$$U_e(\mathbf{F}) = \frac{1}{2} N k_B T \left[\lambda_1^2 + \lambda_2^2 + \lambda_3^2 - 3 - 2 \ln(\lambda_1 \lambda_2 \lambda_3) \right] = \frac{1}{2} N k_B T (F_{iK} F_{iK} - 3 - 2 \ln J), \quad (2.29)$$

which differs from Eq. (2.26) by a factor of 2 in the volumetric term. The same functional form was suggested by others based on mathematical considerations [92] and a statistical mechanics model [95-96]. Note that the principal stretches and deformation gradient in Eq. (2.29) are defined with respect to the dry state as the reference, which is assumed to be isotropic. The functional form should be modified accordingly if a different reference state is used.

Based on Flory-Huggins polymer solution theory [42, 97], the free energy change due to the mixing of pure solvent with a polymer network was obtained as:

$$\Delta F_m = k_B T [n_1 \ln \varphi + \chi n_1 (1 - \varphi)], \quad (2.30)$$

where n_1 is the number of solvent molecules, φ is the volume fraction of the solvent, and χ is a dimensionless quantity that characterizes the interaction energy between the solvent and the polymer. The first term on the right hand side of Eq. (2.30) comes from the entropy of mixing, and the second term from the heat of mixing (enthalpy).

By the assumption of molecular incompressibility, the volume swelling ratio of the hydrogel is

$$J = \frac{V}{V_0} = 1 + \nu C. \quad (2.31)$$

It then follows that $n_1 = V_0 C$ and $\varphi = \frac{\nu C}{1 + \nu C}$. Thus, the free energy of mixing per unit volume is

$$U_m(C) = \frac{\Delta F_m}{V_0} = \frac{k_B T}{\nu} \left(\nu C \ln \frac{\nu C}{1 + \nu C} + \frac{\chi \nu C}{1 + \nu C} \right). \quad (2.32)$$

Eq. (2.32) differs slightly from that given in Hong et al. [63] by a constant, which is insignificant for swelling deformation. In the dry state, we have $C = 0$ and $U_m = 0$. The tendency to increase the entropy of mixing (thus decreasing the free energy) drives the solvent molecules to enter the polymer network. This tendency to mix may either be opposed ($\chi > 0$) or enhanced ($\chi < 0$) by the heat of mixing, depending on the sign of χ . Furthermore, as the process of absorption proceeds, the elastic energy of the network increases as a consequence of swelling. Ultimately, a state of equilibrium swelling may be obtained, in which the total free energy reaches a minimum.

Several limitations of the free energy function as given in Eqs. (2.25), (2.29), and (2.32) may be pointed out. First, the separation of the elastic free energy and the free energy of mixing in form of Eq. (2.25) is a simplification that may not hold in general. Second, the elastic free energy in Eq. (2.29) has its root in the Gaussian network model, which is limited to not so large strains, that is to say, to strains that do not begin to approach the limiting deformability of the network. In the region of very large strains, where an appreciable proportion of the chains become highly extended, the Gaussian statistical treatment is no longer valid, and it is necessary to investigate the properties of the network in terms of the more accurate ‘non-Gaussian’ statistical theory, which takes into account the finite extensibility of the chains, and hence of the network [38].

2.3. ANALYTICAL SOLUTIONS FOR HOMOGENEOUS SWELLING OF HYDROGELS

In the search for the equilibrium swelling state, the condition of molecular incompressibility in Eq. (2.31) may be imposed as a constraint that relates the solvent concentration C to the deformation of the polymer network. In cases of homogeneous swelling, a term with a Lagrange multiplier for the constraint can be added to the free energy function, namely

$$U(\mathbf{F}, C) = U_e(\mathbf{F}) + U_m(C) + \Pi(1 + \nu C - J). \quad (2.33)$$

As defined in Eq. (2.21), the principal nominal stresses are obtained as

$$\begin{aligned}
s_1 &= \frac{\partial U}{\partial \lambda_1} = Nk_B T \left(\lambda_1 - \frac{1}{\lambda_1} \right) - \Pi \lambda_2 \lambda_3, \\
s_2 &= \frac{\partial U}{\partial \lambda_2} = Nk_B T \left(\lambda_2 - \frac{1}{\lambda_2} \right) - \Pi \lambda_1 \lambda_3, \\
s_3 &= \frac{\partial U}{\partial \lambda_3} = Nk_B T \left(\lambda_3 - \frac{1}{\lambda_3} \right) - \Pi \lambda_1 \lambda_2.
\end{aligned} \tag{2.34}$$

The chemical potential is obtained as

$$\mu = \frac{\partial U}{\partial C} = k_B T \left[\ln \frac{\nu C}{1 + \nu C} + \frac{1}{1 + \nu C} + \frac{\chi}{(1 + \nu C)^2} \right] + \Pi \nu. \tag{2.35}$$

In the following, three examples of homogeneous swelling are presented.

2.3.1. Free, isotropic swelling

For three-dimensional (3-D) free, isotropic swelling, we have $s_1 = s_2 = s_3 = 0$ and $\lambda_1 = \lambda_2 = \lambda_3 = \lambda$. The external solvent pressure is usually small and thus ignored here, the effect of which will be discussed in Section 2.3.4. By Eq. (2.34), we have

$$\Pi = Nk_B T \left(\frac{1}{\lambda} - \frac{1}{\lambda^3} \right). \tag{2.36}$$

By Eq. (2.36), the chemical potential in the swollen hydrogel is

$$\mu = \frac{\partial U}{\partial C} = k_B T \left[\ln \frac{\nu C}{1 + \nu C} + \frac{1}{1 + \nu C} + \frac{\chi}{(1 + \nu C)^2} + N\nu \left(\frac{1}{\lambda} - \frac{1}{\lambda^3} \right) \right]. \tag{2.37}$$

The last term in the bracket of Eq. (2.37) represents a modification to the chemical potential due to elastic reaction of the polymer network. A similar formula for the chemical potential was obtained by Flory [42], with a factor of 2 difference in the last

term. The difference results from the different forms of the elastic free energy function in Eqs. (2.26) and (2.29).

By setting $\mu = \hat{\mu}$ as the external chemical potential defined in Eq. (2.24) and noting $\nu C = \lambda^3 - 1$ by the assumption of molecular incompressibility, the isotropic, homogeneous equilibrium swelling ratio can be solved from Eq. (2.37) as

$$\lambda = \lambda \left(\frac{\hat{\mu}}{k_B T}; N\nu, \chi \right), \quad (2.38)$$

where the two dimensionless quantities ($N\nu$ and χ) characterize the hydrogel material system, with N for the polymer network structure, ν for the solvent molecules, and χ for the solvent-polymer interaction. The effect of the external environment (e.g., temperature and vapor pressure) is accounted for in Eq. (2.37) via the normalized chemical potential. As an example, for a hydrogel with $\chi = 0.1$ and $N\nu = 10^{-3}$, the homogeneous swelling ratio is plotted in Fig. 2.2 as a function of the chemical potential, along with two other homogeneous swelling cases. As the chemical potential increases, the corresponding swelling ratio increases. At the equilibrium vapor pressure, we have $\hat{\mu} = 0$ and $\lambda = 3.390$; the corresponding volume ratio of swelling is: $J = \lambda^3 = 38.96$.

It is noted that the first term in the bracket of Eq. (2.37) is unbounded in the dry state (when $C = 0$). This is consistent with the definition of the external chemical potential in Eq. (2.24), which approaches negative infinity as the vapor pressure approaches zero (i.e., vacuum). However, the negative infinite chemical potential in the dry state poses a challenge for numerical simulations of swelling deformation under

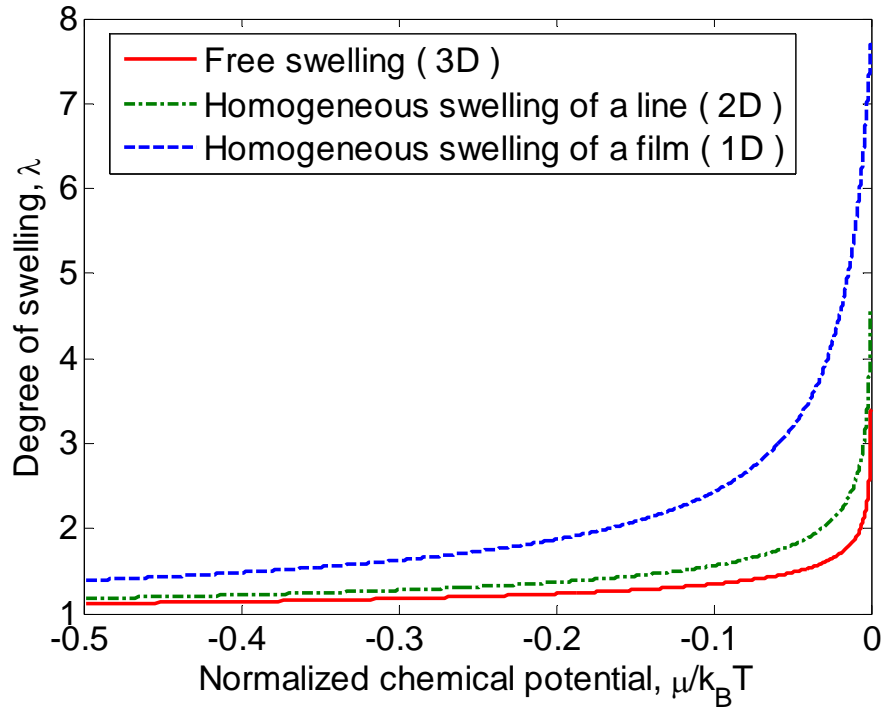


Figure 2.2: Three representative cases of homogeneous swelling of a hydrogel with $Nv = 0.001$ and $\chi = 0.1$.

constraints from the dry state, as will be discussed in the subsequent sections.

2.3.2. Anisotropic, homogeneous swelling of a hydrogel film

Next consider a hydrogel film bonded to a rigid substrate, which swells preferably in the thickness direction due to the constraint in the lateral direction. For a thin film with its thickness dimension much smaller than its lateral dimensions, the swelling deformation is homogeneous, but anisotropic. Let 1 and 3 be the in-plane coordinates and 2 the out-of-plane coordinate. Under the lateral constraint, the principal stretches of the

hydrogel thin film are: $\lambda_1 = \lambda_3 = 1$ and $\lambda_2 > 1$. The constraint induces a biaxial compressive stress in the film, i.e., $s_1 = s_3 = s < 0$, while the other principal stress is zero, i.e., $s_2 = 0$, as the top surface of the film is assumed to be traction-free. By Eq. (2.34), the Lagrange multiplier is obtained as

$$\Pi = Nk_B T \left(\lambda_2 - \frac{1}{\lambda_2} \right), \quad (2.39)$$

The chemical potential is then obtained from Eq. (2.35) as

$$\mu = \frac{\partial U}{\partial C} = k_B T \left[\ln \left(1 - \frac{1}{\lambda_2} \right) + \frac{1}{\lambda_2} + \frac{\chi}{\lambda_2^2} + N\nu \left(\lambda_2 - \frac{1}{\lambda_2} \right) \right], \quad (2.40)$$

where the condition of molecular incompressibility, $\nu C = \lambda_2 - 1$, has been incorporated.

Thus, by setting $\mu = \hat{\mu}$ in Eq. (2.40), we can solve for the equilibrium swelling ratio λ_2 for the hydrogel film as a function of the external chemical potential. The swelling-induced stress in the hydrogel film is then obtained from Eq. (2.34) as

$$s_1 = s_3 = s = -Nk_B T (\lambda_2^2 - 1). \quad (2.41)$$

For a hydrogel film with $\chi = 0.1$ and $N\nu = 10^{-3}$, the swelling ratio is plotted in Fig. 2.2 as a function of the chemical potential. The equilibrium swelling ratio at $\mu = \hat{\mu} = 0$ is $\lambda_2 = 7.696$. Compared to the isotropic, free swelling hydrogel ($\lambda = 3.390$ and $J = \lambda^3 = 38.96$), the hydrogel film will stretch further in the thickness direction, while its volume swelling ratio ($J = \lambda_2 = 7.696$) is much smaller, as a result of the lateral constraint.

2.3.3. Anisotropic, homogeneous swelling of a hydrogel line

As another example, we consider swelling of a hydrogel line. Assume that the longitudinal dimension of the line is much larger than its lateral dimensions. Swelling of such a long line is constrained in the longitudinal direction, and thus $\lambda_3 = 1$. On the other hand, swelling in the lateral directions is unconstrained and isotropic, with $\lambda_1 = \lambda_2 = \lambda > 1$. Such a constrained swelling induces a compressive longitudinal stress in the line: $s_3 < 0$, whereas $s_1 = s_2 = 0$. From Eq. (2.34), the Lagrange multiplier in the hydrogel line is

$$\Pi = Nk_B T \left(1 - \frac{1}{\lambda^2} \right). \quad (2.42)$$

The chemical potential in the hydrogel line is obtained from Eq. (2.35) as

$$\mu = \frac{\partial U}{\partial C} = k_B T \left[\ln \left(1 - \frac{1}{\lambda^2} \right) + \frac{1}{\lambda^2} + \frac{\chi}{\lambda^4} + N\nu \left(1 - \frac{1}{\lambda^2} \right) \right], \quad (2.43)$$

where the condition of molecular incompressibility, $\nu C = \lambda^2 - 1$, has been applied. Thus, by setting $\mu = \hat{\mu}$ in Eq. (2.43), we can solve for the equilibrium swelling ratio λ in the lateral direction for the hydrogel line as a function of the external chemical potential. The swelling-induced longitudinal stress in the hydrogel line is then obtained from Eq. (2.34) as

$$s_3 = -Nk_B T (\lambda^2 - 1). \quad (2.44)$$

The analytical solutions for the swelling ratio are plotted in Fig. 2.2 for a hydrogel line with $\chi = 0.1$ and $N\nu = 10^{-3}$. The equilibrium swelling ratio of the hydrogel line at

$\mu = \hat{\mu} = 0$ is $\lambda = 4.573$, and the volume swelling ratio is $J = \lambda^2 = 20.92$. Since the longitudinal constraint (1D) in the hydrogel line is weaker than the lateral constraint (2D) in the hydrogel film, the volume ratio of the line is greater than that of the film ($J = \lambda_2 = 7.696$), but still smaller than that of the unconstrained, isotropic swelling ($J = \lambda^3 = 38.96$).

2.3.4. Effect of environmental pressure

While the external pressure of the solvent is typically small and negligible up to the equilibrium vapor pressure, the pressure in principle can become significant in the liquid phase ($p > p_0$ and $\hat{\mu} > 0$). By neglecting the external pressure, the solution in the previous sections would predict increasing swelling for positive chemical potential ($\hat{\mu} > 0$). However, this is not the case when the solvent pressure is taken into account, as discussed below.

Consider a hydrogel film bonded to a rigid substrate and surrounded by a solution with a pressure p . The problem is same as in section 2.3.2 except $s_2 = -p$. Then the Lagrange multiplier is

$$\Pi = Nk_B T \left(\lambda_2 - \frac{1}{\lambda_2} \right) + p. \quad (2.45)$$

This equation has the additional term p because of the external solvent pressure. This term can be replaced with the vapor pressure and the chemical potential by using Eq. (2.24). After that, substituting Eq. (2.45) into Eq. (2.35) gives the following equation for the chemical potential and the swelling ratio:

$$\ln\left(1 - \frac{1}{\lambda_2}\right) + \frac{1}{\lambda_2} + \frac{\chi}{\lambda_2^2} + Nv\left(\lambda_2 - \frac{1}{\lambda_2}\right) = \bar{\mu} - \bar{p}_0 \exp(\bar{\mu}) \quad \text{if } p \leq p_0 \text{ or } \hat{\mu} \leq 0 \quad (2.46)$$

$$\ln\left(1 - \frac{1}{\lambda_2}\right) + \frac{1}{\lambda_2} + \frac{\chi}{\lambda_2^2} + Nv\left(\lambda_2 - \frac{1}{\lambda_2}\right) = -\bar{p}_0 \quad \text{if } p \geq p_0 \text{ or } \hat{\mu} \geq 0 \quad (2.47)$$

where $\bar{p}_0 = \frac{p_0 v}{k_B T}$, $\bar{\mu} = \frac{\hat{\mu}}{k_B T}$. Comparison of Eqs. (2.46) and (2.47) with Eq. (2.40) reveals

that the swelling ratio becomes dependent both on the vapor pressure and the chemical potential when the solvent is in the gaseous phase, and for the liquid phase solution, once the swelling ratio reaches the equilibrium swelling ratio ($p = p_0$), it does not increase anymore.

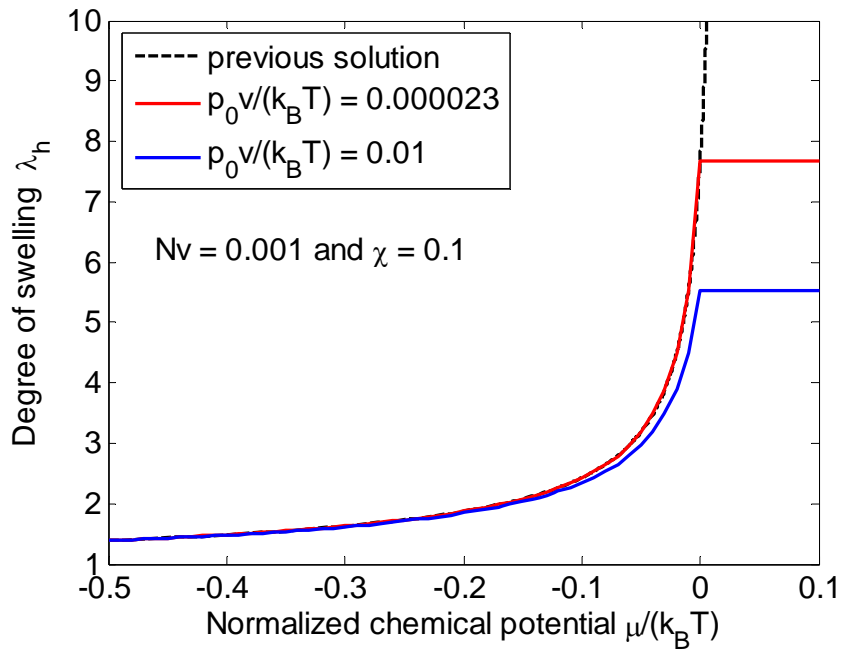
The principal nominal stresses are

$$s_{11} = s_{33} = -Nk_B T(\lambda_2^2 - 1) - p\lambda_2 \quad \text{and} \quad s_{22} = -p. \quad (2.48)$$

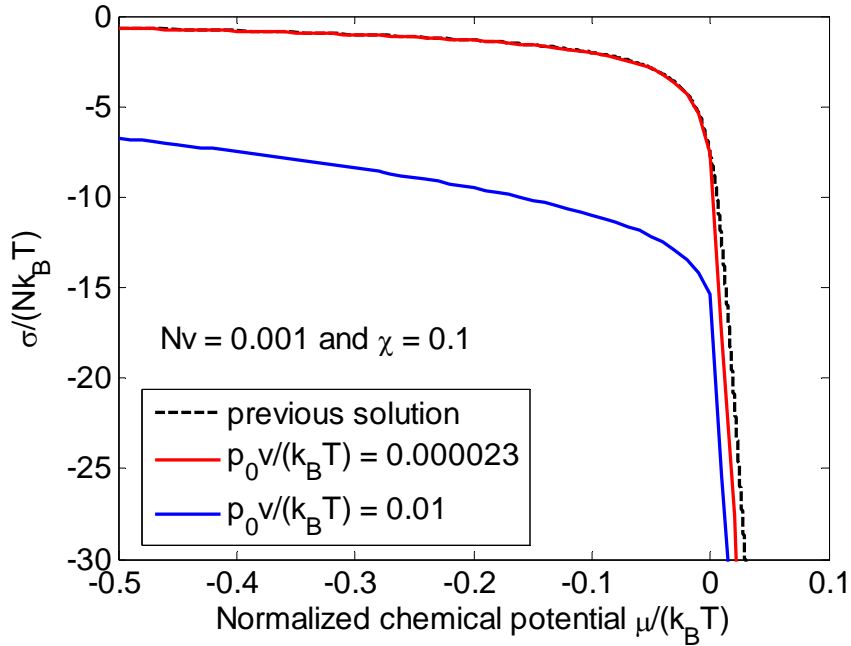
The true stresses are

$$\sigma_{11} = \sigma_{33} = s_{11} / \lambda_2 = -Nk_B T(\lambda_2 - 1/\lambda_2) - p \quad \text{and} \quad \sigma_{22} = s_{22} = -p. \quad (2.49)$$

Figure 2.3 plots the swelling ratio and induced in-plane stress in comparison with the previous solution (Section 2.3.2). The external solvent is water at room temperature whose vapor pressure is about 3.2kPa and the normalized vapor pressure is about 0.000023. It is clearly shown that at room temperature, for the chemical potential less than zero, consideration of the environmental pressure does not give much difference. However, for positive chemical potential, Eq. (2.40) yields drastic increase in swelling ratio while Eq. (2.47) shows that the swelling of a hydrogel body remains the same as the swelling at zero chemical potential or the equilibrium swelling ratio.



(a)



(b)

Figure 2.3: Effect of external solvent pressure on homogeneous swelling of a hydrogel film; (a) The swelling ratio, (b) The normalized in-plane true stress.

The blue curve with a much larger vapor pressure is added to show a trend of the vapor pressure effect. The trend is that as the vapor pressure increases, the swelling ratio decreases in an insensitive manner. The stresses in the in-plane direction due to the constraint are plotted in Fig. 2.3 (b) with and without the solvent pressure. Up to the equilibrium swelling state ($\mu = 0$), the effect of the solvent pressure does not make any noticeable difference, but beyond the equilibrium state, consideration of pressure increases stress due to pressure increase, whereas the previous solution shows stress increase due to swelling increase, which does not appear when the pressure is taken into consideration. From the current example, it can be said that at about room temperature, disregarding the environmental pressure does not lead to erroneous result if we focus only on the swelling ratio. But for stress calculation for positive chemical potential or liquid phase solvent, the pressure should be considered.

Similarly, for 3-D free, isotropic swelling in Section 2.3.1, we now have $\lambda_1 = \lambda_2 = \lambda_3 = \lambda$ and $s_1 = s_2 = s_3 = -p\lambda^2$. Then the Lagrange multiplier and the chemical potential can be obtained from Eqs. (2.34) and (2.35),

$$\Pi = Nk_B T \left(\frac{1}{\lambda} - \frac{1}{\lambda^3} \right) + p, \quad (2.50)$$

$$\mu - pv = k_B T \left[\ln \frac{\lambda^3 - 1}{\lambda^3} + \frac{1}{\lambda^3} + \frac{\chi}{\lambda^6} + Nv \left(\frac{1}{\lambda} - \frac{1}{\lambda^3} \right) \right]. \quad (2.51)$$

Substitution of the definition of the chemical potential from Eq. (2.24) into Eq. (2.51) leads to the following equations.

$$\ln \frac{\lambda^3 - 1}{\lambda^3} + \frac{1}{\lambda^3} + \frac{\chi}{\lambda^6} + Nv \left(\frac{1}{\lambda} - \frac{1}{\lambda^3} \right) = \bar{\mu} - \bar{p}_0 \exp(\bar{\mu}) \quad \text{if } p \leq p_0 \text{ or } \hat{\mu} \leq 0 \quad (2.52)$$

$$\ln \left(\frac{\lambda^3 - 1}{\lambda^3} \right) + \frac{1}{\lambda^3} + \frac{\chi}{\lambda^6} + Nv \left(\frac{1}{\lambda} - \frac{1}{\lambda^3} \right) = -\bar{p}_0 \quad \text{if } p \geq p_0 \text{ or } \hat{\mu} \geq 0 \quad (2.53)$$

For a hydrogel with $Nv = 0.001$, $\chi = 0.1$, and $\bar{p}_0 = 0.000023$, the calculated equilibrium swelling ratio is $\lambda = 3.338$ which shows slight decrease from the previous result $\lambda = 3.390$ (assuming $p_0 = 0$).

2.4. A NONLINEAR FINITE ELEMENT METHOD

Simple, analytical solutions can be obtained for homogeneous swelling of hydrogels from the above theoretical framework. For inhomogeneous swelling with complex geometrical and physical constraints, however, numerical approaches are often necessary [57, 82, 98]. With the variational form of the present theory, a finite element method may be developed to solve the coupled field equations in Eq. (2.22). Alternatively, following Hong et al. [57], a Legendre transformation of the free energy density function leads to

$$\hat{U}(\mathbf{F}, \mu) = U(\mathbf{F}, C) - \mu C, \quad (2.54)$$

which can then be used to solve for the equilibrium swelling deformation with a prescribed chemical potential μ . Since the chemical potential must be a constant in the equilibrium state ($\mu = \hat{\mu}$), a standard nonlinear finite element method for hyperelasticity [99] can be employed to solve for the equilibrium swelling deformation field (\mathbf{F}). The

concentration field (C), which is inhomogeneous in general, can then be obtained from the condition of molecular incompressibility, i.e., $C = (J-1)/\nu$.

Substituting the free energy function in Eq. (2.25) into Eq. (2.54) and replacing νC with $J-1$, we obtain that

$$\hat{U}(\mathbf{F}, \mu) = \frac{1}{2} N k_B T (I - 3 - 2 \ln J) + \frac{k_B T}{\nu} \left[(J-1) \ln \frac{J-1}{J} + \chi \frac{J-1}{J} \right] - \frac{\mu}{\nu} (J-1) \quad (2.55)$$

where $I = F_{iK} F_{iK}$. In the undeformed dry state, we have $J = 1$ and $I = 3$ so that $\hat{U} = 0$. However, the chemical potential in the dry state is singular ($\mu = -\infty$), which cannot be accurately specified for numerical simulations. To circumvent this inconvenience, an auxiliary configuration with a finite value of the chemical potential is used as the initial state in numerical simulations, as illustrated in Fig. 2.4. The choice of the initial state should be such that (a) the corresponding swelling deformation is homogeneous, and (b) the essential boundary conditions in the dry state are satisfied. The condition (a) allows the chemical potential in the initial state to be obtained analytically, and the condition (b) ensures that the effect of constraints on swelling by the essential boundary conditions is maintained in the initial state and throughout the subsequent swelling process. In a previous study [57], a free, isotropic swelling deformation was assumed for the initial state, which does not necessarily satisfy the condition (b) for swelling of hydrogels under geometric constraints. In the present study, we choose an initial state with swelling deformation in form of

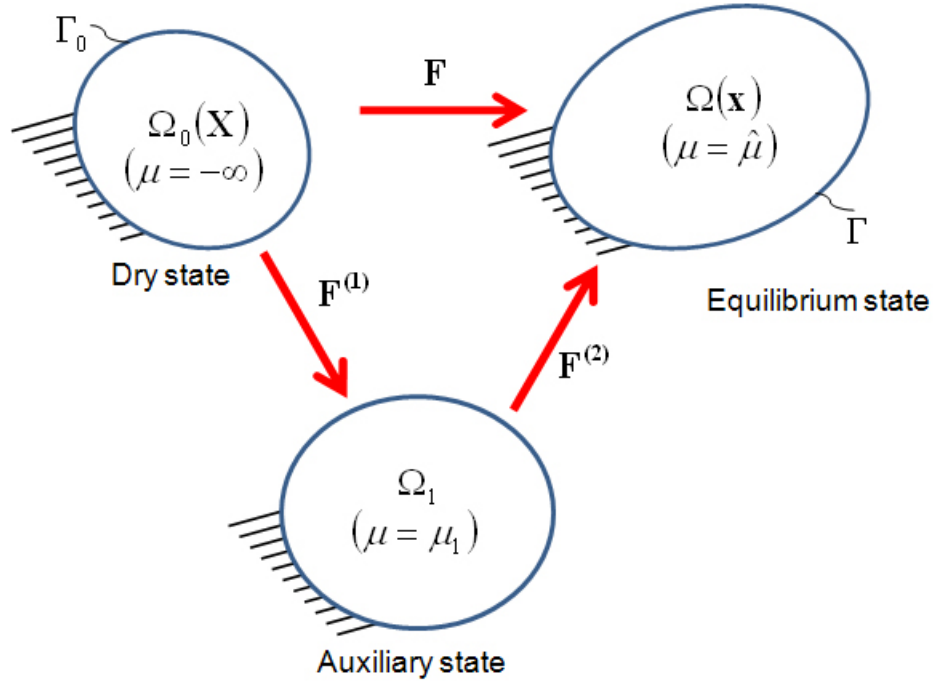


Figure 2.4: Schematic illustration of the reference state (dry) and the equilibrium state (swollen) of a hydrogel, along with an auxiliary initial state used in numerical simulations.

$$\mathbf{F}^{(1)} = \begin{bmatrix} \lambda_1^{(1)} & 0 & 0 \\ 0 & \lambda_2^{(1)} & 0 \\ 0 & 0 & \lambda_3^{(1)} \end{bmatrix}. \quad (2.56)$$

The three principal stretches in the initial state and the corresponding chemical potential ($\mu = \mu_1$) depend on specific constraints imposed by the essential boundary conditions, as will be discussed in the next section.

As illustrated in Fig. 2.4, the total swelling deformation from the dry state is expanded into two parts as:

$$\mathbf{F} = \mathbf{F}^{(2)}\mathbf{F}^{(1)}, \quad (2.57)$$

where $\mathbf{F}^{(2)}$ is the deformation gradient from the initial state ($\mu = \mu_1$) to the final state of equilibrium ($\mu = \hat{\mu}$) and is to be solved numerically by the finite element method.

The nonlinear constitutive behavior of a hydrogel can be specified as a user-defined material in a standard finite element package such as ABAQUS [100]. In particular, ABAQUS offers two options for such an implementation, with the user subroutine UHYPER or UMAT. The former (UHYPER) is specialized for hyperelastic materials, but with the restriction that the initial state must be isotropic. Assuming isotropic swelling in the initial state, a user subroutine with UHYPER was developed previously [57]. In the present study, with a generally anisotropic initial state as given in Eq. (2.56), we develop an alternative implementation for swelling of hydrogels under constraints using the user subroutine UMAT in ABAQUS. As a general material subroutine, the procedures for UMAT implementation are quite different from those for UHYPER. In the UHYPER subroutine, the free energy function and its derivatives with respect to the deviatoric strain invariants are coded [57]. The restriction of such an implementation to an isotropic initial state results from the decomposition of the deformation gradient into a volumetric part and a deviatoric part. The present implementation using UMAT removes this restriction, but requires lengthy derivation of an explicit formula for the true (Cauchy) stress and its variation with respect to the current state in terms of a fourth-order tangent modulus tensor.

First, the nominal stress is obtained as

$$s_{iK} = \frac{\partial \hat{U}}{\partial F_{iK}} = \frac{\partial \hat{U}}{\partial I} \frac{\partial I}{\partial F_{iK}} + \frac{\partial \hat{U}}{\partial J} \frac{\partial J}{\partial F_{iK}}. \quad (2.58)$$

By definition, the Kirchoff stress is

$$J\sigma_{ij} = s_{iK}F_{jK} = \left(\frac{\partial \hat{U}}{\partial I} \frac{\partial I}{\partial F_{iK}} + \frac{\partial \hat{U}}{\partial J} \frac{\partial J}{\partial F_{iK}} \right) F_{jK}, \quad (2.59)$$

where σ_{ij} is the true stress in the current state. Using the free energy function in Eq. (2.55), we obtain that

$$\frac{\partial \hat{U}}{\partial I} = \frac{1}{2} Nk_B T, \quad (2.60)$$

$$\frac{\partial \hat{U}}{\partial J} = Nk_B T \left[-\frac{1}{J} + \frac{1}{N\nu} \left(\ln \frac{J-1}{J} + \frac{1}{J} + \frac{\chi}{J^2} - \frac{\mu}{k_B T} \right) \right]. \quad (2.61)$$

Furthermore, it can be shown that

$$\frac{\partial I}{\partial F_{iK}} = 2F_{iK} \quad \text{and} \quad \frac{\partial J}{\partial F_{iK}} = \frac{1}{2} e_{ijk} e_{kQR} F_{jQ} F_{kR}. \quad (2.62)$$

Substituting Eqs. (2.60-2.62) into Eq. (2.59), we obtain an explicit formula for the true stress:

$$\sigma_{ij} = Nk_B T \left[J^{-\frac{1}{3}} \bar{B}_{ij} + \frac{\delta_{ij}}{N\nu} \left(\ln \frac{J-1}{J} + \frac{1-N\nu}{J} + \frac{\chi}{J^2} - \frac{\mu}{k_B T} \right) \right], \quad (2.63)$$

where $\bar{B}_{ij} = J^{-2/3} F_{iK} F_{jK}$ is the deviatoric stretch tensor and δ_{ij} is the Kronecker delta.

Next, variation of the Kirchoff stress gives that

$$\delta(J\sigma_{ij}) = Nk_B T \left[\frac{2}{3} J^{-\frac{1}{3}} \bar{B}_{ij} \delta J + J^{\frac{2}{3}} \delta \bar{B}_{ij} + \frac{\delta_{ij}}{N\nu} \left(\ln \frac{J-1}{J} + \frac{1}{J-1} - \frac{\chi}{J^2} - \frac{\mu}{k_B T} \right) \delta J \right]. \quad (2.64)$$

It can be shown that

$$\delta J = J \delta D_{kk}, \quad (2.65)$$

$$\delta\bar{B}_{ij} = H_{ijkl} \left(\delta D_{kl} - \frac{\delta_{kl}}{3} \delta D_{mm} \right) + \bar{B}_{kj} \delta W_{ik} - \bar{B}_{ik} \delta W_{kj}, \quad (2.66)$$

where

$$\delta D_{ij} = \frac{1}{2} (\delta L_{ij} + \delta L_{ji}), \quad (2.67)$$

$$\delta W_{ij} = \frac{1}{2} (\delta L_{ij} - \delta L_{ji}), \quad (2.68)$$

$$\delta L_{ij} = \frac{\partial}{\partial x_j} (\delta u_i), \quad (2.69)$$

$$H_{ijkl} = \frac{1}{2} (\bar{B}_{jl} \delta_{ik} + \bar{B}_{ik} \delta_{jl} + \bar{B}_{jk} \delta_{il} + \bar{B}_{il} \delta_{jk}). \quad (2.70)$$

In the above, δu_i is the variation displacement, δD_{ij} is the symmetric part of the deformation gradient, and δW_{ij} is the antisymmetric part (spin), all of which are variational quantities with respect to the current state.

By substituting Eqs. (2.65) and (2.66) into Eq. (2.64), we obtain that

$$\delta(J\sigma_{ij}) = J C_{ijkl} \delta D_{kl} + J (\sigma_{kj} \delta W_{ik} - \sigma_{ik} \delta W_{kj}), \quad (2.71)$$

where an explicit formula for the tangent modulus tensor in the current state is obtained

as

$$C_{ijkl} = N k_B T \left[J^{-\frac{1}{3}} H_{ijkl} + \frac{1}{N_V} \left(\ln \frac{J-1}{J} + \frac{1}{J-1} - \frac{\chi}{J^2} - \frac{\mu}{k_B T} \right) \delta_{ij} \delta_{kl} \right]. \quad (2.72)$$

The second term on the right-hand side of Eq. (2.71) results from rotation of the local coordinates, which is not needed in the material subroutine [100]. The first term on the

right-hand side of Eq. (2.72) gives the tangent modulus for an incompressible, neo-Hookean material.

With Eqs. (2.63) and (2.72) for the true stress and tangent modulus, a user subroutine is coded in the format of UMAT in ABAQUS which is given in Appendix A. Following Hong et al. [57], the chemical potential is mimicked by a temperature-like quantity in the user subroutine, which is set to be a constant in the hydrogel in the equilibrium state. Analogous to thermally induced deformation, change of the chemical potential leads to swelling deformation of the hydrogel, and stress is induced if it is subject to any constraint. Several numerical examples are presented in the next section for homogeneous and inhomogeneous swelling of hydrogels. For convenience, we normalize the key quantities as follows:

$$\bar{U} = \frac{\hat{U}}{Nk_B T}, \quad \bar{\sigma}_{ij} = \frac{\sigma_{ij}}{Nk_B T}, \quad \bar{\mu} = \frac{\mu}{k_B T}. \quad (2.73)$$

2.5. NUMERICAL EXAMPLES

With the finite element method, numerical simulations are performed for both homogeneous and inhomogeneous swelling. The results for the three homogeneous swelling cases are compared with the analytical solutions (Sections 2.3.1~2.3.3). The effect of geometric constraint is emphasized for the inhomogeneous swelling of surface-attached hydrogel lines of rectangular cross sections.

2.5.1. Free, isotropic swelling

For this case, an isotropic initial state is used with an arbitrary swelling ratio, $\lambda_1^{(1)} = \lambda_2^{(1)} = \lambda_3^{(1)} = 1.5$. The chemical potential in the initial state is calculated analytically from Eq. (2.37). Then, the chemical potential of the hydrogel is increased gradually as the loading parameter in the finite element analysis until $\mu = 0$, and the swelling ratio is calculated at each increment. A single three-dimensional 8-node brick element is used to model the hydrogel, with all boundaries free of traction. The numerical results are compared to the analytical solution in Fig. 2.5, showing excellent agreement. Since the

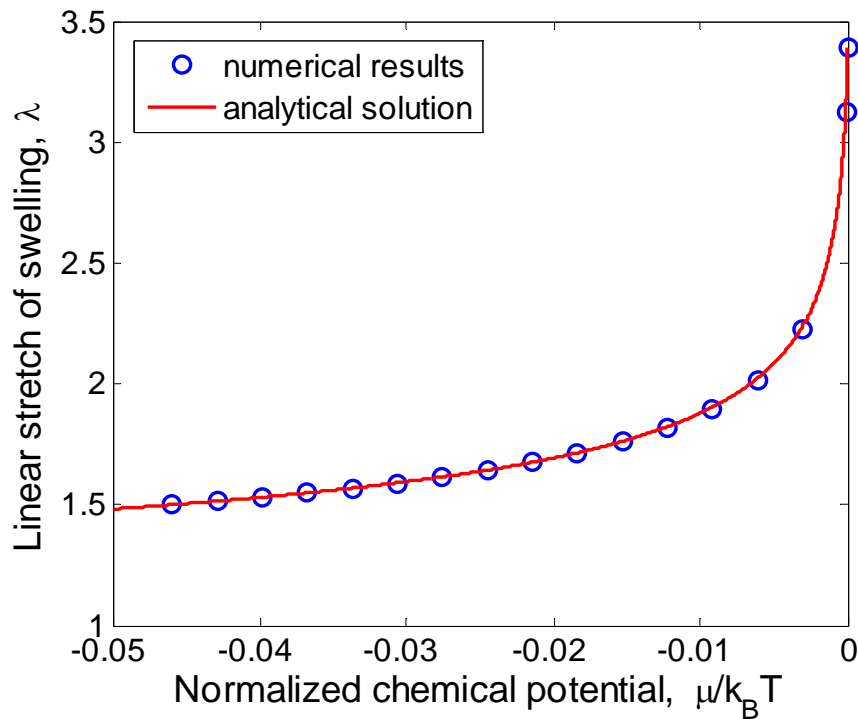
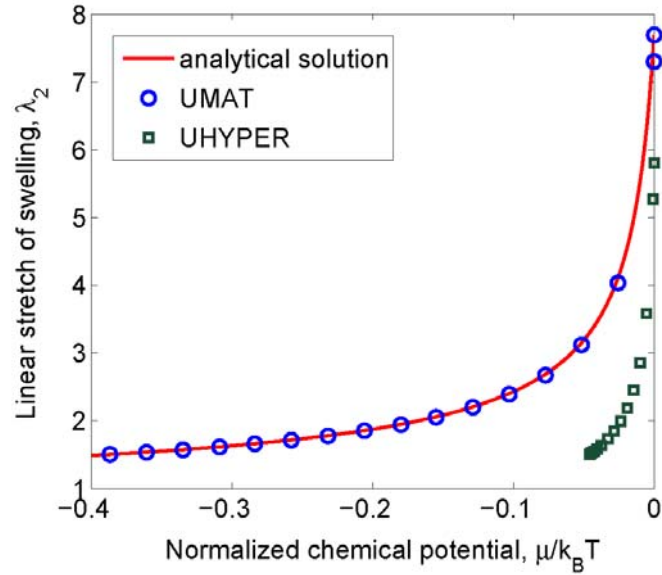


Figure 2.5: Comparison of numerical results with the analytical solution for free, isotropic swelling of a hydrogel.

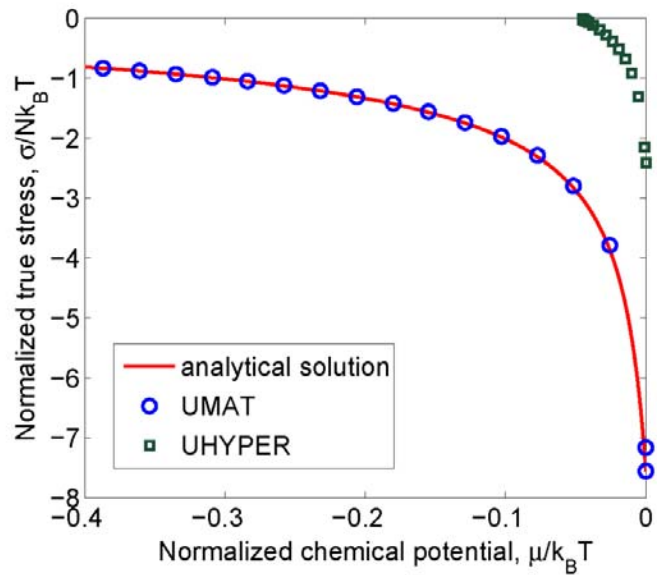
initial state is isotropic in this case, both the UHYPER and UMAT subroutines in ABAQUS can be used, and they produce identical results.

2.5.2. Anisotropic, homogeneous swelling of a hydrogel film

To apply the finite element method for the anisotropic swelling of a hydrogel film, an anisotropic initial state is used, with $\lambda_1^{(1)} = \lambda_3^{(1)} = 1$ and $\lambda_2^{(1)} = 1.5$. The chemical potential in the initial state is calculated analytically from Eq. (2.40). In addition, the swelling-induced stress in the initial state is obtained from Eq. (2.41) and specified by a user subroutine SIGNI in ABAQUS [100]. Either three-dimensional brick elements or two-dimensional plane-strain elements can be used to model the hydrogel film. The lateral constraint on swelling is enforced by the boundary conditions. The numerical results are compared to the analytical solutions in Fig. 2.6, with excellent agreements for both the swelling ratios and the induced stresses as the chemical potential increases. A similar problem was considered by Hong et al. [57] using a UHYPER material subroutine. There, an isotropic initial state with $\lambda_1^{(1)} = \lambda_2^{(1)} = \lambda_3^{(1)} = 1.5$ was used, which relaxed the effect of lateral constraint. The corresponding chemical potential in the isotropic initial state was different from that in Eq. (2.40), and no initial stress was induced. While the subsequent swelling was constrained in the lateral directions, their results are different from the present ones, as shown in Fig. 2.6. In particular, with the use of an isotropic initial state, the results (both swelling ratio and induced stress) for the subsequent swelling under the lateral constraint would depend on the choice of the initial state, and the corresponding analytical solution is different from that in Eqs. (2.39)-

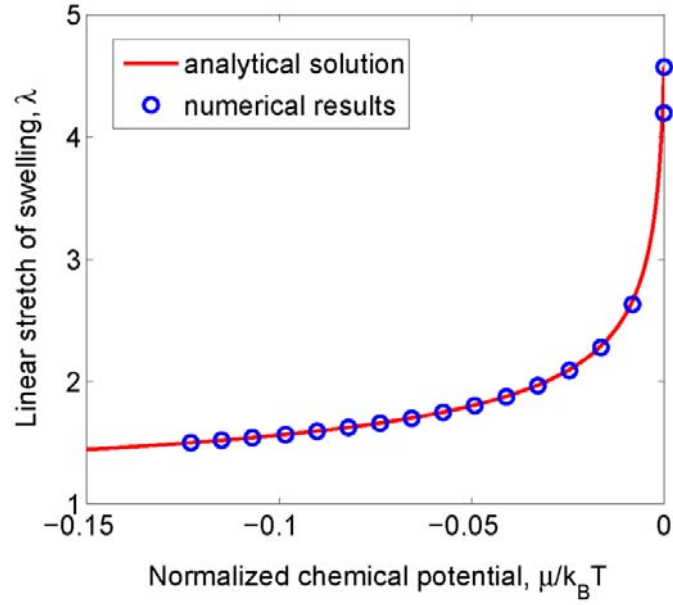


(a)

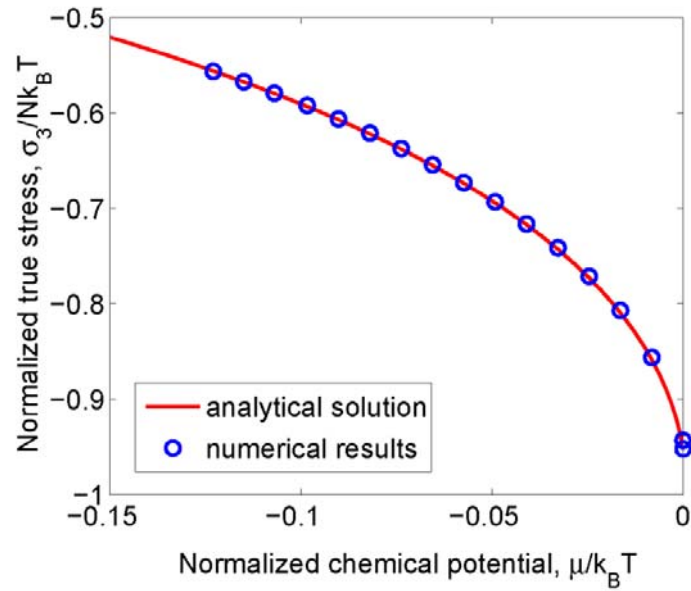


(b)

Figure 2.6: Anisotropic swelling of a hydrogel film under lateral constraint: (a) the swelling ratio in the thickness direction; (b) swelling-induced true stress in the lateral direction. Numerical results from two different implementations (UMAT and UHYPER) are compared to the analytical solution in Eqs. (2.37) and (2.38).



(a)



(b)

Figure 2.7: Anisotropic swelling of a hydrogel line under longitudinal constraint: (a) the swelling ratio in the lateral direction; (b) swelling-induced true stress in the longitudinal direction.

(2.41). With the UMAT implementation and an anisotropic initial state, the present results are independent of the initial state.

Experimental observations of the swelling behavior of hydrogel thin films have shown good agreement with the theoretical predictions [7, 75]. However, at high degrees of swelling, the homogeneous deformation becomes unstable and gives way to inhomogeneous deformation in the form of surface wrinkles or creases [75-76, 80-81, 101].

2.5.3. Anisotropic, homogeneous swelling of a hydrogel line

For the numerical simulation, an anisotropic initial state is assumed with $\lambda_3^{(1)} = 1$ and an arbitrary swelling ratio in the lateral directions, $\lambda_1^{(1)} = \lambda_2^{(1)} = 1.5$. The chemical potential in the initial state is calculated analytically from Eq. (2.43), and the swelling-induced stress in the initial state is obtained from Eq. (2.44) and specified by a user subroutine SIGNI in ABAQUS. The longitudinal constraint on swelling is conveniently imposed by the plane-strain conditions in the finite element analysis using the two-dimensional 4-node elements, with traction-free boundary conditions on the side faces. As shown in Fig. 2.7, the numerical results agree closely with the analytical solutions for both the swelling ratio and the longitudinal stress.

2.5.4. Inhomogeneous swelling of surface-attached hydrogel lines

In this section, we consider swelling of hydrogel lines bonded to a rigid substrate. Polymer lines of this type are commonly used in lithography and imprinting processes for

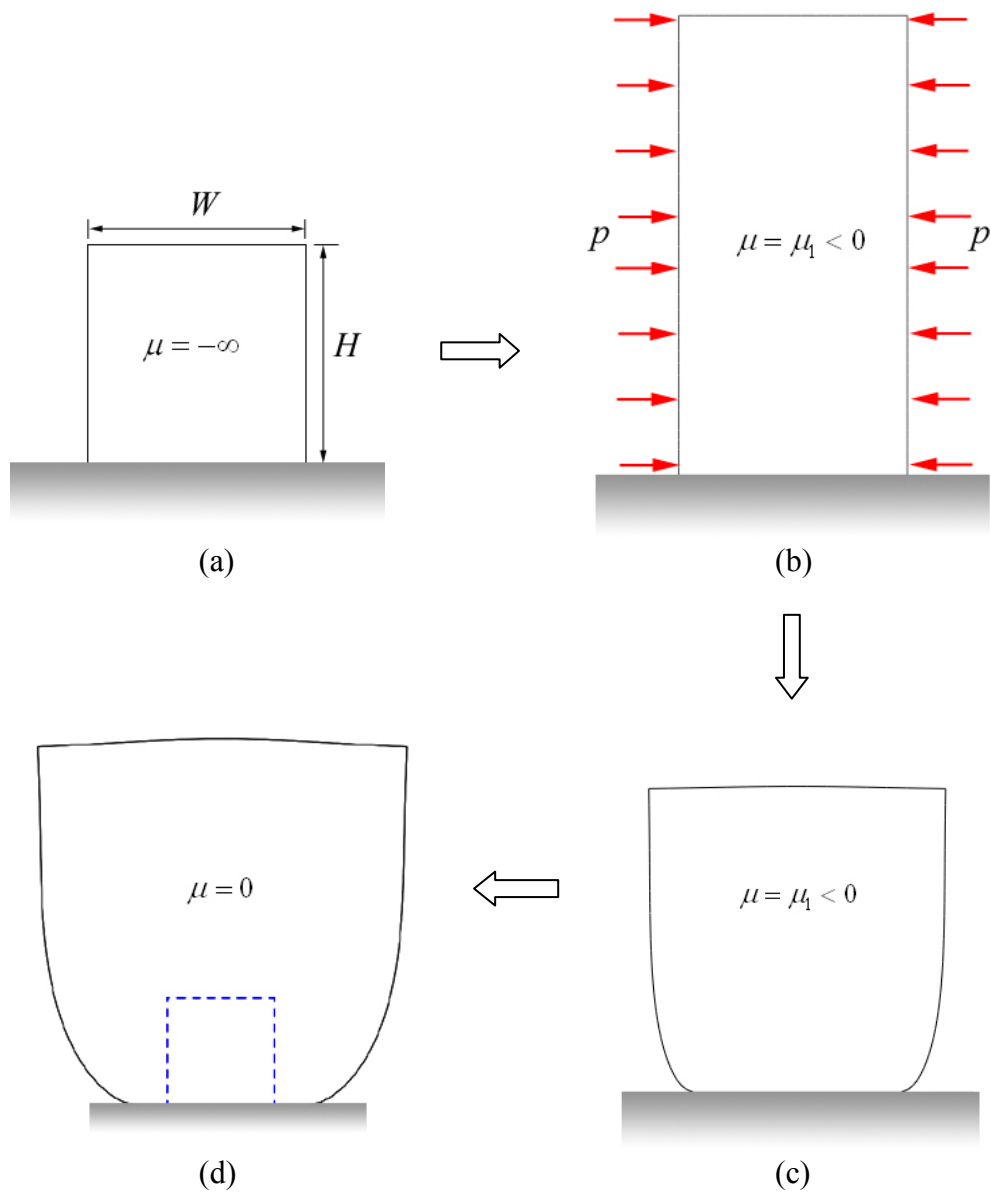


Figure 2.8: Numerical steps to simulate inhomogeneous swelling of a hydrogel line ($W/H = 1$) attached to a rigid substrate: (a) the dry state; (b) the initial state; (c) deformation after releasing the side pressure in (b); (d) equilibrium swelling at $\mu = 0$, with the dashed box as the scaled dry state.

micro/nano-fabrication [78, 102], where large swelling deformation can be detrimental. As we saw in the previous section, the longitudinal dimension of the line is assumed to be much larger than its lateral dimensions so that swelling is constrained in the longitudinal direction with $\lambda_3 = 1$. In addition, the line has a rectangular cross section in the dry state, with one of the side faces bonded to the substrate, as shown in Fig. 2.8 (a). The bonding imposes an additional constraint on the lateral swelling of the line, and the effect of the constraint varies with the width-to-height aspect ratio (W/H) of its cross section.

Swelling deformation of such a surface-attached hydrogel line is typically inhomogeneous, which offers a model system for the study of the constraint effect between two homogeneous limits: (i) When $W/H \rightarrow \infty$, the swelling becomes homogenous, as discussed in Section 2.3.2 for a hydrogel film; (ii) When $W/H \rightarrow 0$, the lateral constraint becomes negligible, and the swelling becomes homogeneous and laterally isotropic, as discussed in Section 2.3.3 for a unattached hydrogel line. Except for the two limiting cases, no analytical solution is available for inhomogeneous swelling of the surface-attached hydrogel lines. To apply the finite element method, we start from an anisotropic initial state of homogeneous swelling with $\lambda_1^{(1)} = \lambda_3^{(1)} = 1$ and an arbitrarily selected swelling ratio in the height direction of the line, e.g., $\lambda_2^{(1)} = 2$ as shown in Fig. 2.8 (b). Such an initial state is identical to that for homogeneous swelling of a hydrogel thin film in Section 2.3.2, for which the chemical potential ($\mu = \mu_1$) can be analytically calculated from Eq. (2.40). With $\lambda_1^{(1)} = \lambda_3^{(1)} = 1$, the longitudinal constraint is maintained and the essential boundary condition at the bottom face of the line is satisfied in the initial

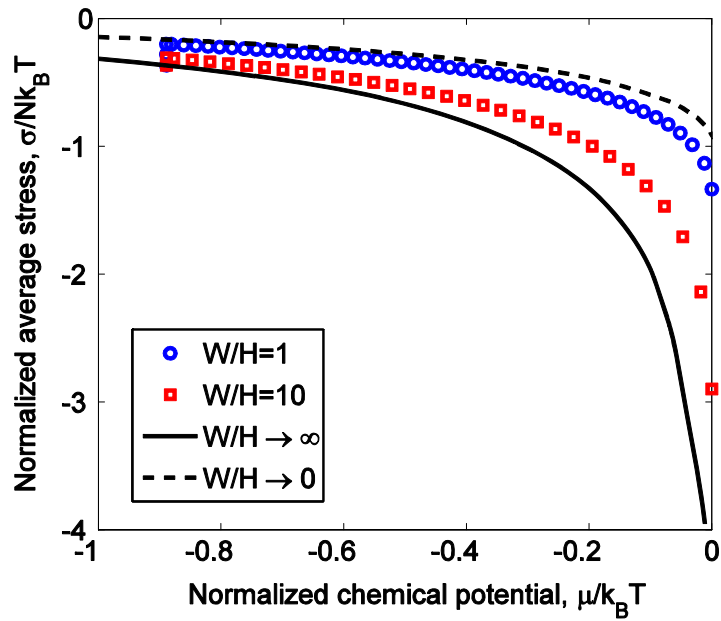
state. However, a compressive stress (or pressure p) has to be applied to the side faces of the line to achieve the homogeneous swelling, which apparently violates the traction-free (natural) boundary condition of the intended problem. The magnitude of the side pressure can be obtained analytically from Eq. (2.41). To recover the traction-free condition on the side faces of the line, we release the side pressure gradually during the first step of numerical simulation, while keeping the chemical potential in the hydrogel unchanged. As illustrated in Fig. 2.8 (c), the release of the side pressure leads to an inhomogeneous deformation of the hydrogel line at the initial chemical potential ($\mu = \mu_1$). Subsequently, further swelling of the hydrogel line is simulated by gradually increasing the chemical potential until $\mu = 0$, as shown in Fig. 2.8 (d).

In all simulations of the present study, the dimensionless material parameters, $N\nu$ and χ , are set to be 0.001 and 0.1, respectively. The dry-state width-to-height aspect ratio (W/H) is varied between 0.1 and 12. A relatively fine finite element mesh is required for simulating inhomogeneous swelling deformation, especially at locations such as the lower corners where a high strain gradient is expected. The use of two-dimensional plane-strain elements is thus warranted by both the computational efficiency and the longitudinal constraint ($\lambda_3 = 1$). The bonding of the bottom face of the hydrogel line to the rigid substrate is mimicked by applying a zero-displacement (essential) boundary condition; debonding of the line is possible but not considered in the present study. Furthermore, the large deformation due to swelling often results in contact of the side

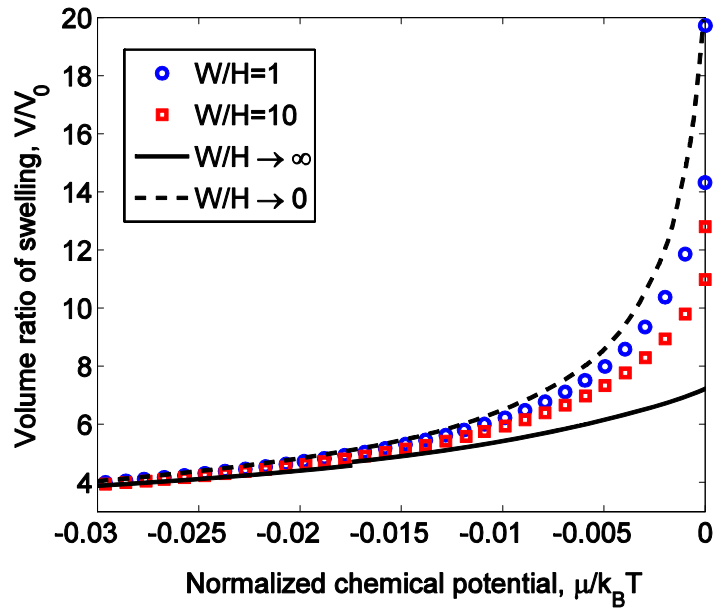
faces of the hydrogel line with the substrate surface, for which hard and frictionless contact properties are assumed in the numerical simulations.

Figure 2.9 (a) plots the average longitudinal stress as a function of the chemical potential for two hydrogel lines with $W/H = 1$ and 10. The analytical solutions at the two limiting cases are also plotted as the upper and lower bounds. In the initial state, we have $\lambda_2^{(1)} = 1.2$ and the corresponding chemical potential, $\bar{\mu}_1 = -0.8886$. The initial longitudinal stress is identical to that in a hydrogel film ($W/H \rightarrow \infty$), which can be obtained from Eq. (2.41) and lies on the solid line in Fig. 2.9 (a). Upon release of the side pressure in the initial state, the magnitude of the average longitudinal stress is reduced while the chemical potential remains at the initial value. From the same initial state, the reduced stress magnitudes are different for the two hydrogel lines, higher in the line with $W/H = 10$ than in the line with $W/H = 1$, due to stronger constraint in the line with the larger aspect ratio. Subsequently, as the chemical potential increases, the magnitudes of the average longitudinal stress in both the hydrogel lines increase. All the numerical results lie between the two homogeneous limits, while the stress magnitude increases with the aspect ratio W/H at the same chemical potential.

Figure 2.9 (b) plots the volume swelling ratios for the two hydrogel lines as the chemical potential approaches $\mu = 0$. The volume ratios increase as the chemical potential increases. The difference in the volume ratios of the two lines is less appreciable until the chemical potential is close to zero. Again, the two analytical limits set the upper and lower bounds for the volume swelling ratios of the surface-attached hydrogel lines.



(a)



(b)

Figure 2.9: Inhomogeneous swelling of surface-attached hydrogel lines: (a) average longitudinal stress; (b) volume ratio of swelling. The solid and dashed lines are analytical solutions for the homogeneous limits with $W/H \rightarrow \infty$ and $W/H \rightarrow 0$, respectively.

The larger the W/H aspect ratio, the stronger the constraint effect and thus the smaller the volume ratio of swelling is observed at the same chemical potential.

The inhomogeneous swelling deformation along with the distribution of the longitudinal stress at the equilibrium chemical potential $\mu = 0$ is plotted in Fig. 2.10 for three hydrogel lines with $W/H = 1, 5,$ and 10 . For each line, the cross section at the dry state is outlined by a small rectangular box. The large swelling deformation pushes the side faces of the hydrogel lines to form contact with the rigid substrate surface. The contact length increases as the aspect ratio increases, reaching a full contact of the side faces for the hydrogel line with $W/H = 10$. The stress contours show stress concentration at the bottom corners, where debonding may occur. We note that the magnitude of the stress in Fig. 2.10 is normalized by $Nk_B T$, which is typically in the range of $10^4 \sim 10^7$ Pa for polymeric hydrogels at room temperature. To further illustrate the effect of geometric constraint on swelling, Figure 2.11 plots the equilibrium swelling ratio at $\mu = 0$ as a function of the dry-state width-to-height aspect ratio (W/H) of the hydrogel lines. The two analytical limits are plotted as dashed lines. As the aspect ratio decreases, the effect of constraint by the substrate diminishes, and the volume ratio approaches that for the homogeneous swelling of a hydrogel line without any lateral constraint (upper bound). On the other hand, as the aspect ratio increases, the volume ratio decreases due to increasing constraint by the substrate, approaching the other limit for the homogeneous swelling of a hydrogel film (lower bound). Therefore, the degree of swelling can be tuned between the two homogeneous limits by varying the geometric aspect ratio of the surface-attached hydrogel lines.

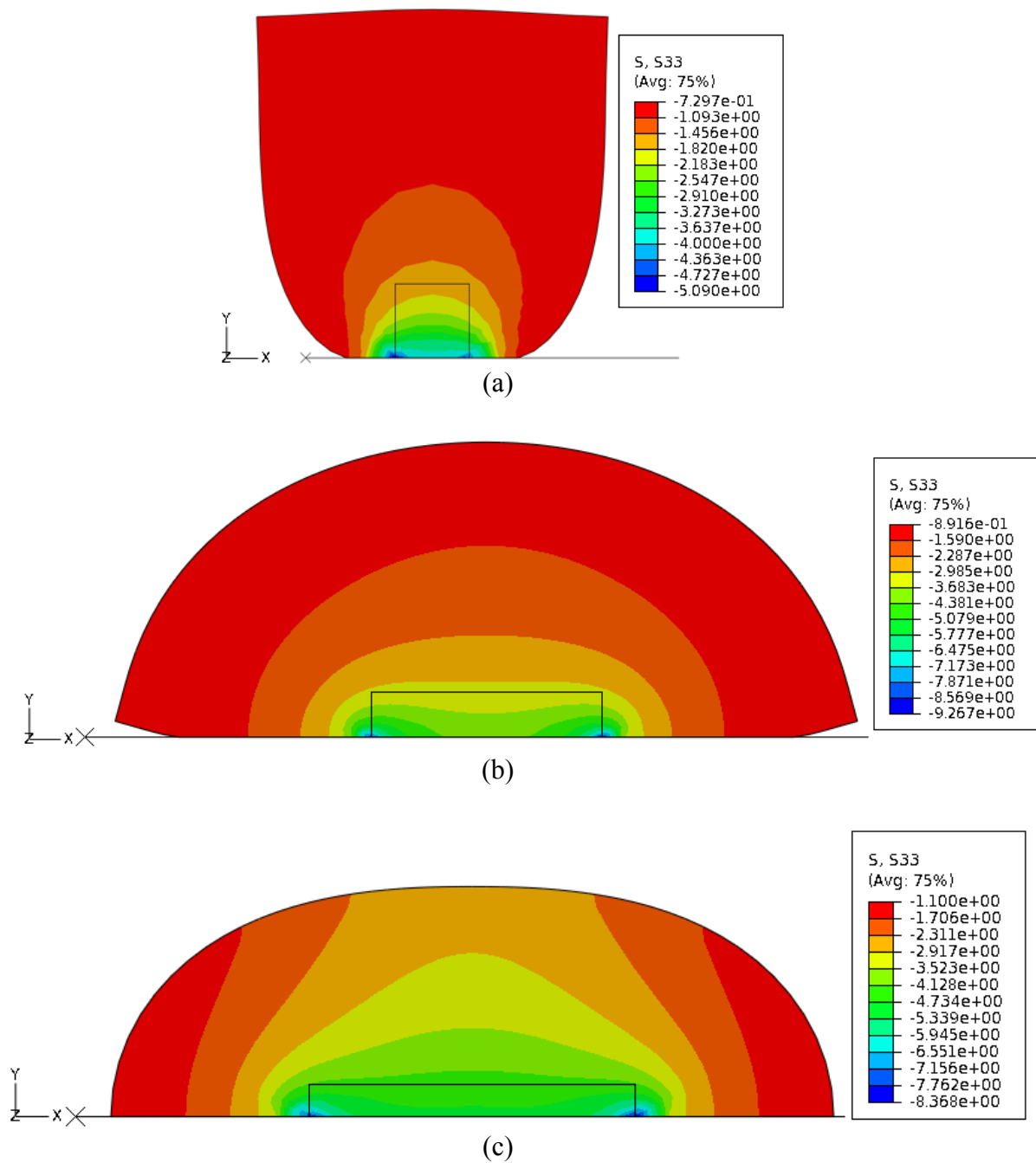


Figure 2.10: Simulated swelling deformation and longitudinal stress distribution in surface-attached hydrogel lines of different aspect ratios: (a) $W/H = 1$; (b) $W/H = 5$; (c) $W/H = 10$. The rectangular boxes outline the cross sections in the dry state.

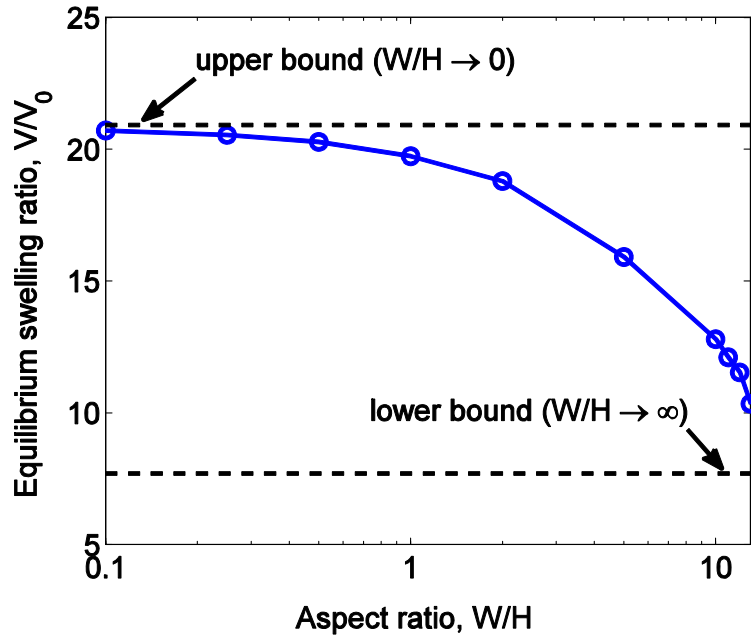


Figure 2.11: Equilibrium volume ratio as a function of the dry-state width-to-height aspect ratio for inhomogeneous swelling of surface-attached hydrogel lines.

As the W/H aspect ratio increases beyond 10, swelling deformation of the hydrogel line becomes highly constrained and induces an increasingly large compressive stress in the top surface. It is found that, at a critical aspect ratio, a surface instability develops, as shown in Fig. 2.12 for $W/H = 12$. As the chemical potential increases, the top surface of the hydrogel line evolves from nearly flat to slightly undulated, and eventually develops two crease-like foldings with self-contact of the top surface. The stress contours show stress concentration at the tip of the creases. More creases are observed in the simulation for a hydrogel line with the aspect ratio $W/H = 13$. However, the numerical simulation becomes increasingly unstable with formation of the surface

creases, posing a numerical challenge for simulations of hydrogel lines with higher aspect ratios.

The formation of surface creases has been observed experimentally in swelling gels [75-76, 81, 101] as well as in rubbers under mechanical compression [85, 103]. A linear perturbation analysis by Biot [84] showed that homogeneous deformation of a rubber under compression becomes unstable at a critical strain, which is about 0.46 under plane-strain compression and about 0.33 under equi-biaxial compression. However, the theoretical prediction for the plane-strain compression was found to exceed the experimentally determined critical strain (~ 0.35) for rubbers [85]. In a recent experimental study of surface-attached hydrogel thin films [81], an effective linear compressive strain of ~ 0.33 was obtained for the onset of creasing for laterally constrained hydrogels. While this effective critical strain is remarkably close to Biot's prediction for rubbers under equi-biaxial compression, the critical condition for the onset of swell-induced creasing in hydrogels has not been established theoretically. A few recent efforts are noted [75-82, 86, 101, 104]. The present study of the surface-attached hydrogel lines demonstrates an alternative approach. Typically for theoretical and numerical studies of surface instability, it is necessary to introduce perturbations to the reference homogeneous solution to trigger the instability. In the present study, surface creases form automatically in the numerical simulations for hydrogel lines beyond the critical aspect ratio, without any perturbation. Our numerical simulations show that the critical aspect ratio for the onset of surface instability depends on the external chemical potential and the material parameters of the hydrogel: $(W/H)_c = f(\bar{\mu}, N\nu, \chi)$. Therefore,

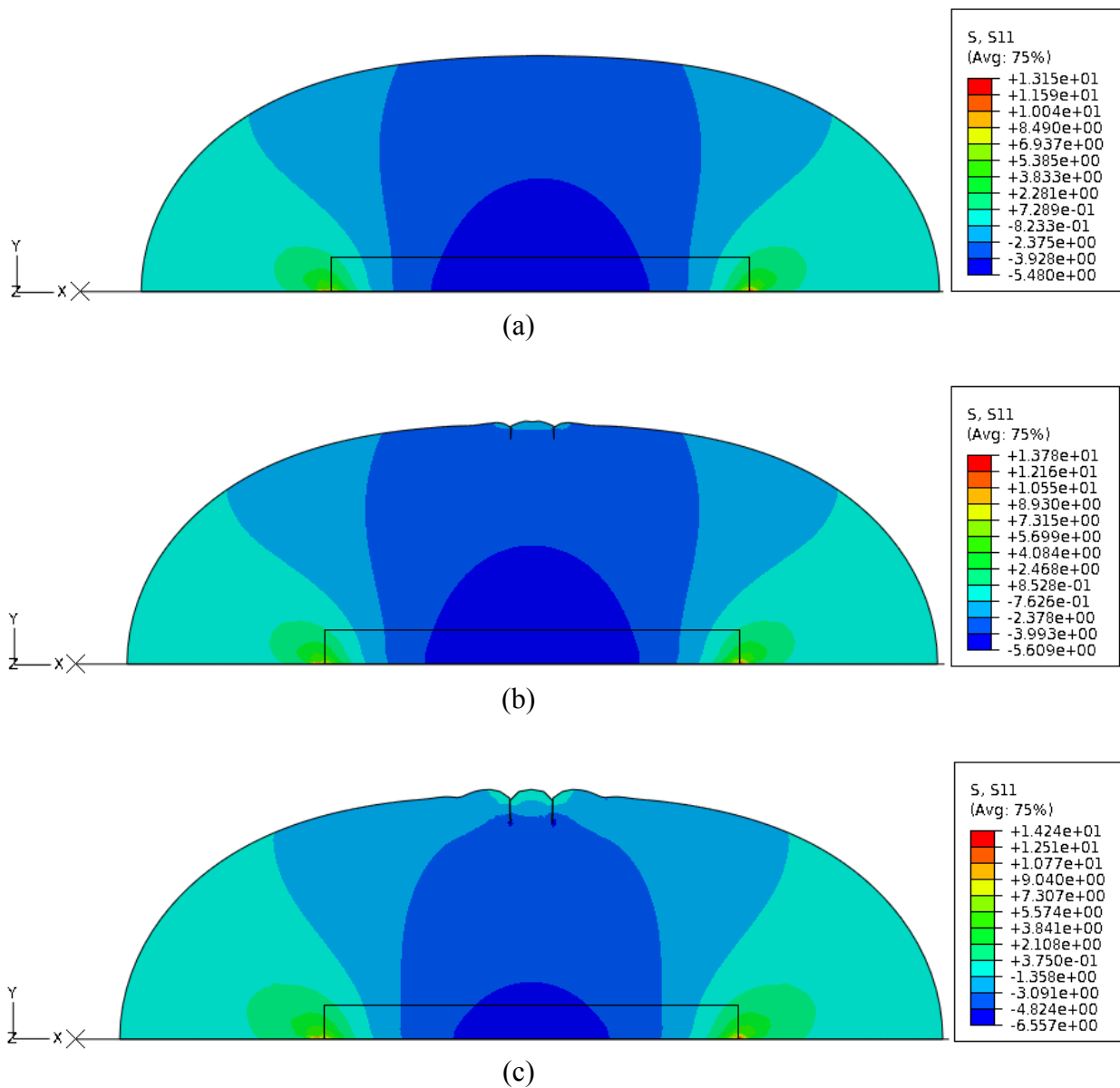


Figure 2.12: Formation of surface creases in a surface-attached hydrogel line with $W/H = 12$ as the chemical potential increases: (a) $\bar{\mu} = -0.00075$, (b) $\bar{\mu} = -0.0003$, and (c) $\bar{\mu} = 0$.

the critical condition for surface instability in a laterally constrained hydrogel film ($W/H \rightarrow \infty$) may be expressed in terms of the same parameters: if $f(\bar{\mu}, N\nu, \chi) < \infty$, the film surface is unstable; otherwise, the film surface is stable.

2.6. SUMMARY

This chapter formulates a general variational approach for equilibrium analysis of swelling deformation of hydrogels. The governing equations for mechanical and chemical equilibrium are obtained along with the boundary conditions. A specific material model is adopted based on a free energy density function. A finite element method for numerical analysis is developed, which allows anisotropic initial states for the study of swelling of hydrogels under constraints. Numerical results by the finite element method are compared to analytical solutions for homogeneous swelling of hydrogels, both without and with constraint. The close agreement between the two demonstrates the validity of the present approach. Inhomogeneous swelling of hydrogel lines attached to a rigid substrate is simulated, illustrating the effect of geometric constraint for different width-to-height aspect ratios. Of particular interest is the formation of surface creases in hydrogel lines beyond a critical aspect ratio. To further understand this phenomenon, the next chapter presents a theoretical analysis of swell-induced surface instability of hydrogels.

Chapter 3

Swell-induced surface instability of confined hydrogel layers

Swell-induced surface instability of hydrogels has been observed in many experiments [26, 75-76, 81] as well as in numerical simulations in the previous chapter. In this chapter, a linear perturbation analysis is performed to predict the critical condition for the onset of surface instability. Numerical simulations are presented to show the swelling process, with evolution of initial surface perturbations followed by formation of crease-like surface patterns

3.1. HOMOGENEOUS SWELLING OF A CONFINED HYDROGEL LAYER

Consider a hydrogel layer attached to a rigid substrate with the initial thickness h_0 (Fig. 3.1 (a)). Due to the confinement of the substrate, the hydrogel layer swells only in the thickness direction. The homogeneous solution for this case is given in Section 2.3.4. Here, an alternative approach is presented by an energy method.

Let 1 and 3 denote the in-plane directions and 2 the out-of-plane (thickness) direction. For homogeneous swelling, the deformation gradient tensor is diagonal, with the principal stretches, $F_{22} = \lambda_h$ and $F_{11} = F_{33} = 1$. The volume swelling ratio is simply, $J_h = \lambda_h$, and the nominal concentration of solvent molecule in the hydrogel is

$$C_h = \frac{\lambda_h - 1}{\nu}. \quad (3.1)$$

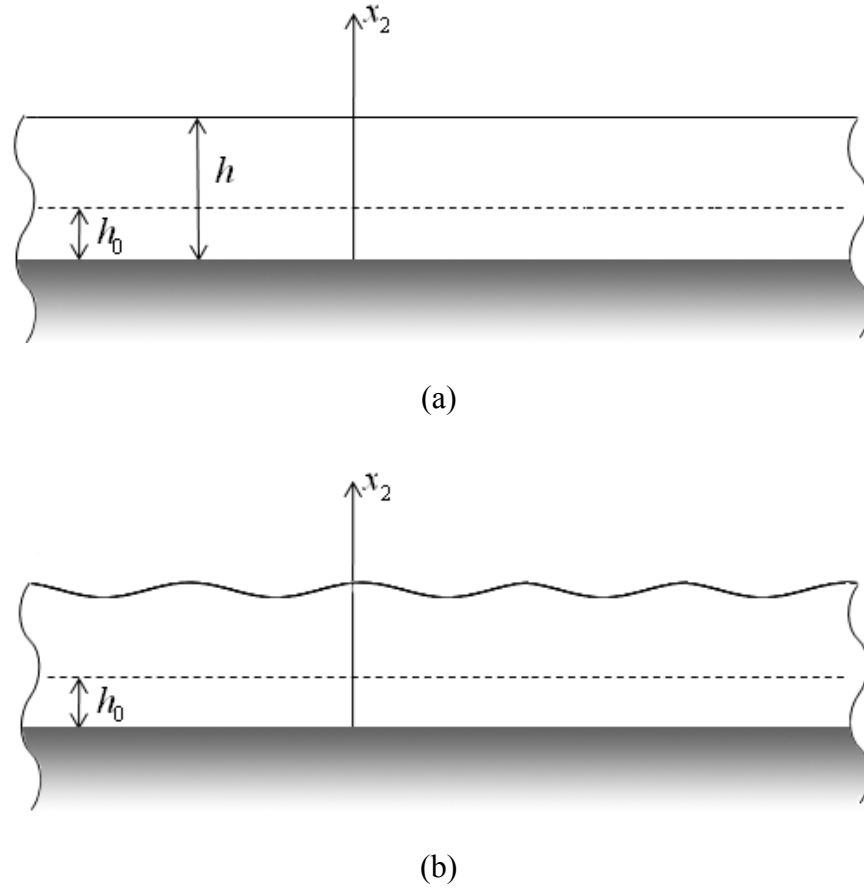


Figure 3.1: Schematic illustrations for (a) homogeneous swelling of a hydrogel layer, and (b) a perturbation of the swollen hydrogel layer.

Upon swelling, the free energy density inside the hydrogel becomes

$$U_h(\lambda_h) = U_e(\lambda_h) + U_m(C_h), \quad (3.2)$$

where, by Eqs. (2.29) and (2.32),

$$U_e(\lambda_h) = \frac{1}{2} N k_B T [\lambda_h^2 - 1 - 2 \ln(\lambda_h)], \quad (3.3)$$

$$U_m(C_h) = \frac{k_B T}{v} \left[(\lambda_h - 1) \ln \left(1 - \frac{1}{\lambda_h} \right) + \chi \left(1 - \frac{1}{\lambda_h} \right) \right]. \quad (3.4)$$

The total free energy of the system (including the hydrogel and the external solvent) consists of the internal free energy and the chemical/mechanical work done during absorption and swelling, namely

$$G = U_h V_0 - \hat{\mu} C_h V_0 + (J_h - 1) p V_0 = \left[U_h(\lambda_h) - \frac{\hat{\mu} - p v}{v} (\lambda_h - 1) \right] V_0, \quad (3.5)$$

where V_0 is the reference volume of the layer at the dry state. Note that the external solvent exerts a pressure p onto the surface of the hydrogel layer, which does negative work and thus increases the free energy as the hydrogel swells.

The equilibrium swelling ratio of the hydrogel can then be determined by minimizing the total free energy. Setting $dG/d\lambda_h = 0$ leads to

$$\ln \left(1 - \frac{1}{\lambda_h} \right) + \frac{1}{\lambda_h} + \frac{\chi}{\lambda_h^2} + N v \left(\lambda_h - \frac{1}{\lambda_h} \right) = \frac{\hat{\mu} - p v}{k_B T}. \quad (3.6)$$

This equation, after substituting the chemical potential in Eq. (2.24), is identical with Eqs. (2.46) and (2.47).

The lateral confinement by the substrate induces a compressive stress in the swollen hydrogel layer. By Eqs. (2.59) - (2.62), we obtain that

$$s_{ij} = N k_B T (F_{ij} - \lambda_h H_{ij}) - p H_{ij}, \quad (3.7)$$

where

$$H_{ij} = \frac{\partial J}{\partial F_{ij}} = \frac{1}{2} e_{ijk} e_{jkl} F_{jk} F_{kl}. \quad (3.8)$$

It then follows that

$$s_{11} = s_{33} = s_h = -Nk_B T(\lambda_h^2 - 1) - p\lambda_h, \quad (3.9)$$

and $s_{22} = -p$, while all other stress components are zero.

The true (Cauchy) stresses in the current state are related to the nominal stresses as

$$\sigma_{11} = \sigma_{33} = s_h / \lambda_h = -Nk_B T(\lambda_h - 1/\lambda_h) - p \quad \text{and} \quad \sigma_{22} = s_{22} = -p. \quad (3.10)$$

The hydrostatic pressure inside the hydrogel layer is thus

$$p_{in} = -\frac{1}{3}(\sigma_{11} + \sigma_{22} + \sigma_{33}) = \frac{2}{3}Nk_B T\left(\lambda_h - \frac{1}{\lambda_h}\right) + p. \quad (3.11)$$

The difference between the internal pressure of the gel and the external pressure of the solvent defines an osmotic pressure, namely

$$p_{os} = p_{in} - p = \frac{2}{3}Nk_B T\left(\lambda_h - \frac{1}{\lambda_h}\right). \quad (3.12)$$

3.2. LINEAR PERTURBATION ANALYSIS

To examine stability of the homogeneous swelling deformation of the confined hydrogel layer, we assume a small perturbation with displacements from the swollen state in both the thickness and lateral directions (Fig. 3.1 (b)), namely

$$u_1 = u_1(x_1, x_2) \quad \text{and} \quad u_2 = u_2(x_1, x_2). \quad (3.13)$$

In the spirit of linear perturbation analysis similar to that by Biot [84], along with the transverse isotropy of the homogeneous solution, the two-dimensional perturbation is sufficient to represent an arbitrary perturbation in three dimensions.

The deformation gradient after the perturbation becomes

$$\tilde{\mathbf{F}} = \begin{bmatrix} 1 + \frac{\partial u_1}{\partial x_1} & \lambda_h \frac{\partial u_1}{\partial x_2} & 0 \\ \frac{\partial u_2}{\partial x_1} & \lambda_h \left(1 + \frac{\partial u_2}{\partial x_2} \right) & 0 \\ 0 & 0 & 1 \end{bmatrix}. \quad (3.14)$$

Thus, the volume ratio of swelling (relative to the dry state) is

$$J = \det(\tilde{\mathbf{F}}) \approx \lambda_h \left(1 + \frac{\partial u_1}{\partial x_1} + \frac{\partial u_2}{\partial x_2} \right) = \lambda_h (1 + \varepsilon), \quad (3.15)$$

where $\varepsilon = \frac{\partial u_1}{\partial x_1} + \frac{\partial u_2}{\partial x_2}$ is the linear volumetric strain relative to the homogeneously

swollen state, and only the first-order terms of the perturbation are retained for the linear analysis. As a result, the concentration field in the hydrogel becomes inhomogeneous, namely

$$\nu C = J - 1 \approx \nu C_h + \lambda_h \varepsilon. \quad (3.16)$$

By substituting Eq. (3.14) into Eq. (3.7), we obtain the nominal stresses after the perturbation,

$$s_{ij} \approx Nk_B T \left[\tilde{F}_{ij} - (\lambda_h - \xi_h \varepsilon) \tilde{H}_{ij} \right] - p \tilde{H}_{ij}, \quad (3.17)$$

where

$$\xi_h = \frac{1}{\lambda_h} + \frac{1}{N\nu} \left(\frac{1}{\lambda_h - 1} - \frac{1}{\lambda_h} - \frac{2\chi}{\lambda_h^2} \right). \quad (3.18)$$

Expanding Eq. (3.17) gives the stress components explicitly as follows:

$$s_{11} \approx s_h + Nk_B T \left[(1 + \lambda_h \xi_h) \frac{\partial u_1}{\partial x_1} + \lambda_h (\xi_h - \lambda_h) \frac{\partial u_2}{\partial x_2} \right] - p \lambda_h \frac{\partial u_2}{\partial x_2}, \quad (3.19)$$

$$s_{22} \approx -p + Nk_B T \left[(\xi_h - \lambda_h) \frac{\partial u_1}{\partial x_1} + (\xi_h + \lambda_h) \frac{\partial u_2}{\partial x_2} \right] - p \frac{\partial u_1}{\partial x_1}, \quad (3.20)$$

$$s_{33} \approx s_h + Nk_B T \lambda_h (\xi_h - \lambda_h) \varepsilon - p \lambda_h \varepsilon, \quad (3.21)$$

$$s_{12} \approx Nk_B T \lambda_h \left(\frac{\partial u_1}{\partial x_2} + \frac{\partial u_2}{\partial x_1} \right) + p \frac{\partial u_2}{\partial x_1}, \quad (3.22)$$

$$s_{21} \approx Nk_B T \left(\lambda_h^2 \frac{\partial u_1}{\partial x_2} + \frac{\partial u_2}{\partial x_1} \right) + p \lambda_h \frac{\partial u_1}{\partial x_2}, \quad (3.23)$$

and $s_{23} = s_{32} = s_{13} = s_{31} = 0$. Apparently, the linearized stress-strain relationship for the hydrogel layer becomes anisotropic due to the anisotropic swelling deformation before perturbation.

By substituting the stress components into the equilibrium equations Eq. (2.19)

and setting the body force $B_i = 0$, we obtain that

$$(1 + \lambda_h \xi_h) \frac{\partial^2 u_1}{\partial x_1^2} + \lambda_h^2 \frac{\partial^2 u_1}{\partial x_2^2} + \lambda_h \xi_h \frac{\partial^2 u_2}{\partial x_1 \partial x_2} = 0, \quad (3.24)$$

$$\frac{\partial^2 u_2}{\partial x_1^2} + \lambda_h (\xi_h + \lambda_h) \frac{\partial^2 u_2}{\partial x_2^2} + \lambda_h \xi_h \frac{\partial^2 u_1}{\partial x_1 \partial x_2} = 0. \quad (3.25)$$

Applying Fourier transform with respect to x_1 in Eq. (3.24) and (3.25), we obtain that

$$-k^2 (1 + \lambda_h \xi_h) \hat{u}_1 + \lambda_h^2 \frac{d^2 \hat{u}_1}{dx_2^2} + ik \lambda_h \xi_h \frac{d\hat{u}_2}{dx_2} = 0, \quad (3.26)$$

$$-k^2 \hat{u}_2 + \lambda_h (\xi_h + \lambda_h) \frac{d^2 \hat{u}_2}{dx_2^2} + ik \lambda_h \xi_h \frac{d\hat{u}_1}{dx_2} = 0, \quad (3.27)$$

where $i = \sqrt{-1}$, $\hat{u}_1(x_2; k)$ and $\hat{u}_2(x_2; k)$ are the Fourier transforms of $u_1(x_1, x_2)$ and $u_2(x_1, x_2)$ with the wave number k in the x_1 direction.

The general solution to Eqs. (3.26) and (3.27) takes the form

$$\hat{u}_1 = \bar{u}_1 \exp(qx_2) \quad \text{and} \quad \hat{u}_2 = \bar{u}_2 \exp(qx_2). \quad (3.28)$$

Substitution of Eq. (3.28) into Eqs. (3.26) and (3.27) leads to an eigenvalue problem

$$\left[-k^2(1 + \lambda_h \xi_h) + \lambda_h^2 q^2 \right] \bar{u}_1 + ik\lambda_h \xi_h q \bar{u}_2 = 0, \quad (3.29)$$

$$ik\lambda_h \xi_h q \bar{u}_1 + \left[-k^2 + \lambda_h (\xi_h + \lambda_h) q^2 \right] \bar{u}_2 = 0, \quad (3.30)$$

for which the eigenvalues are solved from the characteristic equation

$$\begin{vmatrix} -k^2(1 + \lambda_h \xi_h) + \lambda_h^2 q^2 & ik\lambda_h \xi_h q \\ ik\lambda_h \xi_h q & -k^2 + \lambda_h (\xi_h + \lambda_h) q^2 \end{vmatrix} = 0, \quad (3.31)$$

or equivalently,

$$(\lambda_h + \xi_h) \lambda_h^3 q^4 - (\xi_h + 2\lambda_h + \lambda_h^2 \xi_h) \lambda_h k^2 q^2 + (1 + \lambda_h \xi_h) k^4 = 0. \quad (3.32)$$

Solving Eq. (3.32), we obtain four eigenvalues

$$q_{1,2} = \pm \frac{k}{\lambda_h} \quad \text{and} \quad q_{3,4} = \pm k\beta, \quad (3.33)$$

where $\beta = \sqrt{\frac{1 + \lambda_h \xi_h}{\lambda_h^2 + \lambda_h \xi_h}}$. There exist two sets of degenerated solutions to the eigenvalue

problem, when $\xi_h = 0$ or $\lambda_h \xi_h = -1$, as given in Appendix B. They have no substantial effect on the stability analysis that follows.

For each eigenvalue, q_n ($n = 1 - 4$), an eigenvector, $(\bar{u}_1^{(n)}, \bar{u}_2^{(n)})$, is obtained from Eqs. (3.29) and (3.30). Therefore, the complete solution to Eqs. (3.26) and (3.27) is

$$\hat{u}_1(x_2; k) = \sum_{n=1}^4 A_n \bar{u}_1^{(n)} \exp(q_n x_2), \quad (3.34)$$

$$\hat{u}_2(x_2; k) = \sum_{n=1}^4 A_n \bar{u}_2^{(n)} \exp(q_n x_2), \quad (3.35)$$

where, except for the degenerated cases,

$$\begin{bmatrix} \bar{u}_1^{(1)} & \bar{u}_1^{(2)} & \bar{u}_1^{(3)} & \bar{u}_1^{(4)} \\ \bar{u}_2^{(1)} & \bar{u}_2^{(2)} & \bar{u}_2^{(3)} & \bar{u}_2^{(4)} \end{bmatrix} = \begin{bmatrix} 1 & 1 & 1 & 1 \\ -i\lambda_n & i\lambda_n & -i\beta & i\beta \end{bmatrix}. \quad (3.36)$$

The perturbation displacement can then be obtained by inverse Fourier transform of Eqs. (3.34) and (3.35), which may be considered as a superposition of many Fourier components. For each Fourier component with a specific wave number k , the displacement is periodic in the x_1 direction, but varies exponentially in the x_2 direction for each eigen mode, similar to Biot's analysis for surface instability of a half-space rubber-like medium under compression [84], but in contrast with the sinusoidal variation assumed by Tanaka et al. [76].

For each wave number k , the amplitudes for the four eigen modes (A_n , $n = 1 - 4$) are obtained by applying the boundary conditions. The lower surface of the hydrogel layer is attached to the rigid substrate with zero displacement, i.e.,

$$u_1 = u_2 = 0 \quad \text{at } x_2 = 0. \quad (3.37)$$

The upper surface of the hydrogel is subjected to a normal traction due to the pressure of external solvent. To the first order of perturbation, the nominal magnitude of the traction at the perturbed state is

$$T \approx p \left(1 + \frac{\partial u_1}{\partial x_1} \right), \quad (3.38)$$

and the direction is perpendicular to the perturbed surface with the unit vector,

$$n_1 \approx \frac{\partial u_2}{\partial x_1} \quad \text{and} \quad n_2 \approx -1 + \frac{1}{2} \left(\frac{\partial u_2}{\partial x_1} \right)^2. \quad (3.39)$$

Therefore, by Eq. (2.23) and to the first order of perturbation, the traction boundary condition at the upper surface is

$$s_{12} = p \frac{\partial u_2}{\partial x_1} \quad \text{and} \quad s_{22} = -p \left(1 + \frac{\partial u_1}{\partial x_1} \right) \quad \text{at} \quad x_2 = h, \quad (3.40)$$

where $h = \lambda_h h_0$ is the thickness of the hydrogel layer at the swollen state (before perturbation) and h_0 is the dry-state thickness.

Substituting Eqs. (3.34) and (3.35) into Eqs. (3.20) and (3.22) and then applying the boundary conditions in Eqs. (3.37) and (3.40), we obtain that

$$\sum_n^4 A_n \bar{u}_1^{(n)} = 0, \quad (3.41)$$

$$\sum_n^4 A_n \bar{u}_2^{(n)} = 0, \quad (3.42)$$

$$\sum_{n=1}^4 \left[ik(\xi_h - \lambda_h) \bar{u}_1^{(n)} + (\xi_h + \lambda_h) q_n \bar{u}_2^{(n)} \right] A_n \exp(q_n h) = 0, \quad (3.43)$$

$$\sum_n^4 \left[\lambda_h q_n \bar{u}_1^{(n)} + ik \lambda_h \bar{u}_2^{(n)} \right] A_n \exp(q_n h) = 0. \quad (3.44)$$

Re-writing Eqs. (3.41)-(3.44) in a matrix form, we obtain that

$$\sum_{n=1}^4 D_{mn}(k)A_n = 0, \quad (3.45)$$

where the coefficient matrix is given by

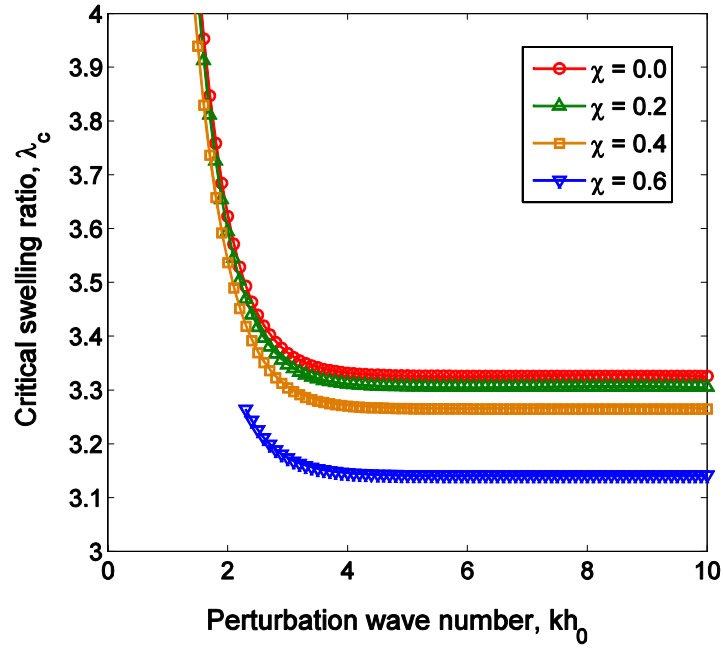
$$[D_{mn}] = \begin{bmatrix} 1 & 1 & 1 & 1 \\ -\lambda_h & \lambda_h & -\beta & \beta \\ 2\lambda_h e^{kh_0} & 2\lambda_h e^{-kh_0} & \left(\lambda_h + \frac{1}{\lambda_h}\right)e^{\beta kh} & \left(\lambda_h + \frac{1}{\lambda_h}\right)e^{-\beta kh} \\ \left(\lambda_h + \frac{1}{\lambda_h}\right)e^{kh_0} & -\left(\lambda_h + \frac{1}{\lambda_h}\right)e^{-kh_0} & 2\beta e^{\beta kh} & -2\beta e^{-\beta kh} \end{bmatrix} \quad (3.46)$$

The homogeneous swelling deformation of the hydrogel layer becomes unstable when Eq. (3.45) yields nontrivial solutions for the amplitudes, A_n ($n = 1 - 4$). The critical condition for the onset of instability is thus predicted by setting the determinant of the matrix \mathbf{D} to be zero, namely

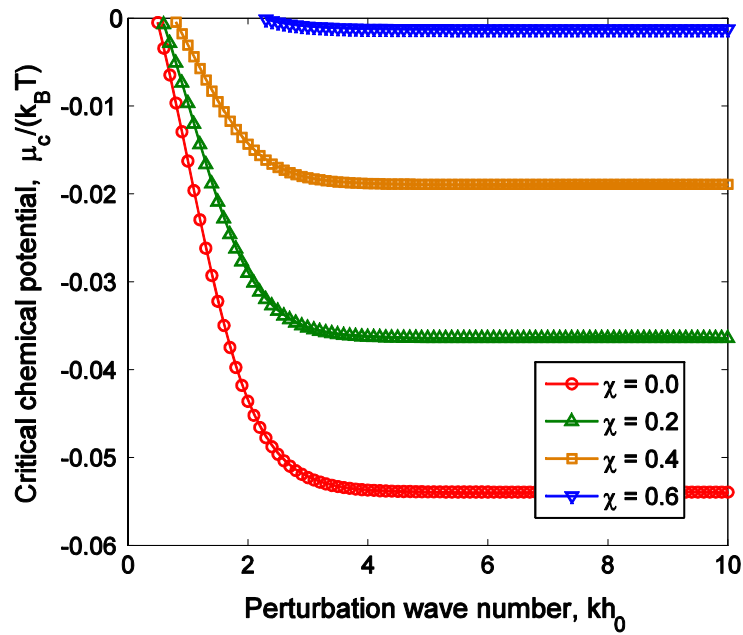
$$\det[D_{mn}] = f(kh_0, \lambda_h; N\nu, \chi) = 0. \quad (3.47)$$

For each kh_0 , Eq. (3.47) predicts a critical swelling ratio, $\lambda_c(kh_0; N\nu, \chi)$, which depends on the two material parameters ($N\nu$ and χ) of the hydrogel. The corresponding critical chemical potential (μ_c) can then be obtained from the homogeneous solution, Eq. (3.6).

Figure 3.2 (a) plots the predicted critical swelling ratio as a function of kh_0 , and Figure 3.2 (b) plots the critical chemical potential, for $\bar{p}_0 = 2.3 \times 10^{-5}$, $N\nu = 0.001$, and different values of χ . Unlike the critical compression for surface instability of a semi-infinite rubber, which is independent of the perturbation wavelength [84], the critical swelling ratio for swell-induced surface instability of a hydrogel layer depends on the normalized perturbation wave number, kh_0 , due to the presence of a rigid substrate. The



(a)



(b)

Figure 3.2: (a) Critical swelling ratio and (b) the corresponding chemical potential, predicted by the linear perturbation analysis, versus the perturbation wave number for $N\nu = 0.001$.

substrate confinement tends to stabilize long-wavelength perturbations (with small kh_0), while the confinement effect diminishes for short-wavelength perturbations (with large kh_0). Consequently, the critical swelling ratio decreases as kh_0 increases and approaches a constant at the limit of short-wavelength perturbations ($kh_0 \rightarrow \infty$). Therefore, the onset of surface instability is controlled by the minimum critical swelling ratio at the short-wavelength limit. It is speculated that surface effects (e.g., surface energy, surface stress) could potentially stabilize short-wavelength perturbations and, together with the substrate confinement effect, could lead to an intermediate wavelength for onset of the surface instability. This will be discussed in Chapter 5.

It is noted in Fig. 3.2 that, for $\chi \leq 0.6$, there exists a critical wave number, for which the critical swelling ratio equals the maximum homogeneous swelling ratio and the corresponding critical chemical potential equals zero. For smaller perturbation wave numbers, the hydrogel layer remains stable at the equilibrium chemical potential ($\mu = \hat{\mu} = 0$). For $\chi > 0.6$, however, we find that the hydrogel layer remains stable for all possible perturbation wave numbers; thus no critical condition is predicted. As shown later (Fig. 3.4), for each Nv , there exists a critical value for χ , beyond which the hydrogel layer is stable and swells homogeneously at the equilibrium state.

Next we focus our attention on the critical condition at the short-wavelength limit. By letting $kh_0 \rightarrow \infty$ in Eq. (3.46) and setting the determinant of the matrix to be zero, we obtain that

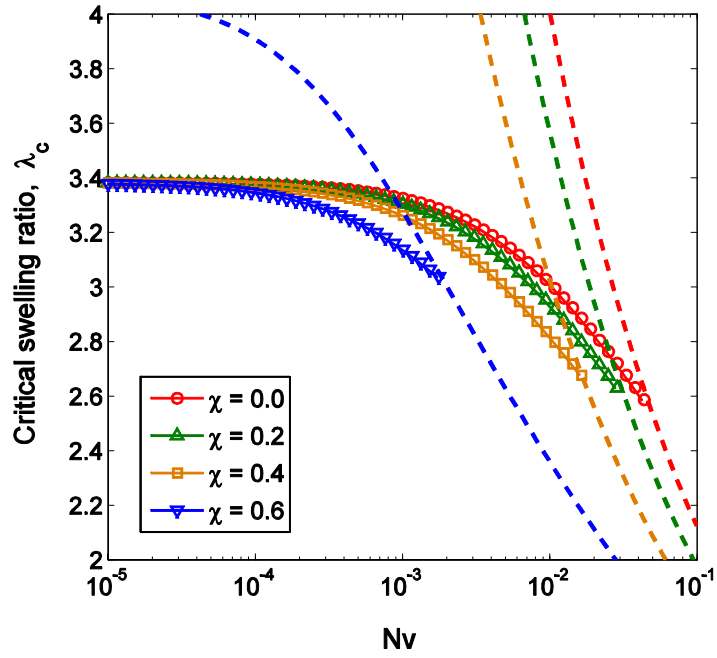
$$f_{\infty}(\lambda_h; N\nu, \chi) = \left[\left(\lambda_h + \frac{1}{\lambda_h} \right)^2 - 4\lambda_h\beta \right] (\beta - \lambda_h) = 0. \quad (3.48)$$

It can be shown that $\beta - \lambda_h \neq 0$ for all swelling hydrogels ($\lambda_h > 1$). Thus, the critical condition becomes

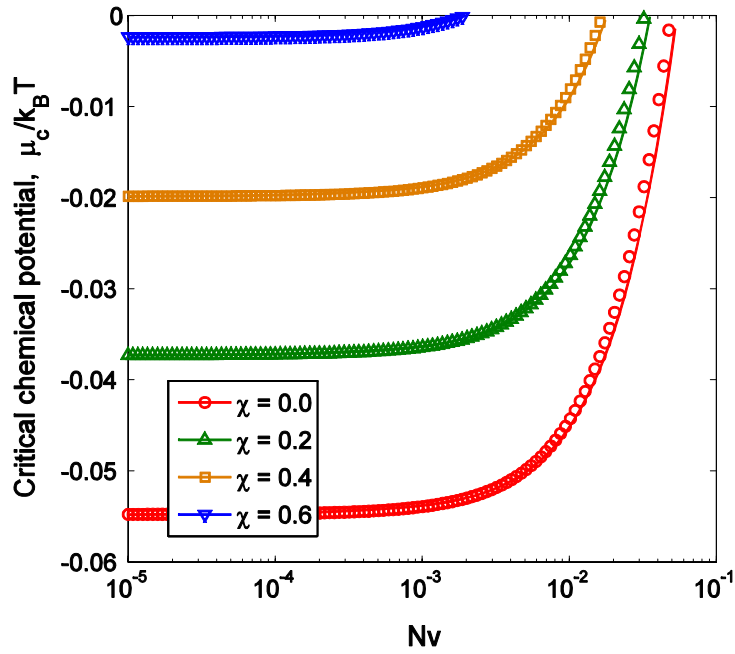
$$\left(\lambda_h + \frac{1}{\lambda_h} \right)^2 - 4\lambda_h\beta = 0. \quad (3.49)$$

Combining this with the definitions of β in Eq. (3.33) and ξ_h in Eq. (3.18) gives a nonlinear equation, which can be solved to predict the critical swelling ratio at the short-wavelength limit, $\lambda_c^{\infty}(N\nu, \chi)$. The corresponding critical chemical potential, $\mu_c^{\infty}(N\nu, \chi, \bar{p}_0)$, is calculated from Eq. (3.6) by setting $\lambda_h = \lambda_c^{\infty}(N\nu, \chi)$.

Figure 3.3 (a) plots the predicted critical swelling ratio (λ_c^{∞}) as a function of $N\nu$ for different values of χ , and Fig. 3.3 (b) plots the critical chemical potential (μ_c^{∞}), assuming a constant equilibrium vapor pressure ($\bar{p}_0 = 2.3 \times 10^{-5}$). The dashed lines in Fig. 3.3 (a) show the maximum homogeneous swelling ratio predicted by Eq. (3.6). For each χ , the critical chemical potential increases monotonically with increasing $N\nu$ until it reaches the equilibrium chemical potential ($\mu_c^{\infty} = 0$), at which point the critical swelling ratio equals the maximum homogeneous swell ratio. Therefore, the stability of the homogeneously swollen hydrogel layer depends on both $N\nu$ and χ . The two dimensionless material parameters characterize the elastic stiffness of the polymer network and the polymer-solvent interaction, respectively. While the polymer stiffness



(a)



(b)

Figure 3.3: (a) Critical swelling ratio and (b) critical chemical potential, predicted by the linear perturbation analysis at an infinite wave number (short-wavelength limit), versus Nv for different values of χ .

increases with $N\nu$, the network tends to swell more significantly in a good solvent (low χ) than in a poor solvent (high χ). The interplay between the two parameters is summarized in a diagram (Fig. 3.4) that separates the region of unstable hydrogels from that of stable hydrogels. The boundary line between the two regions is determined by setting $\bar{\mu}_c^\infty = 0$ or $\lambda_c^\infty(N\nu, \chi) = \max(\lambda_h)$ in Eq. (3.49). The range of $N\nu$ in Fig. 3.4 roughly corresponds to a range between 1 kPa and 10 MPa for the initial shear modulus ($Nk_B T$) of the polymer network at 25°C, which is typical for hydrogels and elastomers. For a hydrogel layer with properties in the upper-right region of the diagram (stiff network, poor solvent), it swells

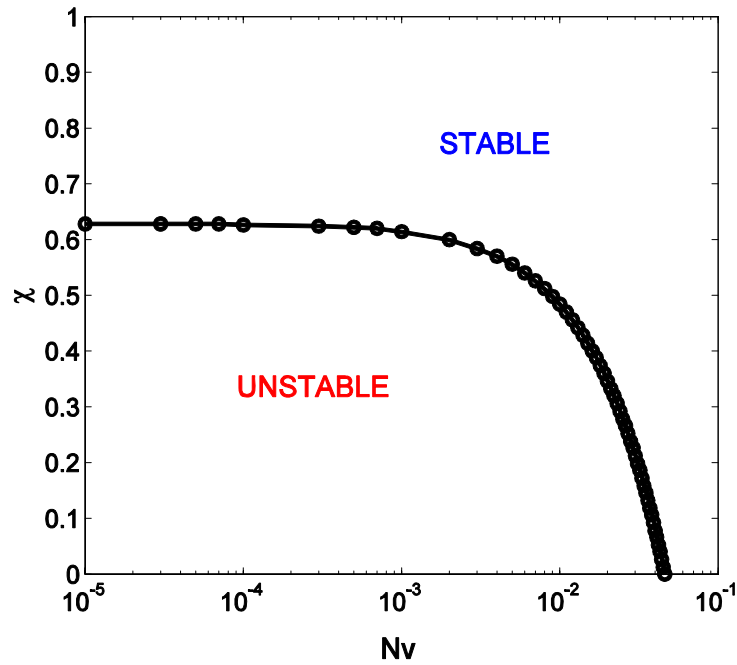


Figure 3.4: A stability diagram for substrate-confined hydrogel layers.

homogeneously and remains stable at the equilibrium chemical potential ($\mu = 0$). The homogeneous swelling ratio is typically small ($\lambda_h < 3$) in this region. For a hydrogel layer with properties in the lower-left region (soft network, good solvent), swell-induced surface instability occurs at a critical swelling ratio (Fig. 3.3 (a)) before it reaches the maximum homogeneous swelling ratio. The predicted critical swelling ratio, ranging between 2.5 and 3.4, depends on both $N\nu$ and χ .

It is noted that, when $N\nu$ is relatively small ($< 10^{-4}$), the critical swelling ratio (Fig. 3.3 (a)) is nearly a constant (~ 3.4) independent of $N\nu$ or χ , and the critical value of χ that separates the unstable and stable regions in Fig. 3.4 is nearly independent of $N\nu$. On the other hand, the critical chemical potential (Fig. 3.3 (b)), nearly independent of $N\nu$, increases with increasing χ . These results may be understood intuitively by considering the limiting case when the contribution of elasticity is negligible ($N\nu \rightarrow 0$) for both the homogeneous swelling and the stability analysis. In this case, the competition between the entropy of mixing and the enthalpy of solvent-polymer interaction dominates the swelling process. Consequently, the stability of the hydrogel layer depends on χ only. As $N\nu \rightarrow 0$, $\xi_h \rightarrow \infty$ and $\beta \rightarrow 1$. Solving Eq. (3.49) gives a nontrivial solution for the constant critical swelling ratio, $\lambda_c = 3.38$. By Eq. (3.6), the critical chemical potential is approximately

$$\frac{\mu_c}{k_B T} \approx 0.0875\chi - 0.0549. \quad (3.50)$$

Setting $\mu_c = 0$ in Eq. (3.50), we obtain that $\lambda_c = 0.63$. This critical value of λ is slightly higher than the critical value that was used to define a good solvent ($\lambda < 0.5$) for swelling polymer networks [6].

Previously, Tanaka et al. [76] suggested a critical osmotic pressure above which distinct surface instability patterns appear in swelling gel slabs. As defined in Eq. (3.12), the osmotic pressure can be determined from the homogeneous swelling ratio. However, their theoretical analysis assumed inhomogeneous swelling of the gel slab even before the onset of instability and the predicted critical pressure depends on variation of the elastic modulus in the swollen state, which cannot readily be evaluated for quantitative comparisons. It has also been suggested that the compressive stress developed in the swollen hydrogel is the driving force for surface instability of confined hydrogel layers [81]. Based on the homogeneous solution in Section 3.1, the critical compressive stress is obtained as

$$\sigma_c = Nk_B T \left(\lambda_c - \frac{1}{\lambda_c} \right) + p_0 \exp\left(\frac{\mu_c}{k_B T} \right). \quad (3.51)$$

Using the critical swelling ratio and the critical chemical potential in Fig. 3.3, we plot the critical compressive stress as a function of $N\nu$ in Fig. 3.5 (a). For comparison, the dashed lines show the compressive stress at the maximum homogeneous swelling ratio. Again, the critical compressive stress in general depends on both $N\nu$ and λ . When $N\nu < 10^{-4}$, we have approximately,

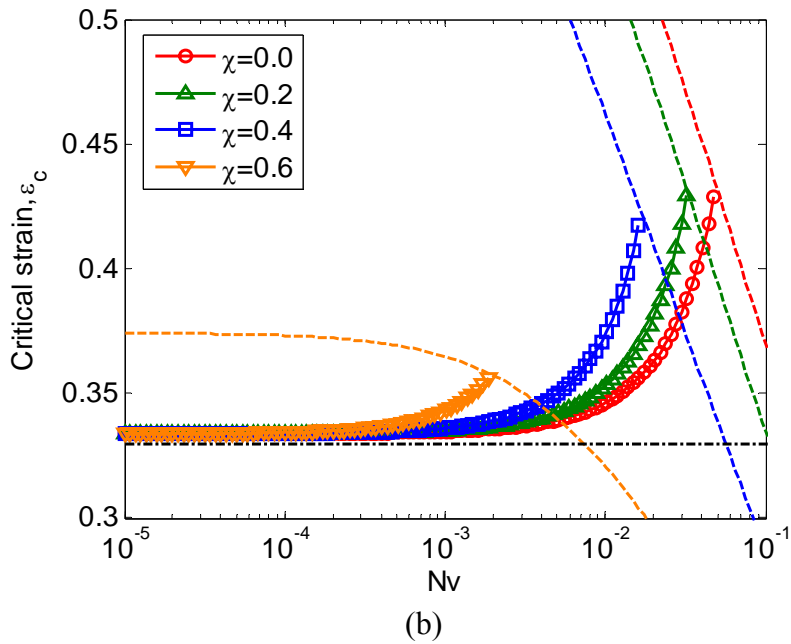
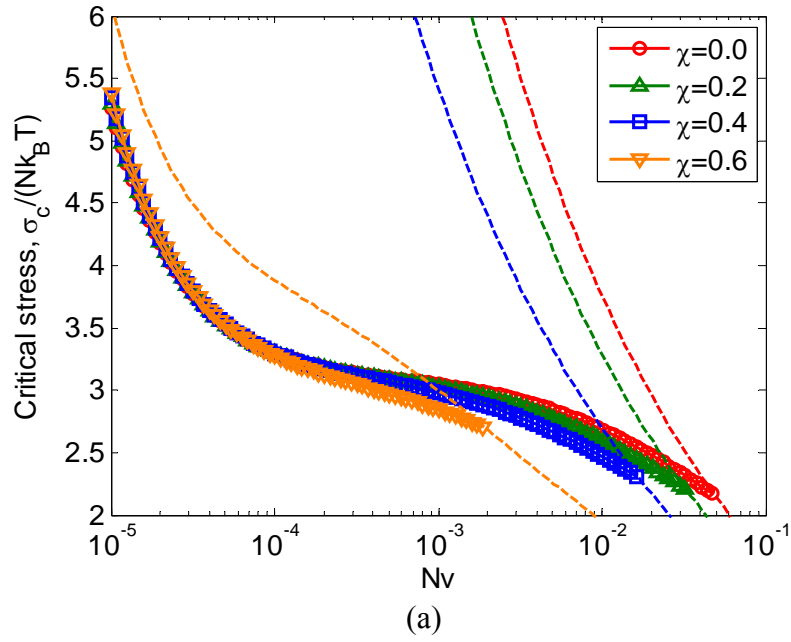


Figure 3.5: (a) Critical compressive stress and (b) critical linear strain, versus Nv for different values of χ . The dashed lines in (b) show the effective strain for homogeneous swelling at $\mu = 0$. The horizontal dash-dotted lines in (a) and (b) indicate the critical stress ($3.08Nk_B T$) and the critical strain (0.33) for a semi-infinite rubber, respectively.

$$\sigma_c \approx Nk_B T \left[3.1 + \frac{\bar{p}_0}{N\nu} \exp(0.0875\chi - 0.0549) \right], \quad (3.52)$$

which weakly depends on χ . Interestingly, the first term in the bracket of Eq. (3.52) compares closely with Biot's prediction of the critical stress ($\sigma_c = 3.08Nk_B T$) for an incompressible rubber-like half-space under plane-strain compression [84]. The second term in the bracket is usually small compared with the first term. But as $N\nu$ gets smaller, the effect of the second term becomes significant and it gives the rise for smaller $N\nu$ in Fig. 3.5 (a).

Based on their experiments with a model system of poly(acrylamide-co-sodium acrylate) hydrogels, Trujillo et al. [81] found that the onset of surface creasing instability corresponds to an effective linear compressive strain of ~ 0.33 , in close agreement with Biot's prediction for a rubber-like half-space under equi-biaxial compression. We calculate the effective linear strain by comparing the laterally confined hydrogel layer to un-constrained free swelling of the same hydrogel system. The linear swelling ratio for free swelling can be obtained as a function of the chemical potential from Eqs. (2.45) and (2.46). The effective linear strain from the state of free swelling to that of the laterally confined swelling is then

$$\varepsilon = \frac{\lambda_0 - 1}{\lambda_0}. \quad (3.53)$$

Figure 3.5 (b) plots the effective linear strain corresponding to the critical chemical potential in Fig. 3.3 (b), where the dashed lines show the maximum strain at $\mu = 0$. While the maximum strain decreases monotonically with increasing $N\nu$, the critical

strain for swell-induced surface instability ($\mu_c < 0$) increases with $N\nu$, due to increasing critical chemical potential. Remarkably, the predicted critical strain is very close to 0.33 for hydrogel systems with $N\nu < 10^{-4}$. By using the approximate solution for the critical chemical potential in Eq. (3.50), we obtain approximately, $\lambda_0 \approx 0.0875^{-1/6} = 1.5$, and thus $\varepsilon \approx 0.33$.

Among various critical quantities shown in Figs. 3.3 and 3.5, the critical swelling ratio can be directly measured experimentally. As noticed previously [86], the wide range of the reported critical swelling ratios (from 2 to 3.72) has not been well understood. While the present study predicts a range of critical swelling ratios (from 2.5 to 3.4), in reasonable agreement with the reported values, quantitative comparisons for specific hydrogel systems are not possible at the moment, because the two key parameters ($N\nu$ and χ) that determine the critical swelling ratio in the present model are not readily available from the reported experiments. In principle, both $N\nu$ and χ can be measured by independent experiments. For example, $N\nu$ is related to the initial shear modulus of the polymer network ($Nk_B T$), which in turn can be related to the crosslink density and molecular weight [38]. The interaction parameter χ can be determined by measuring the volume ratio of free swelling [105]. It was also suggested that χ is inversely proportional to the temperature [6]. Consequently, the stability of the confined hydrogel layer may depend on temperature.

It needs to be pointed out that the present analysis of surface instability assumes a quasi-statically controlled swelling process, where the chemical potential is ramped up

slowly as a loading parameter and the hydrogel swells to an equilibrium state at each loading step until the onset of surface instability. The same process will be simulated numerically using a nonlinear finite element method in the next section. However, in many experiments [76, 81], as a hydrogel is immersed in a solvent of a constant chemical potential (like a step loading), swelling is a kinetic process with non-equilibrium transient states. The kinetics of molecular transport coupled with large deformation of the polymer network could lead to a rich dynamics of evolving surface instability patterns, which presents an interesting topic for future studies.

3.3. NUMERICAL SIMULATIONS

In this section, we use a nonlinear finite element method developed in Chapter 2 to numerically simulate swelling of a confined hydrogel layer and surface evolution beyond the critical point predicted by the linear perturbation analysis. The hydrogel layer is modeled with two-dimensional plane-strain elements (CPE4) in the commercial package ABAQUS [100], along with a self-developed user subroutine (UMAT) for the constitutive behavior of hydrogels. The lower surface of the hydrogel layer is fixed, while the upper surface is subjected to a pressure that depends on the chemical potential according to Eq. (2.24). Symmetric boundary conditions are imposed at the two vertical sidewalls of the model so that the layer can swell only in the thickness direction. The chemical potential in the hydrogel is ramped up as a loading parameter, and the equilibrium equations of the system are solved at each step by a nonlinear solver based on the Newton-Raphson method. As stated before, to circumvent the numerical difficulty

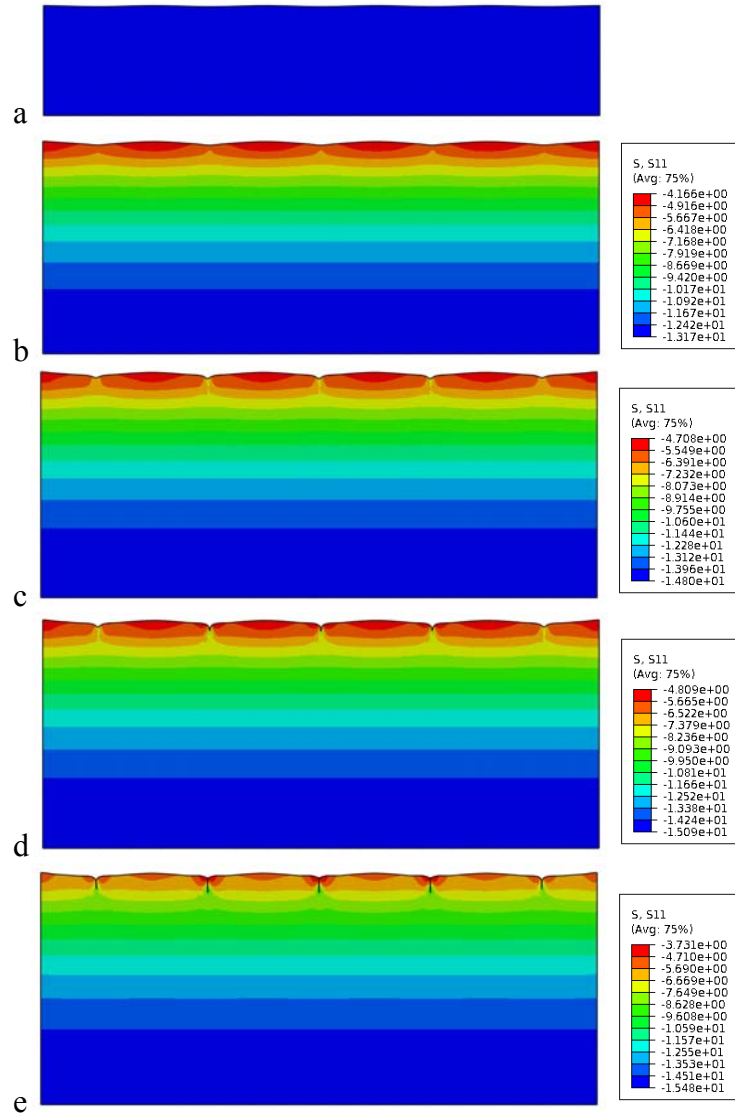


Figure 3.6: Numerical simulation of swell-induced surface instability of a substrate-confined hydrogel layer ($N\nu = 0.001$ and $\chi = 0.4$). Contours show distribution of the compressive true stress in the lateral direction (σ_{11}). (a) Initial perturbation at $\bar{\mu} = -0.0916$; (b) $\bar{\mu} = -0.00456$; (c) $\bar{\mu} = -0.00126$; (d) $\bar{\mu} = -0.000713$; and (e) $\bar{\mu} = 0$. The stress magnitude in the scale bar is normalized by the initial shear modulus of the polymer network ($Nk_B T$).

with the negative infinite chemical potential in the dry state, we start each numerical simulation with an initial state of homogeneous swelling, for which the chemical potential can be determined analytically by Eq. (3.6) for a specific hydrogel system. A small perturbation is then introduced as surface imperfection, which is generated using cubic spline curves in ABAQUS.

Figure 3.6 (a-e) shows the snapshots from one simulation, for a hydrogel layer with $Nv = 0.001$ and $\chi = 0.4$. Figure 3.6 (a) shows the initial state of homogeneous swelling ($\lambda_h = 2$ and $\bar{\mu} = -0.0916$) with a small surface perturbation. At $\bar{\mu} = -0.00456$ (Fig. 3.6 (b)), the hydrogel layer has swollen nearly twice its former size while the surface perturbation has grown considerably, resulting in a clearly inhomogeneous distribution of the compressive stress (σ_{11}) in the layer. As the chemical potential continues to rise, the surface perturbation evolves to form localized grooves (Fig. 3.6 (c)), and eventually the two sides of the groove fold into each other, forming surface creases (Fig. 3.6 (d) and (e)). A frictionless, hard self-contact is defined for the surface to prevent penetration. The simulation is stopped at $\bar{\mu} = 0$. The evolution of the hydrogel surface is shown more clearly in Fig. 3.7 (a-e), where a self-similar growth of the initial perturbation is followed by formation of surface grooves and creases. It is thus suggested that the onset of swell-induced surface instability in a confined hydrogel layer as predicted by the linear perturbation analysis in Section 3.2 could grow into surface creases as a result of the nonlinear post-instability effect. As an analogy, formation of surface grooves has been shown in simulations for surface evolution of stressed crystals facilitated by surface diffusion [106-107], as a nonlinear phenomenon following the

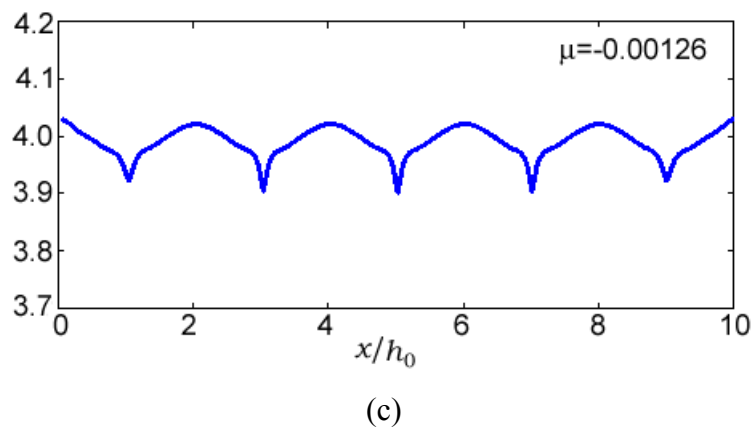
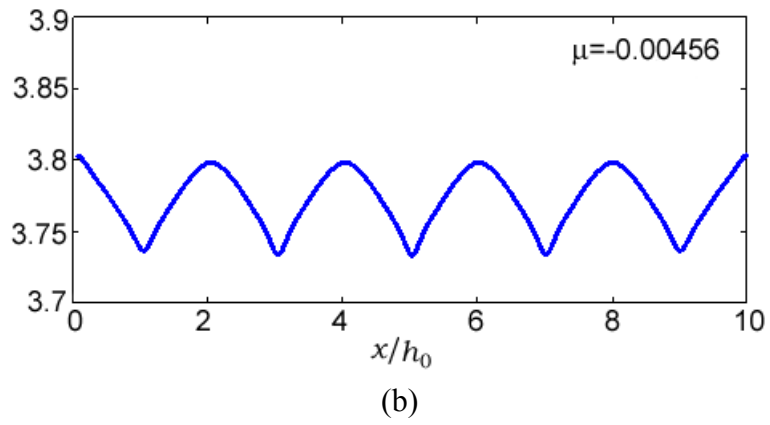
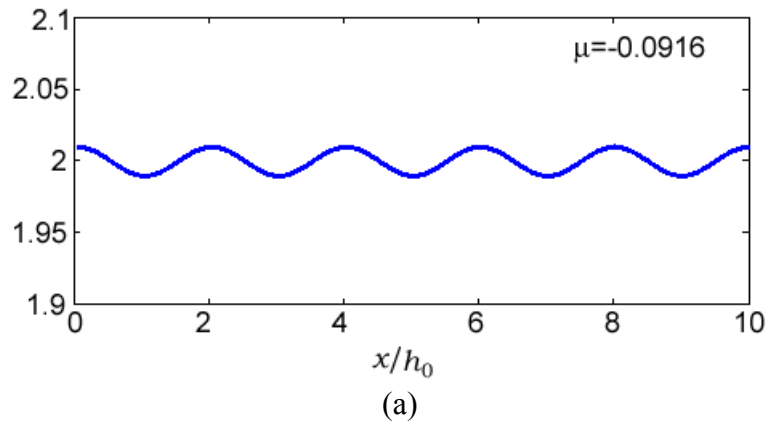


Figure 3.7: Evolution of the surface profile of a substrate-confined hydrogel layer ($Nv = 0.001$ and $\chi = 0.4$). (a) Initial perturbation at $\bar{\mu} = -0.0916$; (b) $\bar{\mu} = -0.00456$; (c) $\bar{\mu} = -0.00126$; (d) $\bar{\mu} = -0.000713$; and (e) $\bar{\mu} = 0$.

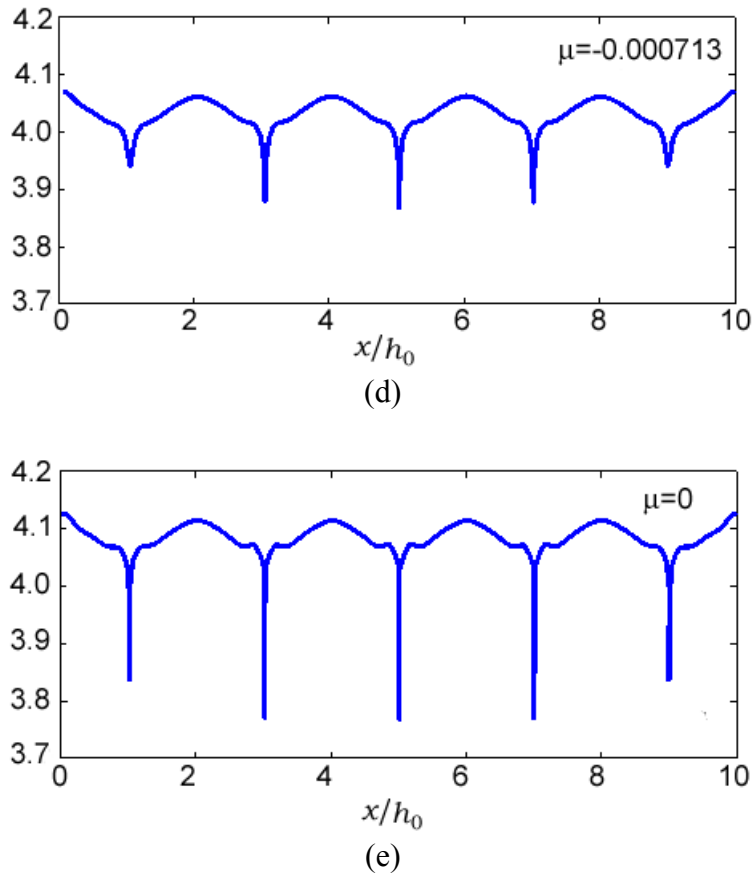


Figure 3.7: Continued.

growth of initially linear perturbations.

3.4. SUMMARY

This chapter presents a linear perturbation analysis for swelling deformation of a surface-confined hydrogel layer, which provides a theoretical understanding of the critical condition for the onset of surface instability. The predicted critical condition depends on the two dimensionless material parameters (Nv and χ) of specific hydrogel systems. In particular, the critical swelling ratio varies from 2.5 to 3.4 for swell-induced

surface instability. Using a nonlinear finite element method, numerical simulations are presented to show the swelling process of a confined hydrogel layer, with evolution of an initial surface perturbation followed by formation of surface creases.

As pointed out previously [81], the surface instability places a fundamental limit on the degree of swelling for a confined hydrogel layer without formation of undesirable surface features for applications such as cell culture and smart surface coatings. Here we suggest that such a limit shall be understood on a system specific basis, which also opens the possibilities to achieve an optimal degree of swelling by selecting a specific solvent system along with molecular structures of the polymer network. Furthermore, theoretical understanding of the critical condition and post-instability surface evolution could also facilitate development of controllable surface patterns in soft materials for a range of applications (e.g., microdevices and tissue engineering) [26].

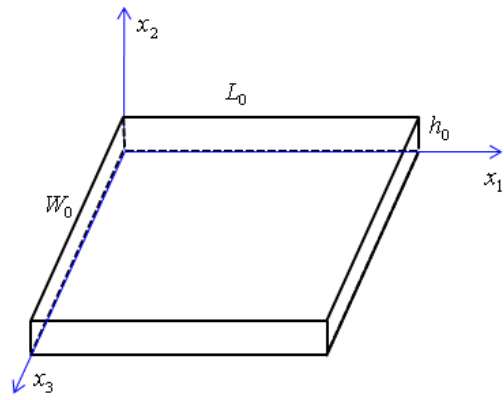
Chapter 4

Effect of pre-stretch on swelling of hydrogels

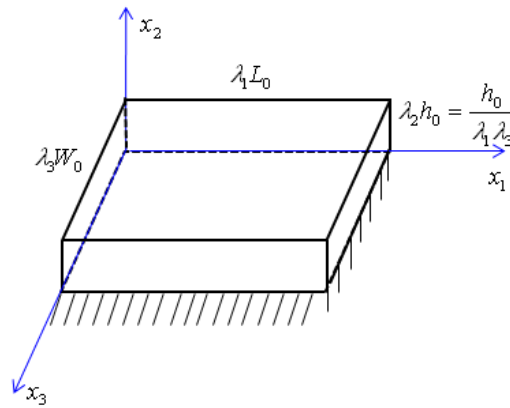
In Chapter 3, the hydrogel layers have been assumed to be in the reference state (no deformation, no stress) before swelling. In practice, however, the polymer network of the hydrogel layer may be subject to a pre-stretch (or compression) before it is attached to the substrate. Subsequently, swelling of the hydrogel layer depends on the pre-stretch. In this chapter, first, we study the effect of pre-stretch on the homogeneous swelling of hydrogel layers. To be specific, an isotropic equi-biaxial pre-stretch and an anisotropic plane-strain stretch are considered as two representative cases. Next, by linear perturbation analyses, we study the effects of pre-stretch on swell-induced surface instability of hydrogels.

4.1. EFFECT OF PRE-STRETCH ON HOMOGENEOUS SWELLING

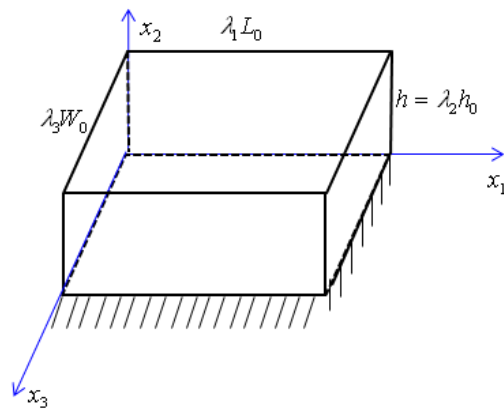
Consider a hydrogel layer as illustrated in Fig. 4.1. The hydrogel layer is initially at rest in the dry state with dimensions L_0 , W_0 , and h_0 as in Fig. 4.1 (a). Let x_1 and x_3 be the in-plane directions and x_2 the out-of-plane direction, or thickness direction. The hydrogel layer is subject to a biaxial pre-stretch in the in-plane directions by λ_1 and λ_3 in the dry state as depicted in Fig. 4.1 (b). As a result, the corresponding out-of-plane stretch is $\lambda_2 = 1/(\lambda_1\lambda_3)$ by the assumption of incompressibility. Then the hydrogel layer is attached to a rigid substrate, and is allowed to swell in a solvent of chemical potential $\hat{\mu}$ as in Fig. 4.1 (c).



(a) Reference state (dry, no stress)



(b) Pre-stretched dry state



(c) Swollen state with pre-stretch

Figure 4.1: Swelling of a hydrogel layer with prescribed in-plane stretches λ_1 and λ_3 .

First, assuming homogeneous swelling for the pre-stretched hydrogel, the volume swelling ratio is simply,

$$J_h = \lambda_1 \lambda_2 \lambda_3 \quad (4.1)$$

and the nominal concentration of the solvent molecule in the hydrogel from molecular incompressibility is

$$C_h = \frac{\lambda_1 \lambda_2 \lambda_3 - 1}{v}. \quad (4.2)$$

where the subscript h stands for the homogeneous state. Then the energy density function in Eq. (3.2) is

$$U_h = \frac{1}{2} N k_B T (\lambda_1^2 + \lambda_2^2 + \lambda_3^2 - 3 - 2 \ln J_h) + \frac{k_B T}{v} \left((J_h - 1) \ln \frac{J_h - 1}{J_h} + \frac{\chi (J_h - 1)}{J_h} \right) \quad (4.3)$$

The total free energy of the system (including the hydrogel and the external solvent) consists of the internal free energy and the chemical/mechanical work done during absorption and swelling, namely,

$$G = U_h V_0 - \hat{\mu} C_h V_0 + (J_h - 1) p V_0 = \left[U_h(\lambda_2) - \frac{\hat{\mu} - p v}{v} (\lambda_1 \lambda_2 \lambda_3 - 1) \right] V_0, \quad (4.4)$$

where V_0 is the reference volume of the layer in the dry state. Note that the external solvent exerts a pressure p onto the surface of the hydrogel layer, which does a negative work and thus increases the free energy as the hydrogel swells.

For a prescribed pre-stretch (λ_1, λ_3) , the equilibrium swelling ratio of the hydrogel can then be determined by minimizing the total free energy. By setting $dG/d\lambda_2 = 0$, we obtain that

$$\ln\left(1 - \frac{1}{\lambda_1\lambda_2\lambda_3}\right) + \frac{1}{\lambda_1\lambda_2\lambda_3} + \frac{\chi}{(\lambda_1\lambda_2\lambda_3)^2} + N\nu\left(\frac{\lambda_2}{\lambda_1\lambda_3} - \frac{1}{\lambda_1\lambda_2\lambda_3}\right) = \frac{\hat{\mu} - p\nu}{k_B T}. \quad (4.5)$$

For prescribed in-plane stretches $(\lambda_1$ and $\lambda_3)$, the corresponding out-of-plane stretch (λ_2) can be calculated from the above equation. At the equilibrium vapor pressure, the out-of-plane stretches for two special cases with respect to the prescribed in-plane

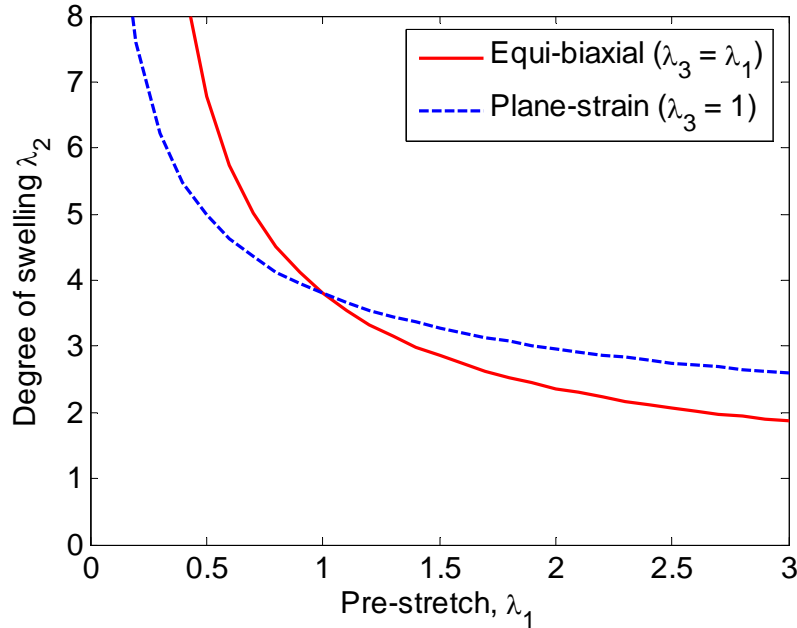


Figure 4.2: Homogeneous swelling of hydrogel films at equilibrium vapor pressure with prescribed lateral stretches for equi-biaxial pre-stretch and for plane-strain pre-stretch ($N\nu = 0.01$, $\chi = 0.1$, and $\bar{p}_0 = 0.000023$).

stretch are presented in Fig. 4.2. One is the equi-biaxial case ($\lambda_1 = \lambda_3$) drawn with the red-solid line, and the other is the plane-strain case ($\lambda_3 = 1$) drawn with the blue-dashed line. Here $N\nu = 0.01$ and $\chi = 0.1$ and $\bar{p}_0 = 0.000023$. When $\lambda_1 < 1$, the hydrogel is initially under compression and when $\lambda_1 > 1$, the hydrogel is initially under tension. The out-of-plane swelling decreases as λ_1 increases. Since $\lambda_1 = \lambda_3$ for the equi-biaxial state, the hydrogel is more compressed than the plane-strain state if $\lambda_1 < 1$, which results in more swelling in the out-of-plane direction and vice versa for $\lambda_1 > 1$.

Referring to Eq. (3.7), the nominal stress is

$$s_{ij} = Nk_B T (F_{ij} + \alpha H_{ij}), \quad (4.6)$$

where

$$\alpha = -\frac{1}{J} + \frac{1}{N\nu} \left(\ln \frac{J-1}{J} + \frac{1}{J} + \frac{\chi}{J^2} - \frac{\hat{\mu}}{k_B T} \right) = -\frac{\lambda_2}{\lambda_1 \lambda_3} - \frac{p}{Nk_B T}, \quad (4.7)$$

$$H_{ij} = \frac{\partial J}{\partial F_{ij}} = \frac{1}{2} e_{ijk} e_{jkl} F_{jK} F_{kL}. \quad (4.8)$$

For the present problem, from Eqs. (4.6) – (4.8), the non-zero dimensionless nominal stress components are

$$\begin{aligned} s_{11} &= Nk_B T \left(\lambda_1 - \frac{\lambda_2^2}{\lambda_1} \right) - p \lambda_2 \lambda_3, \\ s_{22} &= -p \lambda_1 \lambda_3, \\ s_{33} &= Nk_B T \left(\lambda_3 - \frac{\lambda_2^2}{\lambda_3} \right) - p \lambda_1 \lambda_2, \end{aligned} \quad (4.9)$$

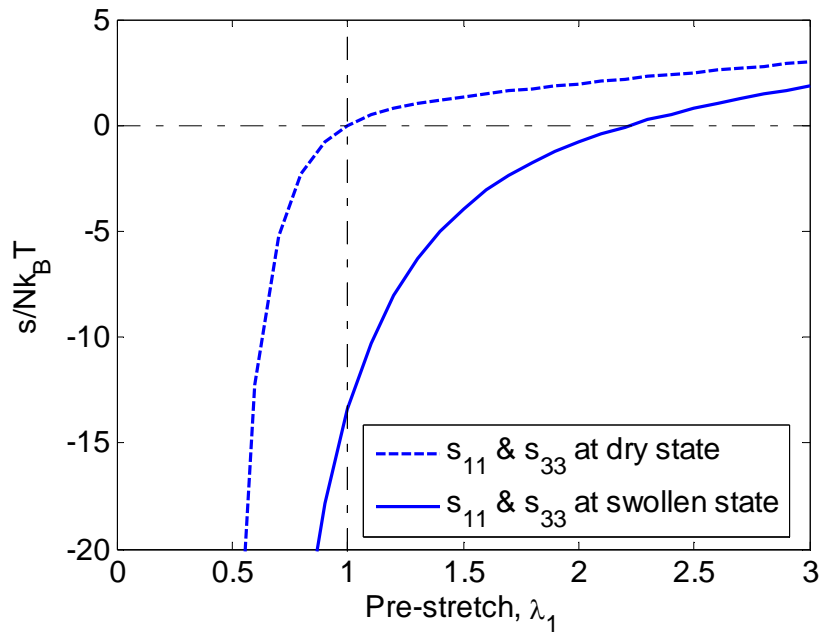
and the corresponding true stresses are

$$\begin{aligned}
\sigma_{11} &= Nk_B T \left(\frac{\lambda_1}{\lambda_2 \lambda_3} - \frac{\lambda_2}{\lambda_1 \lambda_3} \right) - p, \\
\sigma_{22} &= -p, \\
\sigma_{33} &= Nk_B T \left(\frac{\lambda_3}{\lambda_1 \lambda_2} - \frac{\lambda_2}{\lambda_1 \lambda_3} \right) - p.
\end{aligned} \tag{4.10}$$

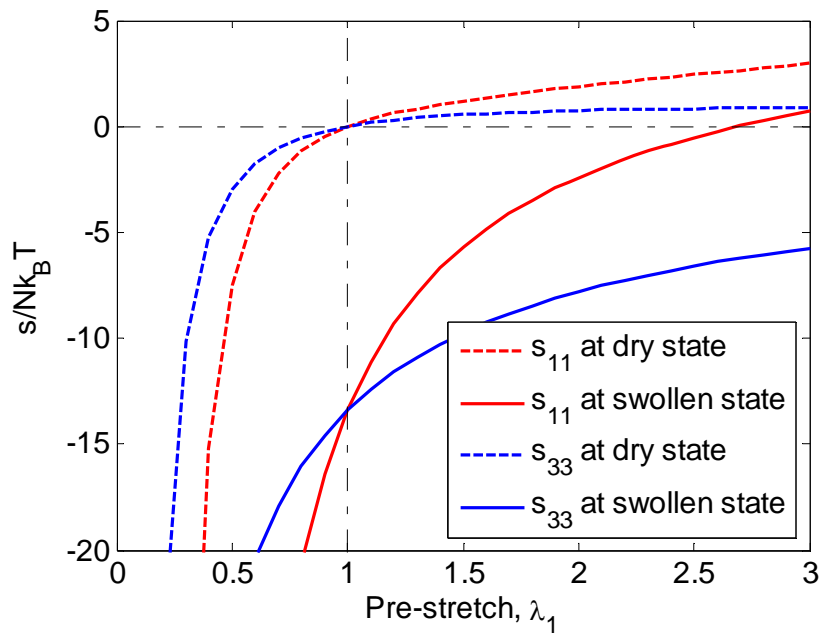
Nominal in-plane stress components during homogeneous swelling with prescribed in-plane stretches are plotted in Fig. 4.3 for (a) equi-biaxial state and for (b) plane-strain state. In the plots, dashed lines represent stresses in the dry state with initial mechanical stretches and solid lines represent stresses in the equilibrium swollen state. The dashed-dotted line indicates zero stress above which the stress is tensile and below which the stress is compressive.

For the equi-biaxial state in Fig 4.3 (a), due to transverse isotropy, the two in-plane stress components s_{11} and s_{33} have the same value. During the swelling process, the in-plane stress shifts towards more compression due to the lateral constraint. Considering that the necessary condition for instability is compressive stress, the in-plane stress initially in tension can be converted to compressive stress during swelling and the hydrogel can become unstable. But when the initial stretch is larger than a certain value, the in-plane stress remains in tension after swelling and it can be expected that the hydrogel swells stably.

For the plane-strain state, as in Fig. 4.3 (b), the difference in the two perpendicular in-plane stretches (λ_1, λ_3) leads to the difference in the corresponding stress components. In Fig. 4.3 (b), s_{11} is colored in red and s_{33} is colored in blue. Since λ_3 is fixed at 1, the x_1 direction experiences more compression when $\lambda_1 < 1$ and the x_3



(a)



(b)

Figure 4.3: Nominal in-plane stress components with respect to the prescribed in-plane stretches at equilibrium state. ($N\nu = 0.01$ and $\chi = 0.1$) ; (a) Equibiaxial pre-stretch ($\lambda_1 = \lambda_3$), (b) Plane-strain pre-stretch ($\lambda_3 = 1$).

direction experiences more compression when $\lambda_1 > 1$. This can be seen as the maximum compressive stress shift across $\lambda_1 = 1$ in Fig. 4.3 (b). When $\lambda_1 = 1$, the results of both the plane-strain case and the equi-biaxial case are identical. If we assume that the instability prefers the maximum compression direction then the change of the instability direction may be expected in the plane-strain state. This will be studied in detail in the following section. Unlike the equi-biaxial case, even when s_{11} becomes tensile after swelling for a relatively large pre-stretch (λ_1), the x_3 direction still undergoes compressive stress due to the plane strain condition and it is thus possible to have surface instability in the x_3 direction.

4.2. THREE-DIMENSIONAL LINEAR PERTURBATION ANALYSIS

Based on the homogeneous solution obtained in the previous section, we introduce small perturbed displacement fields. As explained in the last paragraph of the previous section, since surface instability has dependence on direction for plane-strain case, perturbation is applied in all three directions.

$$u_1 = u_1(x_1, x_2, x_3), \quad u_2 = u_2(x_1, x_2, x_3), \quad \text{and} \quad u_3 = u_3(x_1, x_2, x_3). \quad (4.11)$$

After the perturbation, the deformation gradient from the dry state becomes

$$\tilde{\mathbf{F}} = \begin{bmatrix} \lambda_1 \left(1 + \frac{\partial u_1}{\partial x_1} \right) & \lambda_2 \frac{\partial u_1}{\partial x_2} & \lambda_3 \frac{\partial u_1}{\partial x_3} \\ \lambda_1 \frac{\partial u_2}{\partial x_1} & \lambda_2 \left(1 + \frac{\partial u_2}{\partial x_2} \right) & \lambda_3 \frac{\partial u_2}{\partial x_3} \\ \lambda_1 \frac{\partial u_3}{\partial x_1} & \lambda_2 \frac{\partial u_3}{\partial x_2} & \lambda_3 \left(1 + \frac{\partial u_3}{\partial x_3} \right) \end{bmatrix}. \quad (4.12)$$

Then the volume change after linearization is

$$\tilde{J} = \det(\tilde{\mathbf{F}}) \approx \lambda_1 \lambda_2 \lambda_3 \left(1 + \frac{\partial u_1}{\partial x_1} + \frac{\partial u_2}{\partial x_2} + \frac{\partial u_3}{\partial x_3} \right) = J_h (1 + \varepsilon), \quad (4.13)$$

where $\varepsilon = \frac{\partial u_1}{\partial x_1} + \frac{\partial u_2}{\partial x_2} + \frac{\partial u_3}{\partial x_3}$ and $J_h = \lambda_1 \lambda_2 \lambda_3$ is the volume ratio of the homogeneous

state. The perturbed concentration field is

$$\nu C = J - 1 \approx J_h (1 + \varepsilon) - 1 = \nu C_h + J_h \varepsilon. \quad (4.14)$$

Then the nominal stress is obtained from Eqs. (4.6) – (4.8) with the following change in Eq. (4.7):

$$\begin{aligned} \tilde{\alpha} &= -\frac{1}{J} + \frac{1}{N\nu} \left(\ln \frac{J-1}{J} + \frac{1}{J} + \frac{\chi}{J^2} - \frac{\hat{\mu}}{k_B T} \right) \\ &\approx -\frac{1}{J_h} + \frac{1}{N\nu} \left(\ln \frac{J_h-1}{J_h} + \frac{1}{J_h} + \frac{\chi}{J_h^2} - \frac{\mu}{k_B T} \right) + \varepsilon \left[\frac{1}{J_h} + \frac{1}{N\nu} \left(\frac{1}{J_h-1} - \frac{1}{J_h} - \frac{2\chi}{J_h^2} \right) \right]. \end{aligned} \quad (4.15)$$

Substitution of the chemical potential, Eq. (4.5) into (4.15) gives

$$\tilde{\alpha} = -\frac{\lambda_2}{\lambda_1 \lambda_3} - \frac{p}{Nk_B T} + \xi_h \varepsilon, \quad (4.16)$$

where

$$\xi_h = \frac{1}{J_h} + \frac{1}{N\nu} \left(\frac{1}{J_h-1} - \frac{1}{J_h} - \frac{2\chi}{J_h^2} \right). \quad (4.17)$$

Then the nominal stress in Eq. (4.6) becomes

$$s_{ij} = Nk_B T \left[\tilde{F}_{ij} + \tilde{H}_{ij} \left(-\frac{\lambda_2}{\lambda_1 \lambda_3} + \xi_h \varepsilon \right) \right] - p \tilde{H}_{ij}. \quad (4.18)$$

Expanding the above equation gives the following stress components explicitly:

$$\frac{s_{11}}{Nk_B T} \approx \bar{s}_{11}^h + (\lambda_1 + \lambda_2 \lambda_3 \xi_h) \frac{\partial u_1}{\partial x_1} + \left(\lambda_2 \lambda_3 \xi_h - \frac{\lambda_2^2}{\lambda_1} \right) \left(\frac{\partial u_2}{\partial x_2} + \frac{\partial u_3}{\partial x_3} \right) - \bar{p} \lambda_2 \lambda_3 \left(\frac{\partial u_2}{\partial x_2} + \frac{\partial u_3}{\partial x_3} \right), \quad (4.19)$$

$$\frac{s_{22}}{Nk_B T} \approx \bar{s}_{22}^h + (\lambda_1 \lambda_3 \xi_h - \lambda_2) \left(\frac{\partial u_1}{\partial x_1} + \frac{\partial u_3}{\partial x_3} \right) + (\lambda_1 \lambda_3 \xi_h + \lambda_2) \frac{\partial u_2}{\partial x_2} - \bar{p} \lambda_1 \lambda_3 \left(\frac{\partial u_1}{\partial x_1} + \frac{\partial u_3}{\partial x_3} \right), \quad (4.20)$$

$$\frac{s_{33}}{Nk_B T} \approx \bar{s}_{33}^h + \left(\lambda_1 \lambda_2 \xi_h - \frac{\lambda_2^2}{\lambda_3} \right) \left(\frac{\partial u_1}{\partial x_1} + \frac{\partial u_2}{\partial x_2} \right) + (\lambda_3 + \lambda_1 \lambda_2 \xi_h) \frac{\partial u_3}{\partial x_3} - \bar{p} \lambda_1 \lambda_2 \left(\frac{\partial u_1}{\partial x_1} + \frac{\partial u_2}{\partial x_2} \right), \quad (4.21)$$

$$\frac{s_{12}}{Nk_B T} \approx \lambda_2 \left(\frac{\partial u_1}{\partial x_2} + \frac{\partial u_2}{\partial x_1} \right) + \bar{p} \lambda_1 \lambda_3 \frac{\partial u_2}{\partial x_1}, \quad (4.22)$$

$$\frac{s_{13}}{Nk_B T} \approx \lambda_3 \frac{\partial u_1}{\partial x_3} + \frac{\lambda_2^2}{\lambda_3} \frac{\partial u_3}{\partial x_1} + \bar{p} \lambda_1 \lambda_2 \frac{\partial u_3}{\partial x_1}, \quad (4.23)$$

$$\frac{s_{21}}{Nk_B T} \approx \lambda_1 \frac{\partial u_2}{\partial x_1} + \frac{\lambda_2^2}{\lambda_1} \frac{\partial u_1}{\partial x_2} + \bar{p} \lambda_2 \lambda_3 \frac{\partial u_1}{\partial x_2}, \quad (4.24)$$

$$\frac{s_{23}}{Nk_B T} \approx \lambda_3 \frac{\partial u_2}{\partial x_3} + \frac{\lambda_2^2}{\lambda_3} \frac{\partial u_3}{\partial x_2} + \bar{p} \lambda_1 \lambda_2 \frac{\partial u_3}{\partial x_2}, \quad (4.25)$$

$$\frac{s_{31}}{Nk_B T} \approx \lambda_1 \frac{\partial u_3}{\partial x_1} + \frac{\lambda_2^2}{\lambda_1} \frac{\partial u_1}{\partial x_3} + \bar{p} \lambda_2 \lambda_3 \frac{\partial u_1}{\partial x_3}, \quad (4.26)$$

$$\frac{s_{32}}{Nk_B T} \approx \lambda_2 \left(\frac{\partial u_2}{\partial x_3} + \frac{\partial u_3}{\partial x_2} \right) + \bar{p} \lambda_1 \lambda_3 \frac{\partial u_2}{\partial x_3}, \quad (4.27)$$

where superscript h stands for the homogeneous solution. Note that the nominal stress is not symmetric.

The equilibrium equations are

$$\begin{aligned}
\frac{\partial s_{11}}{\partial X_1} + \frac{\partial s_{12}}{\partial X_2} + \frac{\partial s_{13}}{\partial X_3} &= \lambda_1 \frac{\partial s_{11}}{\partial x_1} + \lambda_2 \frac{\partial s_{12}}{\partial x_2} + \lambda_3 \frac{\partial s_{13}}{\partial x_3} = 0 \\
\frac{\partial s_{21}}{\partial X_1} + \frac{\partial s_{22}}{\partial X_2} + \frac{\partial s_{23}}{\partial X_3} &= \lambda_1 \frac{\partial s_{21}}{\partial x_1} + \lambda_2 \frac{\partial s_{22}}{\partial x_2} + \lambda_3 \frac{\partial s_{23}}{\partial x_3} = 0 \quad . \\
\frac{\partial s_{31}}{\partial X_1} + \frac{\partial s_{32}}{\partial X_2} + \frac{\partial s_{33}}{\partial X_3} &= \lambda_1 \frac{\partial s_{31}}{\partial x_1} + \lambda_2 \frac{\partial s_{32}}{\partial x_2} + \lambda_3 \frac{\partial s_{33}}{\partial x_3} = 0
\end{aligned} \tag{4.28}$$

Substitution of Eqs. (4.19) – (4.27) into the equilibrium equations gives

$$\begin{aligned}
(\lambda_1^2 + \lambda_1 \lambda_2 \lambda_3 \xi_h) \frac{\partial^2 u_1}{\partial x_1^2} + \lambda_2^2 \frac{\partial^2 u_1}{\partial x_2^2} + \lambda_3^2 \frac{\partial^2 u_1}{\partial x_3^2} + \lambda_1 \lambda_2 \lambda_3 \xi_h \left(\frac{\partial^2 u_2}{\partial x_1 \partial x_2} + \frac{\partial^2 u_3}{\partial x_1 \partial x_3} \right) &= 0, \\
\lambda_1^2 \frac{\partial^2 u_2}{\partial x_1^2} + (\lambda_2^2 + \lambda_1 \lambda_2 \lambda_3 \xi_h) \frac{\partial^2 u_2}{\partial x_2^2} + \lambda_3^2 \frac{\partial^2 u_2}{\partial x_3^2} + \lambda_1 \lambda_2 \lambda_3 \xi_h \left(\frac{\partial^2 u_1}{\partial x_1 \partial x_2} + \frac{\partial^2 u_3}{\partial x_2 \partial x_3} \right) &= 0, \tag{4.29} \\
\lambda_1^2 \frac{\partial^2 u_3}{\partial x_1^2} + \lambda_2^2 \frac{\partial^2 u_3}{\partial x_2^2} + (\lambda_3^2 + \lambda_1 \lambda_2 \lambda_3 \xi_h) \frac{\partial^2 u_3}{\partial x_3^2} + \lambda_1 \lambda_2 \lambda_3 \xi_h \left(\frac{\partial^2 u_1}{\partial x_1 \partial x_3} + \frac{\partial^2 u_2}{\partial x_2 \partial x_3} \right) &= 0.
\end{aligned}$$

A two-dimensional Fourier transform with respect to x_1 and x_3 is performed. This leads to the following:

$$\begin{aligned}
-k_1^2 (\lambda_1^2 + \lambda_1 \lambda_2 \lambda_3 \xi_h) \hat{u}_1 + \lambda_2^2 \frac{\partial^2 \hat{u}_1}{\partial x_2^2} - k_3^2 \lambda_3^2 \hat{u}_1 + ik_1 \lambda_1 \lambda_2 \lambda_3 \xi_h \frac{\partial \hat{u}_2}{\partial x_2} - k_1 k_3 \lambda_1 \lambda_2 \lambda_3 \xi_h \hat{u}_3 &= 0, \\
-k_1^2 \lambda_1^2 \hat{u}_2 + (\lambda_2^2 + \lambda_1 \lambda_2 \lambda_3 \xi_h) \frac{\partial^2 \hat{u}_2}{\partial x_2^2} - k_3^2 \lambda_3^2 \hat{u}_2 + ik_1 \lambda_1 \lambda_2 \lambda_3 \xi_h \frac{\partial \hat{u}_1}{\partial x_2} + ik_3 \lambda_1 \lambda_2 \lambda_3 \xi_h \frac{\partial \hat{u}_3}{\partial x_2} &= 0, \tag{4.30} \\
-k_1^2 \lambda_1^2 \hat{u}_3 + \lambda_2^2 \frac{\partial^2 \hat{u}_3}{\partial x_2^2} - k_3^2 (\lambda_3^2 + \lambda_1 \lambda_2 \lambda_3 \xi_h) \hat{u}_3 - k_1 k_3 \lambda_1 \lambda_2 \lambda_3 \xi_h \hat{u}_1 + ik_3 \lambda_1 \lambda_2 \lambda_3 \xi_h \frac{\partial \hat{u}_2}{\partial x_2} &= 0.
\end{aligned}$$

where $\hat{u}_1(k_1, k_3, x_2)$, $\hat{u}_2(k_1, k_3, x_2)$, and $\hat{u}_3(k_1, k_3, x_2)$ are Fourier transforms of $u_1(x_1, x_2, x_3)$, $u_2(x_1, x_2, x_3)$, and $u_3(x_1, x_2, x_3)$, and can be expressed as

$$\begin{aligned}
\hat{u}_1 &= \bar{u}_1(k_1, k_3) \exp(qx_2) \\
\hat{u}_2 &= \bar{u}_2(k_1, k_3) \exp(qx_2). \\
\hat{u}_3 &= \bar{u}_3(k_1, k_3) \exp(qx_2)
\end{aligned} \tag{4.31}$$

Substitution of Eq. (4.31) into Eq. (4.30) gives an eigenvalue problem for the eigenvector $(\bar{u}_1, \bar{u}_2, \bar{u}_3)$. The characteristic equation is

$$\begin{vmatrix}
q^2 \lambda_2^2 - k_1^2 (\lambda_1^2 + J_h \xi_h) - k_3^2 \lambda_3^2 & ik_1 J_h \xi_h q & -k_1 k_3 J_h \xi_h \\
ik_1 J_h \xi_h q & (\lambda_2^2 + J_h \xi_h) q^2 - k_1^2 \lambda_1^2 - k_3^2 \lambda_3^2 & ik_3 J_h \xi_h q \\
-k_1 k_3 J_h \xi_h & ik_3 J_h \xi_h q & q^2 \lambda_2^2 - k_1^2 \lambda_1^2 - k_3^2 (\lambda_3^2 + J_h \xi_h)
\end{vmatrix} = 0 \tag{4.32}$$

This equation gives six eigenvalues for q .

$$q_{1,2} = \frac{(k_1^2 \lambda_1^2 + k_3^2 \lambda_3^2)^{1/2}}{\lambda_2}, \quad q_{3,4} = -q_{1,2} \quad \text{and} \quad q_{5,6} = \pm \sqrt{\frac{k_1^2 \lambda_1^2 + k_3^2 \lambda_3^2 + J_h \xi_h (k_1^2 + k_3^2)}{\lambda_2^2 + J_h \xi_h}} \tag{4.33}$$

with six eigenvectors,

$$\begin{bmatrix} \bar{u}_1^{(1)} & \bar{u}_1^{(2)} & \bar{u}_1^{(3)} & \bar{u}_1^{(4)} & \bar{u}_1^{(5)} & \bar{u}_1^{(6)} \\ \bar{u}_2^{(1)} & \bar{u}_2^{(2)} & \bar{u}_2^{(3)} & \bar{u}_2^{(4)} & \bar{u}_2^{(5)} & \bar{u}_2^{(6)} \\ \bar{u}_3^{(1)} & \bar{u}_3^{(2)} & \bar{u}_3^{(3)} & \bar{u}_3^{(4)} & \bar{u}_3^{(5)} & \bar{u}_3^{(6)} \end{bmatrix} = \begin{bmatrix} 1 & 0 & 1 & 0 & k_1 & k_1 \\ -i \frac{k_1}{q_1} & -i \frac{k_3}{q_1} & i \frac{k_1}{q_1} & i \frac{k_3}{q_1} & -iq_5 & iq_5 \\ 0 & 1 & 0 & 1 & k_3 & k_3 \end{bmatrix}. \tag{4.34}$$

Note that there are two pairs of repeated roots in Eq. (4.33), each with two linearly independent eigenvectors as in Eq. (4.34). Besides the above eigenvalues and eigenvectors, we can think of two degenerated cases for this eigenvalue problem in Eq. (4.32), as given in Appendix C.

The complete solution takes the form

$$\begin{aligned}
\hat{u}_1(k_1, k_3, x_2) &= \sum_{n=1}^6 A_n \bar{u}_1^{(n)}(k_1, k_3) \exp(q_n x_2) \\
\hat{u}_2(k_1, k_3, x_2) &= \sum_{n=1}^6 A_n \bar{u}_2^{(n)}(k_1, k_3) \exp(q_n x_2) \quad . \\
\hat{u}_3(k_1, k_3, x_2) &= \sum_{n=1}^6 A_n \bar{u}_3^{(n)}(k_1, k_3) \exp(q_n x_2)
\end{aligned} \tag{4.35}$$

To determine the unknown coefficients A_n , boundary conditions should be applied. From the bonding of the lower surface of the hydrogel layer to the rigid substrate,

$$u_1 = u_2 = u_3 = 0 \quad \text{at} \quad x_2 = 0. \tag{4.36}$$

From the upper surface of the hydrogel layer, the nominal traction is

$$T \approx p\lambda_1\lambda_3 \left(1 + \frac{\partial u_1}{\partial x_1} + \frac{\partial u_3}{\partial x_3} \right), \tag{4.37}$$

and the direction is perpendicular to the perturbed surface with the unit vector,

$$n_1 \approx \frac{\partial u_2}{\partial x_1}, \quad n_2 \approx -1, \quad \text{and} \quad n_3 \approx \frac{\partial u_2}{\partial x_3}. \tag{4.38}$$

Therefore, the traction boundary condition at the upper surface is as follows to the first order of perturbation

$$s_{12} = p\lambda_1\lambda_3 \frac{\partial u_2}{\partial x_1}, \quad s_{22} = -p\lambda_1\lambda_3 \left(1 + \frac{\partial u_1}{\partial x_1} + \frac{\partial u_3}{\partial x_3} \right), \quad \text{and} \quad s_{32} = p\lambda_1\lambda_3 \frac{\partial u_2}{\partial x_3} \quad \text{at} \quad x_2 = h \tag{4.39}$$

where h is the thickness of the hydrogel in the swollen state.

The boundary conditions in Eqs. (4.36) and (4.39) can then be expressed with Eq. (4.35). This generates the eigenvalue problem for eigenvector A_n . In matrix form,

$$\sum_{m,n}^6 D_{mn}(kh_0, \lambda_h) A_n = 0, \quad (4.40)$$

where D_{mn} is

$$\begin{bmatrix} 1 & 0 & 1 \\ -\frac{k_1}{q_1} & -\frac{k_3}{q_1} & \frac{k_1}{q_1} \\ 0 & 1 & 0 \\ 2\lambda_2 k_1 e^{q_1 \lambda_2 h_0} & 2\lambda_2 k_3 e^{q_1 \lambda_2 h_0} & 2\lambda_2 k_1 e^{-q_1 \lambda_2 h_0} \\ \lambda_2 \left(q_1 + \frac{k_1^2}{q_1} \right) e^{q_1 \lambda_2 h_0} & \lambda_2 \frac{k_1 k_3}{q_1} e^{q_1 \lambda_2 h_0} & -\lambda_2 \left(q_1 + \frac{k_1^2}{q_1} \right) e^{-q_1 \lambda_2 h_0} \\ \lambda_2 \frac{k_1 k_3}{q_1} e^{q_1 \lambda_2 h_0} & \lambda_2 \left(q_1 + \frac{k_3^2}{q_1} \right) e^{q_1 \lambda_2 h_0} & -\lambda_2 \frac{k_1 k_3}{q_1} e^{-q_1 \lambda_2 h_0} \\ 0 & k_1 & k_1 \\ \frac{k_3}{q_1} & -q_5 & q_5 \\ 1 & k_3 & k_3 \\ 2\lambda_2 k_3 e^{-q_1 \lambda_2 h_0} & \alpha e^{q_5 \lambda_2 h_0} & \alpha e^{-q_5 \lambda_2 h_0} \\ -\lambda_2 \frac{k_1 k_3}{q_1} e^{-q_1 \lambda_2 h_0} & 2\lambda_2 q_5 k_1 e^{q_5 \lambda_2 h_0} & -2\lambda_2 q_5 k_1 e^{-q_5 \lambda_2 h_0} \\ -\lambda_2 \left(q_1 + \frac{k_3^2}{q_1} \right) e^{-q_1 \lambda_2 h_0} & 2\lambda_2 q_5 k_3 e^{q_5 \lambda_2 h_0} & -2\lambda_2 q_5 k_3 e^{-q_5 \lambda_2 h_0} \end{bmatrix} \quad (4.41)$$

where

$$\alpha = \frac{1}{\lambda_2} \left[k_1^2 \lambda_1^2 + \lambda_2^2 (k_1^2 + k_3^2) + k_3^2 \lambda_3^2 \right]. \quad (4.42)$$

The characteristic equation is then

$$\det(D_{mn}) = f(\lambda_2; k_1, k_3, \lambda_1, \lambda_3, Nv, \chi) = 0. \quad (4.43)$$

The three stretches are coupled through the relation between the swelling ratios and the chemical potential in Eq. (4.5).

At this point, it is worthwhile mentioning Biot's analysis of surface instability of homogeneous half-space rubber under pure mechanical compression [84]. Under the incompressibility condition of rubber ($\lambda_1\lambda_2\lambda_3 = 1$), he reached the following characteristic equation,

$$\zeta^3 + 2\zeta^2 - 2 = 0 \quad (4.44)$$

where

$$\zeta = \frac{-\sigma_{11}}{Nk_B T(\lambda_2^2 + \lambda_1^2)} = \frac{\lambda_2^2 - \lambda_1^2}{\lambda_2^2 + \lambda_1^2}. \quad (4.45)$$

Eq. (4.44) has only one real root, $\zeta = 0.839$. This solution combined with the equi-biaxial condition ($\lambda_1 = \lambda_3$) and Eq. (4.45) yields $\lambda_1^c = 0.666$, $\sigma_{11}^c = -4.64Nk_B T$ for the critical conditions. In the same way, the critical conditions for the plane strain condition ($\lambda_3=1$) are $\lambda_1^c = 0.544$, $\sigma_{11}^c = -3.08Nk_B T$. These critical conditions are independent of the perturbation wavelength. In the following sections, the coupled effect of swelling and mechanical compression is studied.

4.3. EFFECT OF EQUI-BIAXIAL PRE-STRETCH ON SURFACE INSTABILITY

Figure 4.4 shows the critical out-of-plane swelling ratio λ_2 with respect to the wavenumbers k_1 and k_3 for $N\nu = 0.01$, $\chi = 0.1$, $\bar{p}_0 = 0.000023$, and $\lambda_1 = \lambda_3 = 0.9$. The critical swelling ratio shows a circular shape distribution indicating direction independence due to transverse isotropy of equi-biaxial state. The empty circular region for small wavenumbers means that no solution for Eq. (4.43) is found and the hydrogel

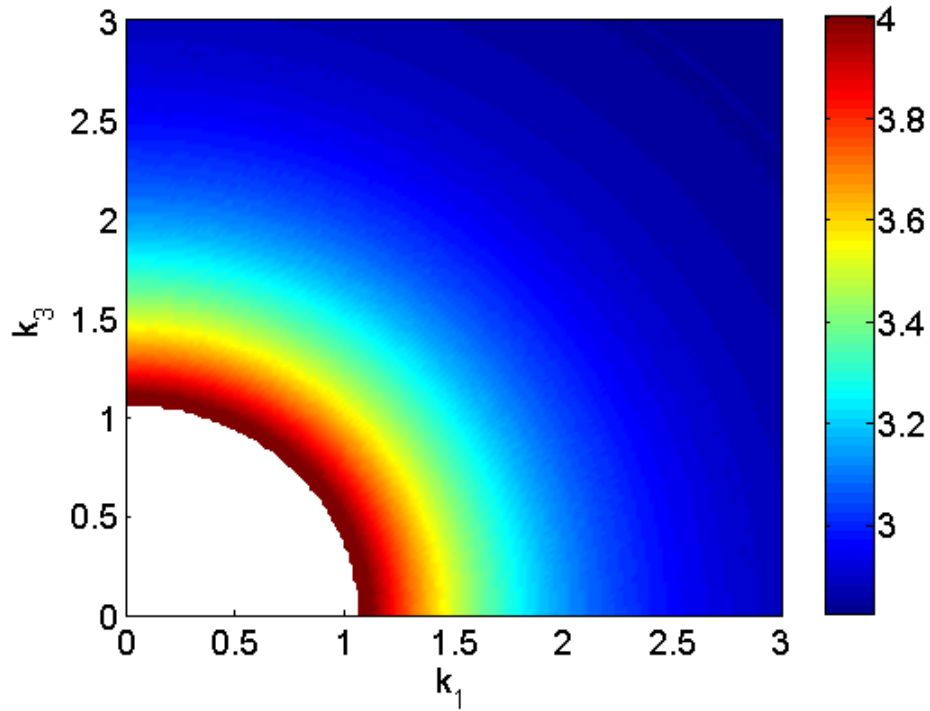


Figure 4.4: Color contours of critical swelling ratio (λ_2) vs. wavenumbers (k_1 and k_3) for $N\nu = 0.01$, $\chi = 0.1$, $\bar{p}_0 = 0.000023$, and $\lambda_1 = \lambda_3 = 0.9$.

layer will not become unstable for the perturbation with the wavenumbers in that region. Except for this region, as the wavenumber increases, the critical swelling ratio gradually decreases from its maximum value equal to the homogeneous swelling ratio for given material parameters. Considering the swelling process, the minimum critical swelling ratio is the dominant critical condition for instability which can be found at large wavenumbers or short wavelengths.

Based on the transverse isotropy shown in Fig. 4.4, without losing generality we can choose $k_3=0$ and simplify Eq.(4.41). Then

$$\det(D_{mn}) = \begin{vmatrix} 1 & 1 & 1 & 1 \\ -\frac{\lambda_2}{\lambda_1} & \frac{\lambda_2}{\lambda_1} & -\sqrt{\frac{\lambda_1^2 + J_h \xi_h}{\lambda_2^2 + J_h \xi_h}} & \sqrt{\frac{\lambda_1^2 + J_h \xi_h}{\lambda_2^2 + J_h \xi_h}} \\ 2\lambda_2 e^{q_1 \lambda_2 h_0} & 2\lambda_2 e^{-q_1 \lambda_2 h_0} & \frac{\lambda_1^2 + \lambda_2^2}{\lambda_2} e^{q_5 \lambda_2 h_0} & \frac{\lambda_1^2 + \lambda_2^2}{\lambda_2} e^{-q_5 \lambda_2 h_0} \\ \frac{\lambda_1^2 + \lambda_2^2}{\lambda_1} e^{q_1 \lambda_2 h_0} & -\frac{\lambda_1^2 + \lambda_2^2}{\lambda_1} e^{-q_1 \lambda_2 h_0} & 2\lambda_2 \sqrt{\frac{\lambda_1^2 + J_h \xi_h}{\lambda_2^2 + J_h \xi_h}} e^{q_5 \lambda_2 h_0} & -2\lambda_2 \sqrt{\frac{\lambda_1^2 + J_h \xi_h}{\lambda_2^2 + J_h \xi_h}} e^{-q_5 \lambda_2 h_0} \end{vmatrix} \quad (4.46)$$

It is shown that the critical swelling ratio decreases as the wavenumber increases. For a wavenumber of infinity ($kh_0 \rightarrow \infty$), the matrix in Eq. (4.46) can be further simplified as

$$\det(D_{mn}^\infty) = \begin{vmatrix} 1 & 1 & 1 & 1 \\ -\frac{\lambda_2}{\lambda_1} & \frac{\lambda_2}{\lambda_1} & -\sqrt{\frac{\lambda_1^2 + J_h \xi_h}{\lambda_2^2 + J_h \xi_h}} & \sqrt{\frac{\lambda_1^2 + J_h \xi_h}{\lambda_2^2 + J_h \xi_h}} \\ 2\lambda_2 e^{q_1 \lambda_2 h_0} & 0 & \frac{\lambda_1^2 + \lambda_2^2}{\lambda_2} e^{q_5 \lambda_2 h_0} & 0 \\ \frac{\lambda_1^2 + \lambda_2^2}{\lambda_1} e^{q_1 \lambda_2 h_0} & 0 & 2\lambda_2 \sqrt{\frac{\lambda_1^2 + J_h \xi_h}{\lambda_2^2 + J_h \xi_h}} e^{q_5 \lambda_2 h_0} & 0 \end{vmatrix}. \quad (4.47)$$

This matrix can be reduced to the characteristic equation of the 2-D plane-strain model in Chapter 3 by setting $\lambda_1 = 1$.

From the matrix in Eq. (4.47), a stability map in the plane of the in-plane swelling ratio (λ_1) and the critical out-of-plane swelling ratio (λ_2) can be constructed and a typical case is shown in Fig. 4.5. The material parameters $N\nu$ and χ in the plot are 0.01 and 0.1, respectively. To understand the stability map, we need to consider three limiting cases. The first case is that the hydrogel is in the dry state and experiences lateral pressure only.

In the dry state, the concentration is zero and the molecular incompressibility condition is changed to the incompressibility condition of the polymer network ($\lambda_1\lambda_2\lambda_3 = \lambda_1^2\lambda_2 = 1$), which is plotted as the lower bound dashed line in Fig. 4.5. Then the whole system is turned into the deformation of the incompressible polymer under in-plane pressure. Another limiting case is when there is no lateral confinement. Then the swelling is just like 3-dimensional isotropic free swelling ($\lambda_1 = \lambda_2 = \lambda_3$), plotted as the straight dashed line passing through A to F in Fig. 4.5. The last limiting case is when the chemical potential is zero. A hydrogel keeps swelling until the chemical potential reaches zero, and

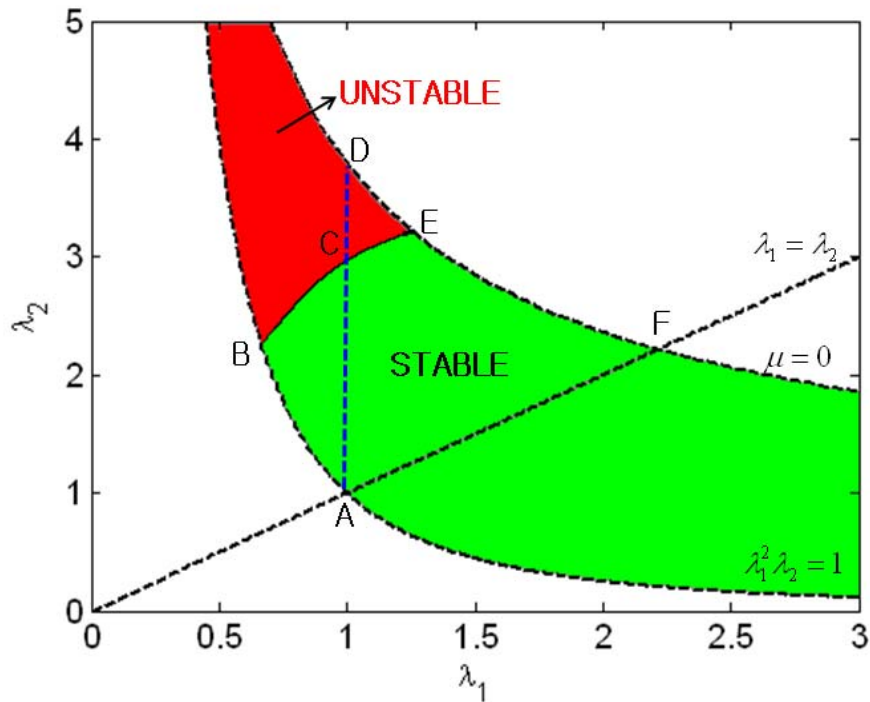


Figure 4.5: A stability map for hydrogels under equi-biaxial pre-stretch ($N\nu = 0.01$, $\chi = 0.1$).

at zero chemical potential, the hydrogel is in its fully swollen state. Unlike other limiting cases, the zero chemical potential condition is dependent on the material parameters $N\nu$ and χ , which is plotted in Fig. 4.5 as the upper bound dashed line. Once we set up the above three limiting cases, the area of feasible deformation is bounded by the incompressibility condition and the zero chemical potential condition. In this area, above the free swelling line (path A-F, $\lambda_1 = \lambda_2 = \lambda_3$), the hydrogel layer experiences compression in the in-plane direction. Now the solution of Eq. (4.47) decides the critical instability condition, which is drawn with the solid line dividing the two colors (path B-C-E). The hydrogel layer is unstable above the line and stable below the line.

Let us look at how the hydrogel layer deforms. Hydrogel in the dry state with no in-plane constraint is marked as A on the map. If pure mechanical compression is exerted in the in-plane direction in the dry state, then the deformation follows the lower limit line and reaches point B where the hydrogel become unstable. Thus point B is the critical surface instability condition under pure mechanical in-plane compression and the corresponding in-plane stretch is $\lambda_B = 0.666$ which is equal to the critical surface instability condition of half-space incompressible rubbery material under equi-biaxial compression as stated in the previous section. When the hydrogel layer swells with fixed in-plane stretch of 1 ($\lambda_1 = 1$), it starts from A, follows the vertical dashed line, and becomes unstable at C. For a pre-stretch in between ($0.666 < \lambda_1 < 1$), the hydrogel layer becomes unstable at a critical swelling ratio (λ_2) between 2.25 at B and 2.98 at C under the combined loading of mechanical compression and swelling for the given material

properties. For a pre-stretch greater than 1 ($\lambda_1 > 1$), there exists a critical stretch (λ_E), beyond which the hydrogel swells homogeneously without surface instability. In other words, λ_E can be interpreted as the critical pre-stretch to stabilize the swelling of the hydrogel.

The critical swelling ratios are presented in Fig. 4.6 (a) for different values of $N\nu$. χ is fixed at 0.1 for all cases. Zero chemical potential limiting cases are drawn with dashed lines of the same color as the corresponding critical conditions in Fig. 4.6 (a). The black dashed line indicates the incompressibility of polymer network ($\lambda_1\lambda_2\lambda_3 = \lambda_1^2\lambda_2 = 1$). All critical conditions start from the same point, which is the surface instability condition of rubber under compression as stated in the previous paragraph. This point shows material independence of the critical condition, which is in agreement with Biot's result [84]. However, once swelling is involved before the instability happens, the critical condition is a function of material properties.

The corresponding critical in-plane true stress ($\sigma_{11} = \sigma_{33}$) is plotted for various $N\nu$ in Fig. 4.6 (b). These are the critical stresses along path B-C-E in Fig. 4.5 for different $N\nu$ values. At point B, the critical stress under pure mechanical compression is $-4.64Nk_B T$ regardless of $N\nu$. This value is identical to Biot's results for the equi-biaxial case. The critical stress value increases as λ_1 increases, showing that swell-induced instability occurs under less compressive stress than does the instability under pure mechanical compression.

Further investigation of point E in Fig. 4.5 is performed. The in-plane pre-stretch

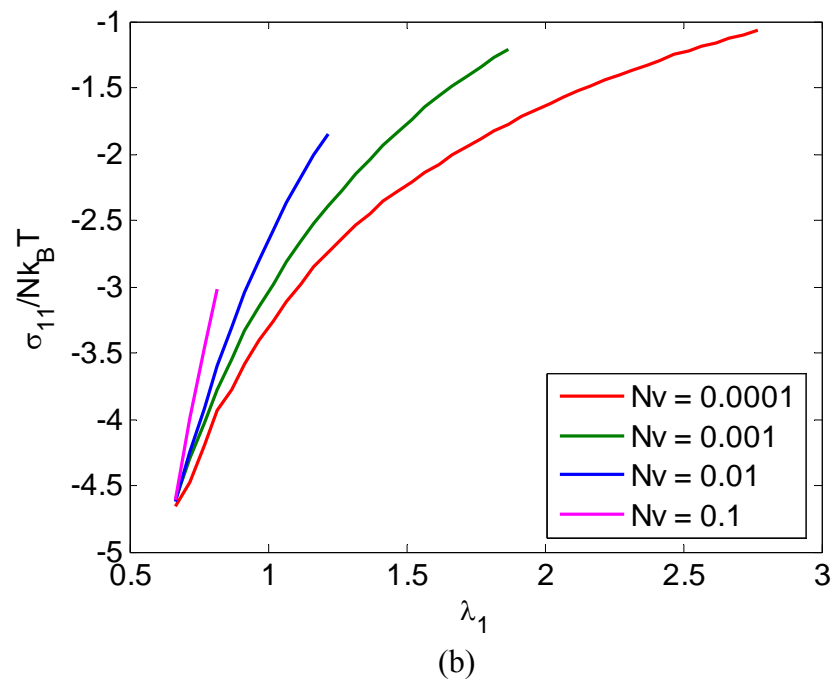
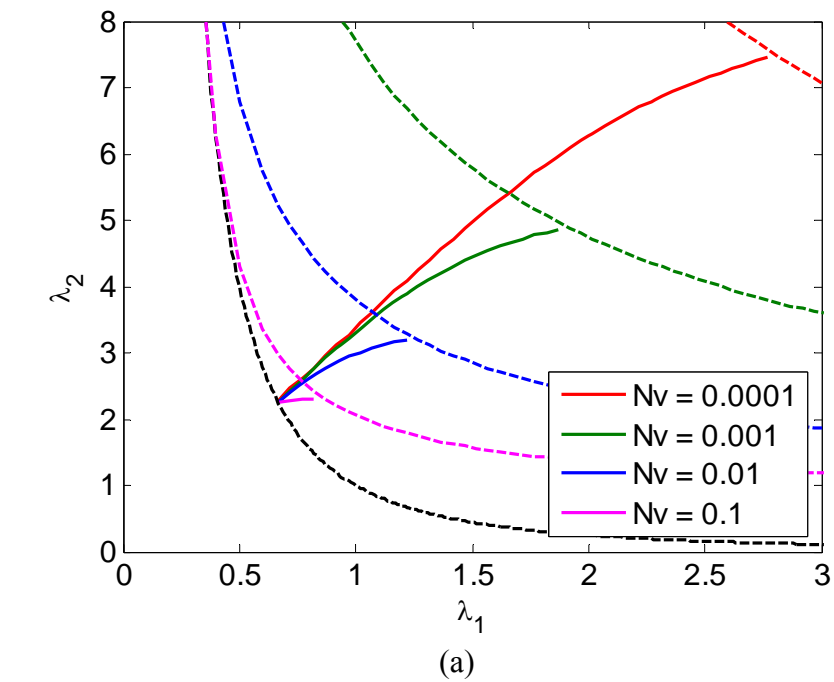


Figure 4.6: (a) Critical swelling ratio, and (b) critical in-plane true stress ($\sigma_{11} = \sigma_{33}$) for hydrogels under equi-biaxial pre-stretch ($\lambda_1 = \lambda_3$), with $\chi = 0.1$.

at point E takes a role of the minimum necessary pre-stretch to stabilize the swelling of a hydrogel layer. The critical in-plane pre-stretch (λ_1^*) is plotted in Fig. 4.7 as a function of $N\nu$ for fixed χ . The range of $N\nu$ presented in Fig. 4.7 is roughly in the order of 10kPa to 100MPa of the initial shear modulus of the polymer network at room temperature. The graph tells that as either $N\nu$ increases or χ decreases, the in-plane critical pre-stretch decreases. For very stiff hydrogels (high $N\nu$), very little swelling is expected. Then the critical pre-stretch (λ_1^*) approaches to the critical condition under pure mechanical compression at point B in Fig. 4.5. As a result, all curves in Fig. 4.7 converge to the

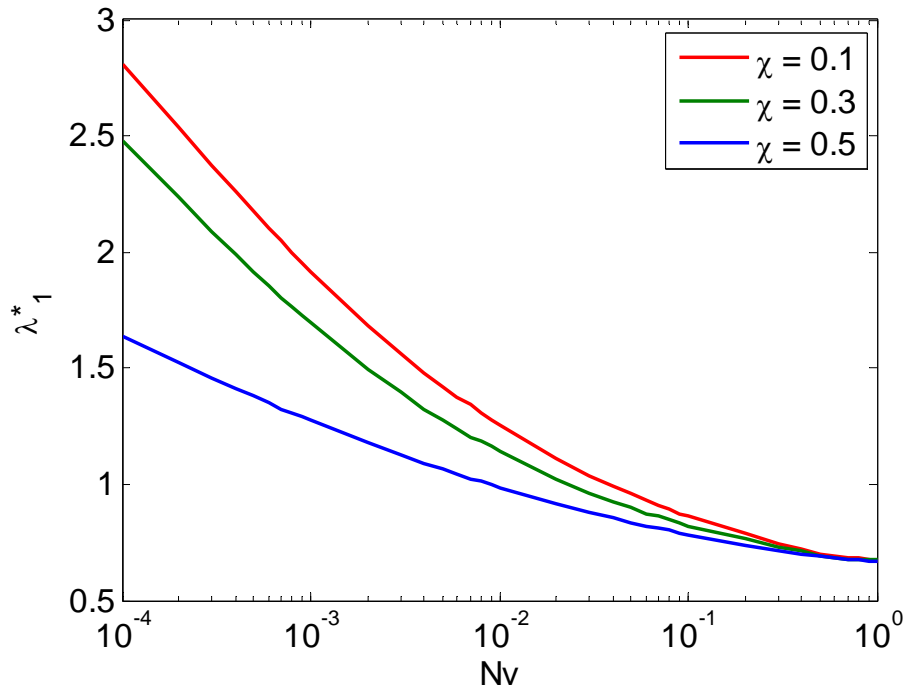


Figure 4.7: Critical pre-stretch at zero chemical potential (equilibrium vapor pressure) with respect to varying $N\nu$ for the equi-biaxial case.

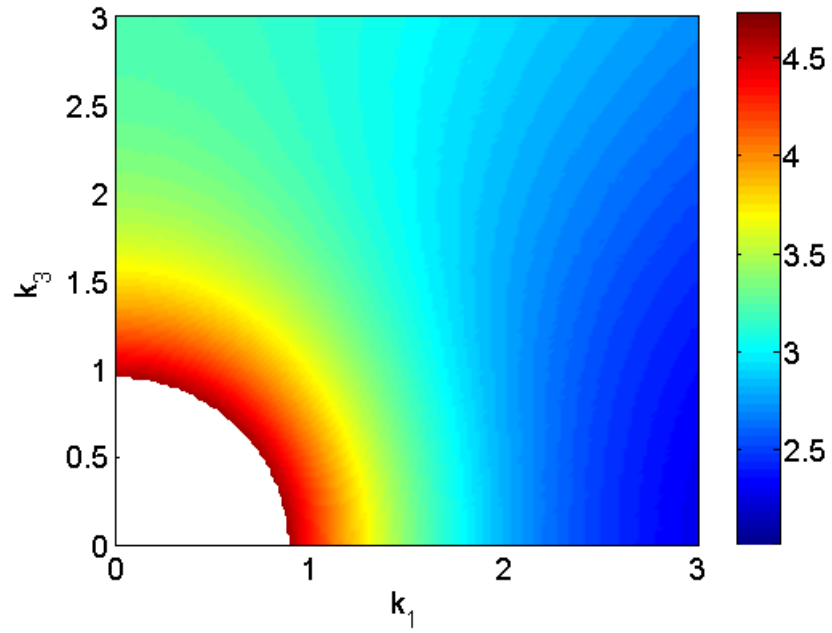
critical instability condition of incompressible rubbery material, $\lambda_1 = \lambda_B = 0.666$ as Nv increases.

4.4. EFFECT OF PLANE-STRAIN PRE-STRETCH ON SURFACE INSTABILITY

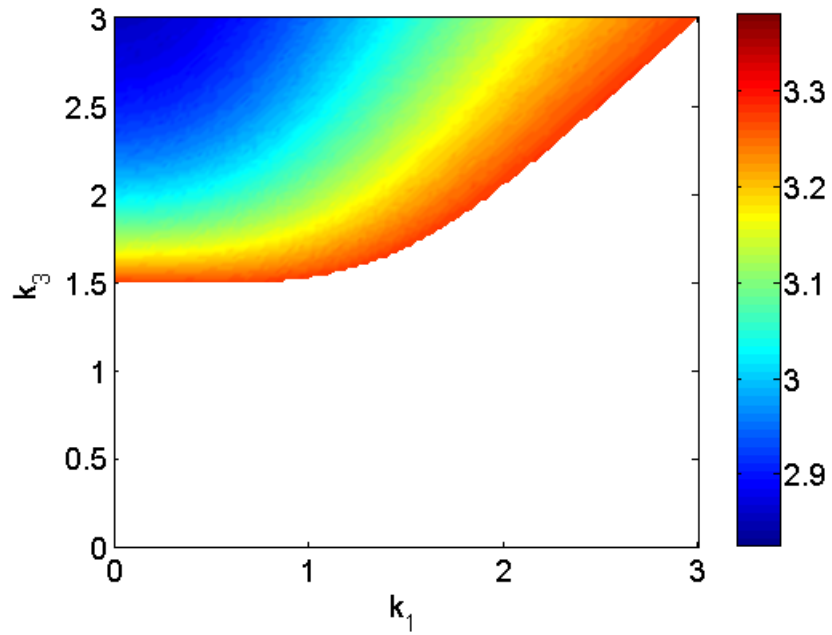
Just like the previous section, the contours of the critical out-of-plane swelling ratio (λ_2) vs. wavenumbers k_1 and k_3 are plotted for $\lambda_1 = 0.6$ and $\lambda_1 = 1.5$ in Fig. 4.8 (a) and (b). The first case represents $\lambda_1 < \lambda_3$ and compression is applied more in the x_1 direction. Similar to the equi-biaxial case, there is a stable region of oval shape for smaller wavenumbers, and, except for this region, the critical swelling ratio gradually decreases as the wavenumbers increase. But the critical swelling ratio varies with respect to the in-plane orientation and the lowest critical swelling ratio can be found along k_1 axis. As discussed in the equi-biaxial case, the direction of the lowest critical swelling ratio can be interpreted as the dominant instability direction.

The second case in Fig. 4.8 (b) represents $\lambda_1 > \lambda_3$. Since $\lambda_1 > 1$, the hydrogel is under less compression compared with the case in Fig. 4.8 (a). As a result, large portion of the area remains stable. The minimum critical swelling ratio can be found for large k_3 or in the x_3 direction, which indicates the favored direction of instability. From these two plane-strain cases, it can be said that the directional preference of the instability follows the maximum compression direction.

Based on this observation, we can simplify Eq. (4.41) with $k_3 = 0$ for $\lambda_1 < \lambda_3$ and $k_1 = 0$ for $\lambda_1 > \lambda_3$. Then Eq (4.47) is applicable for $\lambda_1 < \lambda_3$ with a different volume ratio $J_h = \lambda_1 \lambda_2$ and for $\lambda_1 > \lambda_3$,



(a)



(b)

Figure 4.8: Color contours of critical swelling ratio (λ_2) vs. wavenumbers (k_1 and k_3) for $N_V = 0.01$, $\chi = 0.1$, $\bar{p}_0 = 0.000023$; (a) $\lambda_1 = 0.6$, $\lambda_3 = 1$, (b) $\lambda_1 = 1.5$, $\lambda_3 = 1$.

$$\det(D_{mn}^{\infty}) = \begin{vmatrix} -\frac{\lambda_2}{\lambda_3} & \frac{\lambda_2}{\lambda_3} & -\sqrt{\frac{\lambda_3^2 + J_h \xi_h}{\lambda_2^2 + J_h \xi_h}} & \sqrt{\frac{\lambda_3^2 + J_h \xi_h}{\lambda_2^2 + J_h \xi_h}} \\ 1 & 1 & 1 & 1 \\ 2\lambda_2 e^{q_1 \lambda_2 h_0} & 0 & \frac{\lambda_2^2 + \lambda_3^2}{\lambda_2} e^{q_5 \lambda_2 h_0} & 0 \\ \frac{\lambda_2^2 + \lambda_3^2}{\lambda_3} e^{q_1 \lambda_2 h_0} & 0 & 2\lambda_2 \sqrt{\frac{\lambda_3^2 + J_h \xi_h}{\lambda_2^2 + J_h \xi_h}} e^{q_5 \lambda_2 h_0} & 0 \end{vmatrix}, \quad (4.48)$$

where λ_1 is included in J_h , ξ_h , and $q_{1,5}$. For the plane-strain case, $\lambda_3 = 1$.

The stability map for the plane-strain case for $Nv = 0.01$ and $\chi = 0.1$ is given in Fig. 4.9. Here, λ_3 is always fixed at 1, and the dry state limiting case is now

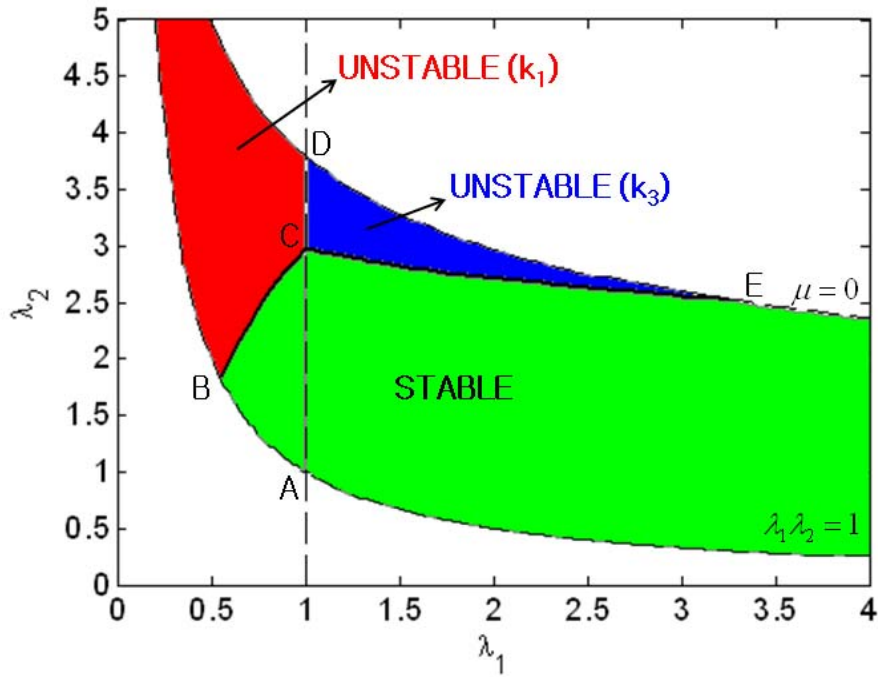
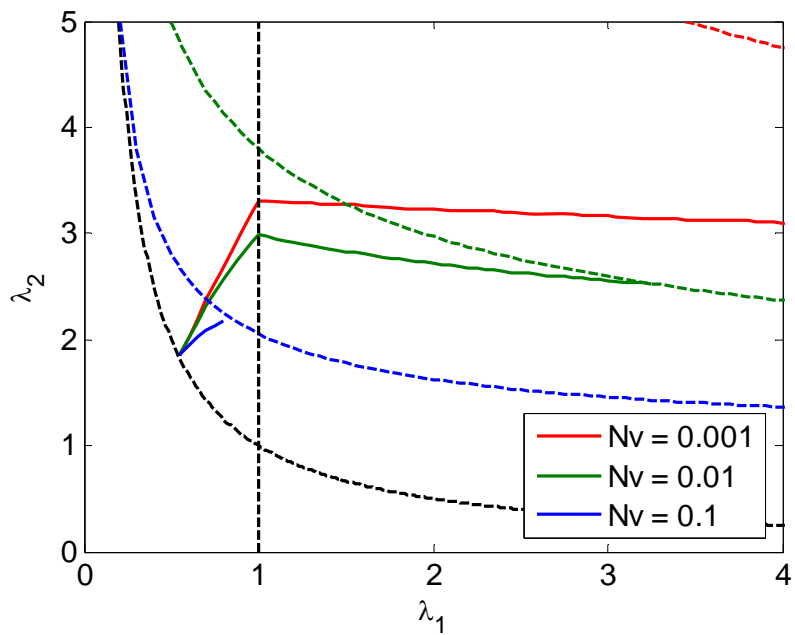


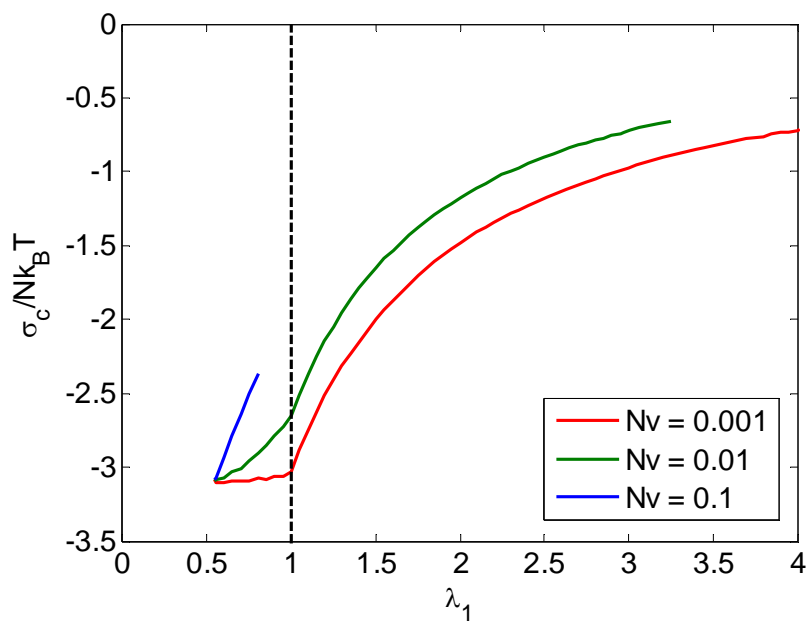
Figure 4.9: A stability map for hydrogels under plane strain pre-stretch ($Nv = 0.01$, $\chi = 0.1$).

$\lambda_1\lambda_2\lambda_3 = \lambda_1\lambda_2 = 1$ plotted as the lower bound in Fig. 4.9. We still have the zero chemical potential limiting case plotted as the upper bound in Fig. 4.9. The region of possible deformation is enclosed by these two limiting cases. The critical conditions in Eq. (4.46) and (4.47) divide the region of possible deformation into the unstable region and the stable region. The critical surface instability can be found along the in-plane direction with maximum compressive stress, which is x_1 for $\lambda_1 < 1$ and x_3 for $\lambda_1 > 1$. As a result, the area of deformation is divided into three: the unstable region along the x_1 direction with the perturbation wavenumber k_1 colored in red; the unstable region along the x_3 direction with the perturbation wavenumber k_3 colored in blue; and the stable region colored in green in Fig. 4.9.

Point A indicates a hydrogel at rest in the dry state. Path A to B is pure mechanical compression and the stretch at B is 0.544, identical to the critical condition of the plane-strain case of Biot's analysis [84]. Path B-C and C-E are the critical condition for the instability in the x_1 and x_3 directions, respectively. In detail, for a pre-stretch in between ($0.544 < \lambda_1 < 1$), the hydrogel layer becomes unstable in the x_1 direction at a critical swelling ratio (λ_2) between 1.84 at B and 2.98 at C, and for a pre-stretch in between ($1 < \lambda_1 < \lambda_E$), the hydrogel layer becomes unstable in the x_3 direction at a critical swelling ratio (λ_2) between 2.51 at E and 2.98 at C under the combined loading of mechanical compression and swelling for the given material properties. When the pre-stretch (λ_1) is greater than the critical pre-stretch (λ_E), a hydrogel swells homogeneously without surface instability.



(a)



(b)

Figure 4.10: (a) Critical swelling ratio, and (b) critical in-plane true stress ($\sigma_c = \sigma_{11}$ for $\lambda_1 < 1$, $\sigma_c = \sigma_{33}$ for $\lambda_1 > 1$) for hydrogels under plane-strain pre-stretch ($\lambda_3 = 1$), with $\chi=0.1$.

Path A-C-D indicates the region of direction independence since $\lambda_1 = \lambda_3 = 1$ and is identical with the Path A-C-D in Fig. 4.5 for the equi-biaxial state. Point E indicates the critical pre-stretch in the x_1 direction beyond which the swelling of a hydrogel is stable.

The critical swelling ratios and the corresponding critical in-plane true stresses are plotted for various $N\nu$ in Fig. 4.10 (a) and (b), respectively. Regardless of the material properties, the critical swelling in-plane stretch and the critical in-plane stress are 0.544 and $-3.08Nk_B T$, respectively. The critical stretch and the ratio of the critical stress and the initial shear modulus ($Nk_B T$) show material indifference under pure mechanical

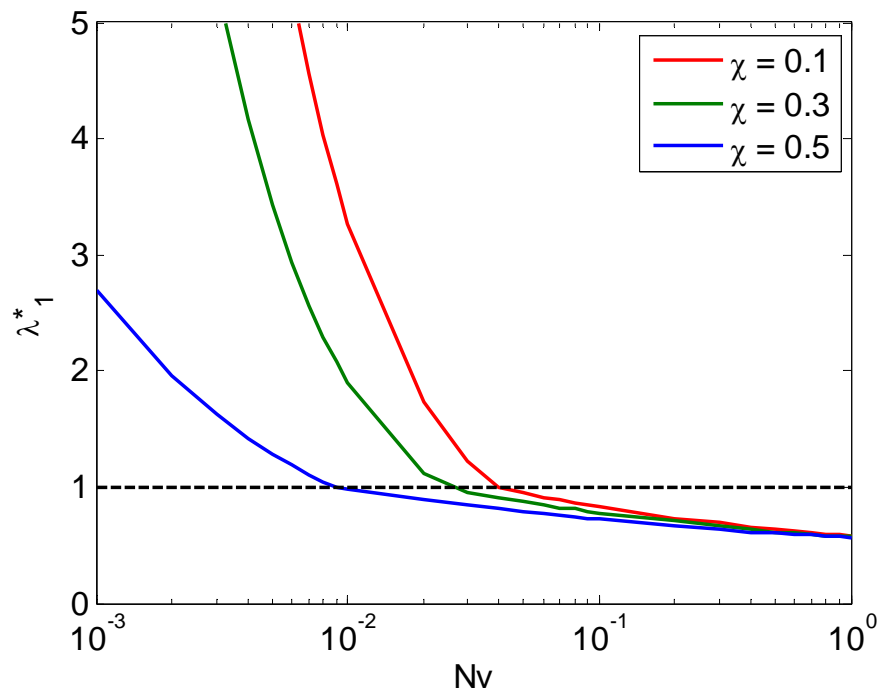


Figure 4.11: Critical pre-stretch at zero chemical potential (equilibrium vapor pressure) with respect to varying $N\nu$ for the plane-strain state.

compression, just as in Biot's analysis[84]. For the plane-strain case, sharp transition of the critical conditions is shown at $\lambda_1 = 1$ because of the instability direction change from x_1 to x_3 as λ_1 goes over 1 and the direction of the critical stress in Fig. 4.10 (b) also follows the instability direction.

The critical in-plane pre-stretches (point E in Fig. 4.9) are plotted in Fig. 4.11 as a function of Nv for fixed χ for the plane-strain state. The trend is that the critical in-plane stretches decrease as hydrogels get stiffer and reach the critical condition under pure mechanical compression, 0.544. A hydrogel will show stable swelling if it is initially pre-stretched by the amount larger than the pre-stretch values in Fig. 4.11. Below the critical value, a hydrogel will be unstable along the x_3 direction if $\lambda_1 > 1$ and the x_1 direction if $\lambda_1 < 1$. However, for stiffer hydrogels, since the critical in-plane pre-stretch(λ_1^*) is smaller than 1, surface instability in the x_1 direction can only be critical.

4.5. SUMMARY

In this chapter, the surface instability of hydrogel layers under biaxial pre-stretch immersed in a solvent is investigated. The swelling and deformation is determined by the chemical potential and the vapor pressure of the external solvent and the prescribed in-plane stretches. A mathematical model is derived for a hydrogel layer under general biaxial constraint and then two special cases are studied. One is the equi-biaxial case and the other is the plane-strain case. The homogeneous solutions of both cases are obtained. The generated in-plane compressive stresses are directly related to the in-plane stretches. Stress distribution due to the equi-biaxial pre-stretch is homogeneous in in-plane

directions showing transverse isotropy, but for plane-strain case, the less-stretched direction experiences more compressive stress which later is related to the directional preference of surface instability. Three-dimensional linear perturbation is introduced on top of the homogeneous solution and the equi-biaxial case and the plane-strain case are examined in detail. A stability map is constructed for the critical out-of-plane swelling ratio vs. pre-stretch. From the stability map, based on the amount of the pre-stretch, three different scenarios can be explained. The first scenario is surface instability under pure mechanical compression, which is identical to Biot's analysis on the surface instability of homogeneous half-space rubber under compression [84]. The second one is that a hydrogel is stable under pre-stretch but becomes unstable during swelling process. The critical swelling ratio is dependent on the amount of the pre-stretch. The last one is that a hydrogel remains stable until the end of the swelling process when the pre-stretch is large enough. From there, the critical pre-stretch can be found, beyond which no surface instability occurs. For the equi-biaxial case, any in-plane direction has the same possibility of surface instability due to transverse isotropy, whereas for the plane strain case, the surface instability favors the maximum compression direction. By considering the coupling effects of swelling due to an external solvent and the in-plane pre-stretch, the present analysis can serve as a unified theory for the surface instability under pure mechanical compression and the swell-induced surface instability of hydrogel.

Chapter 5

Effect of surface tension on swell-induced surface instability of hydrogels

In the previous chapters, swell-induced surface instability of hydrogels has been studied under the condition of the substrate constraint and the biaxial pre-stretch. While the long-wavelength instability modes are suppressed by the substrate effect, the short-wavelength modes are unaffected. As a result, the critical condition is predicted at the limit of an infinitely short wavelength. However, several experimental studies have reported characteristic wavelengths of swelling-induced surface patterns in gels [76, 81, 108]. Two possible mechanisms may lead to finite characteristic wavelengths for swell-induced surface instability in gels. For one, the characteristic wavelength may be dynamically determined by the swelling kinetics, similar to wrinkling of an elastic thin film on a viscoelastic substrate [109-111]. Second, the short-wavelength modes of surface instability may be suppressed by surface tension of the hydrogel, which together with the substrate effect would result in a finite wavelength for the surface instability. This chapter focuses on the effects of surface tension on both the critical condition and the characteristic wavelength.

5.1. EFFECT OF SURFACE TENSION ON HOMOGENEOUS SWELLING

Swelling of nanoscale hydrogel particles may be different from swelling of bulk hydrogel due to the effect of surface tension. Consider a spherical hydrogel particle of

radius a in the dry state. As the hydrogel swells, the surface area increases. Then the surface area in the dry state (S_0) and in the free-swollen state (S) is, respectively,

$$\begin{aligned} S_0 &= 4\pi a^2 \\ S &= 4\pi(\lambda a)^2, \end{aligned} \quad (5.1)$$

where λ is the swelling ratio.

The surface energy is proportional to the surface area (S) of the particle:

$$G_{surface} = S\gamma. \quad (5.2)$$

The total free energy is then

$$G = U(\lambda)V_0 + \lambda^2\gamma S_0 - \hat{\mu}CV_0 + (\lambda^3 - 1)pV_0 \quad (5.3)$$

where

$$V_0 = \frac{4}{3}\pi a^3, \quad (5.4)$$

$$C = \frac{\lambda^3 - 1}{\nu}. \quad (5.5)$$

Minimizing the free energy gives the equilibrium swelling ratio as:

$$\ln\left(1 - \frac{1}{\lambda^3}\right) + \frac{1}{\lambda^3} + \frac{\chi}{\lambda^6} + N\nu\left(\frac{1}{\lambda} - \frac{1}{\lambda^3}\right) + 2\frac{N\nu}{\lambda}\frac{L}{a} = \frac{\hat{\mu} - p\nu}{k_B T} \quad (5.6)$$

where $L = \frac{\gamma}{Nk_B T}$ is an intrinsic length scale defined by the ratio between the surface tension (γ) and the bulk shear modulus ($G_0 = Nk_B T$) of the polymer network. The above equation is identical to the isotropic, homogeneous free swelling case in Eqs. (2.52) and (2.53) except the last term on the left-hand side due to the surface tension term. For a

large particle, since L/a is negligibly small, the equilibrium swelling ratio is independent of the size. However, for a nanoscale hydrogel particle, the surface-to-volume ratio can be significant and the effect of surface tension increases as the ratio L/a increases.

To be specific, consider a hydrogel material with $Nv = 0.001$ and $\chi = 0.4$. Take the surface tension of water ($\gamma \sim 0.073 \text{ N/m}$) as a rough estimate for the hydrogel. Then $L \sim 0.53 \mu\text{m}$ at room temperature. Figure 5.1 plots the equilibrium swelling ratio ($\bar{\mu} = 0$) as a function of the characteristic size (a) of the hydrogel particle for various surface tension. The black dashed line is the homogeneous swelling ratio of a hydrogel particle without the surface tension effect. The surface tension effect clearly decreases the

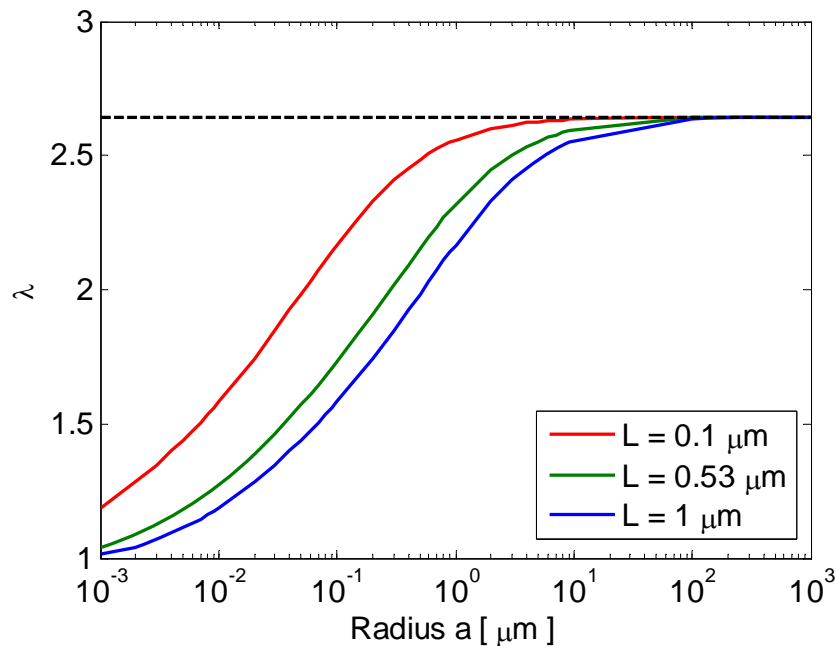


Figure 5.1: Equilibrium swelling ratio of a spherical hydrogel particle under surface tension effect.

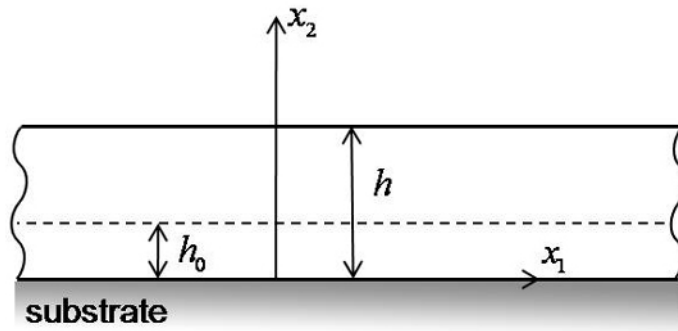
homogeneous swelling ratio as the characteristic size (a) decreases, and is diminished as the size increases. As a result, the swelling ratio approaches to that of the bulk hydrogel (negligible surface tension effect) as the radius a increases.

For a hydrogel layer, as the surface of the hydrogel layer is assumed to remain flat during the homogeneous swelling, the presence of a surface tension or surface energy does not have any effect on the one-dimensional (1-D) homogeneous swelling of the hydrogel, as considered in Section 3.1. On the other hand, surface tension plays a critical role in swell-induced surface instability of substrate-confined hydrogel layers, as discussed in the following sections.

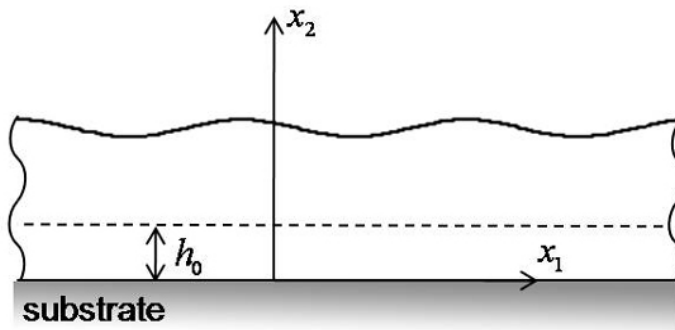
5.2. LINEAR PERTURBATION ANALYSIS

In Chapter 3, we performed a linear perturbation analysis of the homogeneous solution to predict swell-induced surface instability without considering the effect of surface tension. Following the same procedure, we present here a linear perturbation analysis with the effect of surface tension. As illustrated in Fig. 5.2, once the initially flat surface (Fig. 5.2 (a)) becomes unstable, it may evolve from a smooth undulation (Fig. 5.2 (b)) to form localized foldings and surface creases (Fig. 5.2 (c)).

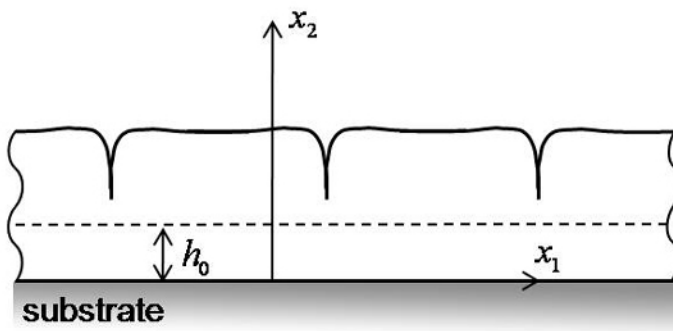
For a linear stability analysis, we can still use the perturbation and the corresponding deformation gradient given in Section 3.2. As a result, the nominal stresses in Eqs. (3.17), (3.19) – (3.23) and the equilibrium equations in Eqs. (3.24) and (3.25) hold. Thus, the solution in Eqs. (3.34) and (3.35) is still applicable with the same eigenvalues and eigenvectors in Eqs. (3.33) and (3.36).



(a)



(b)



(c)

Figure 5.2: Schematic illustrations of substrate-confined hydrogel layers: (a) homogeneous swelling; (b) onset of swell-induced surface instability; (c) formation of surface creases.

In addition, the stress field must satisfy the boundary conditions. Assume a liquid-like surface tension (γ) for the hydrogel. The perturbed surface has a curvature, $\kappa \approx \frac{\partial^2 u_2}{\partial x_1^2}$, to the first-order approximation. By the classical Young-Laplace equation, the normal stress at the surface of the hydrogel layer is balanced by the capillary pressure and the external pressure. In addition, due to the rotation of the surface normal direction, the nominal traction at the perturbed surface has a shear component. To the first order of perturbation, we have, at $x_2 = h = \lambda_h h_0$,

$$s_{22} = -p \left(1 + \frac{\partial u_1}{\partial x_1} \right) + \gamma \frac{\partial^2 u_2}{\partial x_1^2}, \quad (5.7)$$

$$s_{12} = p \frac{\partial u_2}{\partial x_1}. \quad (5.8)$$

At the hydrogel/substrate interface, we assume perfect bonding with zero displacements.

$$u_1 = u_2 = 0 \quad \text{at } x_2 = 0 \quad (5.9)$$

Expressing the boundary conditions in Eqs. (5.7) – (5.9) with the general solution in Eqs. (3.34) and (3.35) gives

$$\sum_{n=1}^4 D_{mn} A_n = 0, \quad (5.10)$$

where the coefficient matrix is given by

$$\mathbf{D} = \begin{bmatrix} 1 & 1 & 1 & 1 \\ -\lambda_h & \lambda_h & -\beta & \beta \\ (2\lambda_h + \lambda_h kL)e^{kh_0} & (2\lambda_h - \lambda_h kL)e^{-kh_0} & \left(\lambda_h + \frac{1}{\lambda_h} + \beta kL\right)e^{\beta kh} & \left(\lambda_h + \frac{1}{\lambda_h} - \beta kL\right)e^{-\beta kh} \\ \left(\lambda_h + \frac{1}{\lambda_h}\right)e^{kh_0} & -\left(\lambda_h + \frac{1}{\lambda_h}\right)e^{-kh_0} & 2\beta e^{\beta kh} & -2\beta e^{-\beta kh} \end{bmatrix} \quad (5.11)$$

The critical condition for swell-induced surface instability of the hydrogel layer is then obtained by setting the determinant of the matrix \mathbf{D} to be zero, namely

$$\text{Det}[\mathbf{D}] = f\left(kh_0, \lambda_h, \frac{h_0}{L}, N\nu, \chi\right) = 0. \quad (5.12)$$

As explained in Section 5.1, L is an intrinsic length scale defined by the ratio between the surface tension (γ) and the bulk shear modulus ($G_0 = Nk_B T$) of the polymer network. A similar length scale appeared in a critical condition that predicts the maximum pressure for cavitation in hydrogels [112]. Alternatively, a length scale can be defined with respect to the molecular volume of solvent, i.e., $L' = \frac{\mathcal{V}}{k_B T}$, which is independent of the polymer network. Take the surface tension of the hydrogel to be similar to that of water [112]. At room temperature, $\gamma \sim 0.073$ N/m and $\nu \sim 3 \times 10^{-29}$ m³, we have $L' \sim 0.53$ nm, while L can vary over several orders of magnitude (from nanometers to micrometers) depending on the value of $N\nu$. Here, we show that the presence of such a length scale leads to a thickness-dependent critical condition for swell-induced surface instability of substrate-confined hydrogel layers.

5.3. RESULTS AND DISCUSSIONS

The linear perturbation analysis predicts a critical condition, Eq. (5.12), for the onset of swell-induced surface instability of substrate-confined hydrogel layers. As plotted in Fig 5.3 (a), the predicted critical swelling ratio (λ_c) is a function of the normalized perturbation wavelength, $S = \frac{2\pi}{kh_0}$, depending on the initial layer thickness (h_0) as well as the material properties ($N\nu$ and χ) of the hydrogel. Figure 5.3 (b) plots the corresponding critical chemical potential (μ_c), which is related to the critical swelling ratio by Eq. (3.6). For these calculations, we assume a specific hydrogel system with $N\nu = 10^{-3}$, $\chi = 0.4$, $\bar{p}_0 = 2.3 \times 10^{-5}$, and $L = 0.53 \mu\text{m}$. For comparison, the thick dashed lines in Fig. 5.3 show the results from the previous analysis without the effect of surface tension, which are independent of the layer thickness. As expected, the surface tension tends to stabilize short-wavelength perturbations, leading to an increasingly larger critical swelling ratio as the wavelength decreases. Together with the effect of substrate confinement, which suppresses the long-wavelength perturbations, the critical swelling ratio has a minimum (λ_c^*) at an intermediate wavelength (S^*); both λ_c^* and S^* depend on the initial thickness (h_0) of the hydrogel layer.

Figure 5.4 (a) plots the minimum critical swelling ratio (λ_c^*) as a function of the initial thickness (h_0) of the hydrogel layer, and Fig. 5.4 (b) plots the corresponding wavelength (S^*h_0). To illustrate the effect of surface tension, the results are shown for different values of the length scale L . As a dimensionless quantity, the minimum critical

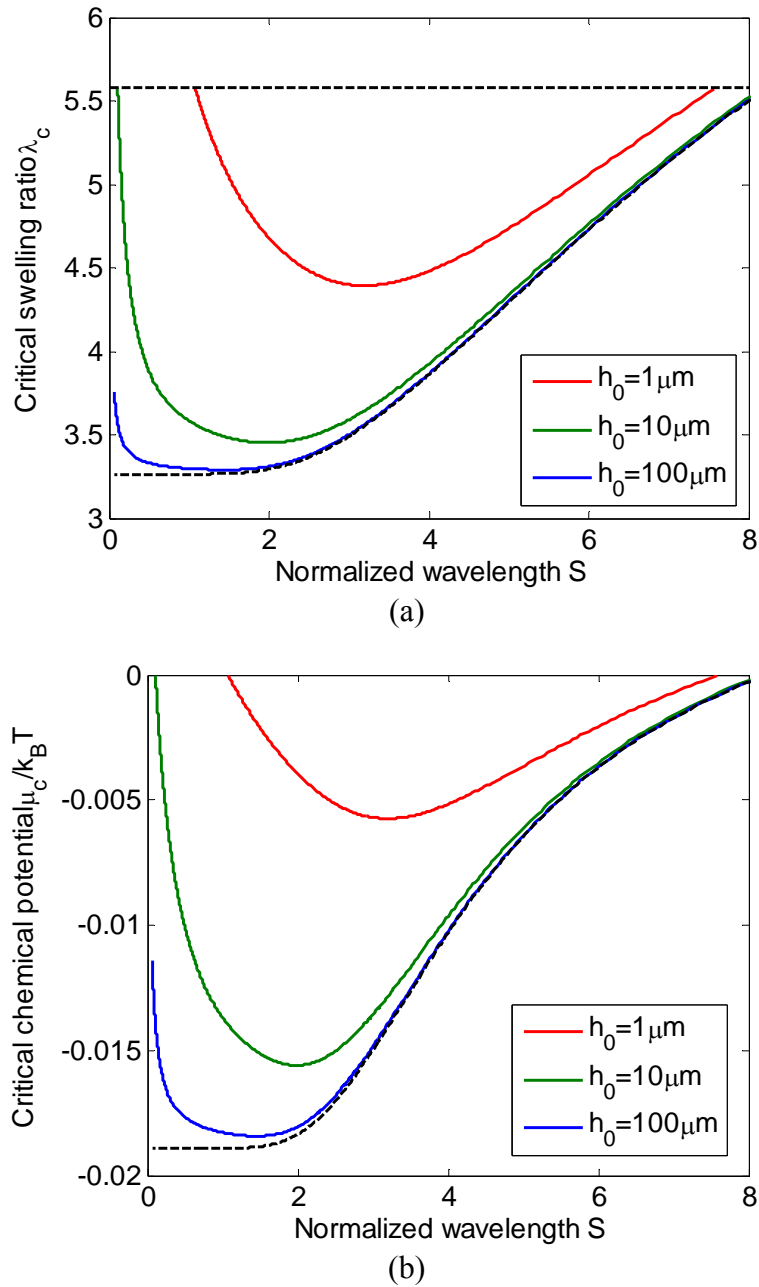


Figure 5.3: (a) Critical swelling ratio and (b) critical chemical potential, versus the perturbation wavelength for swell-induced surface instability of substrate-confined hydrogel layers with $Nv = 10^{-3}$, $\chi = 0.4$, and $L = 0.53 \mu\text{m}$. The thick dashed lines show the results without the effect of surface tension, and the thin dashed line in (a) indicates the homogeneous swelling ratio at the equilibrium.

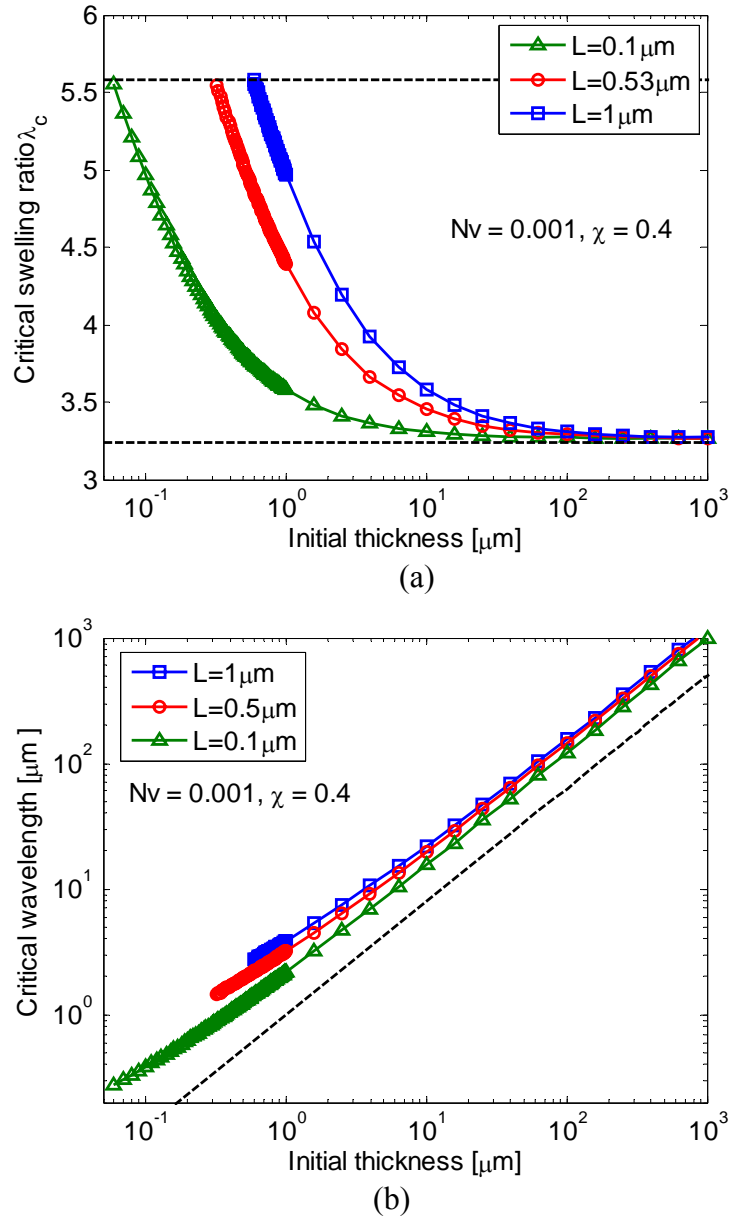


Figure 5.4: (a) The minimum critical swelling ratio and (b) the corresponding characteristic wavelength, versus the initial thickness of the substrate-confined hydrogel layers with $Nv = 10^{-3}$ and $\chi = 0.4$. The lower dashed line in (a) shows the thickness-independent critical swelling ratio without the effect of surface tension, and the upper dashed line indicates the homogeneous swelling ratio at the equilibrium. The dashed line in (b) shows the power-law scaling of the characteristic wavelength ($S^* h_0 \sim h_0^{0.9}$).

swelling ratio depends on the ratio between the two lengths, h_0/L . For a relatively thick hydrogel layer, the surface tension has negligible effect, and thus the critical swelling ratio approaches the previous prediction (the lower dashed line), which is independent of the layer thickness. As the layer thickness decreases, the effect of surface tension becomes increasingly important, and the critical swelling ratio increases until it reaches the equilibrium homogeneous swelling ratio (the upper dashed line) of the hydrogel layer at a critical thickness (h_c). For a thinner hydrogel layer ($h_0 < h_c$), the homogeneously swollen state is stable up to the equilibrium chemical potential ($\mu = 0$). Corresponding to the minimum critical swelling ratio, the characteristic wavelength (S^*h_0) decreases monotonically as the layer thickness decreases (Fig. 5.4 (b)), in qualitative agreement with experimental observations [76, 81, 108]. However, it is found that the characteristic wavelength as predicted here is not exactly proportional to the layer thickness. Instead, it appears to approximately follow a power-law scaling,

$$S^*h_0 \propto h_0^{1-\alpha}L^\alpha, \quad (5.12)$$

with a positive exponent α , over a wide range of the layer thickness. As shown by the dashed line in Fig. 5.4 (b), $\alpha \approx 0.1$ for $Nv = 10^{-3}$ and $\chi = 0.4$. The positive exponent (α) suggests that the characteristic wavelength increases as the surface tension of the hydrogel increases. Remarkably, the exponent is found to be insensitive to the other material properties of the hydrogel, with nearly identical value of α for different Nv and χ .

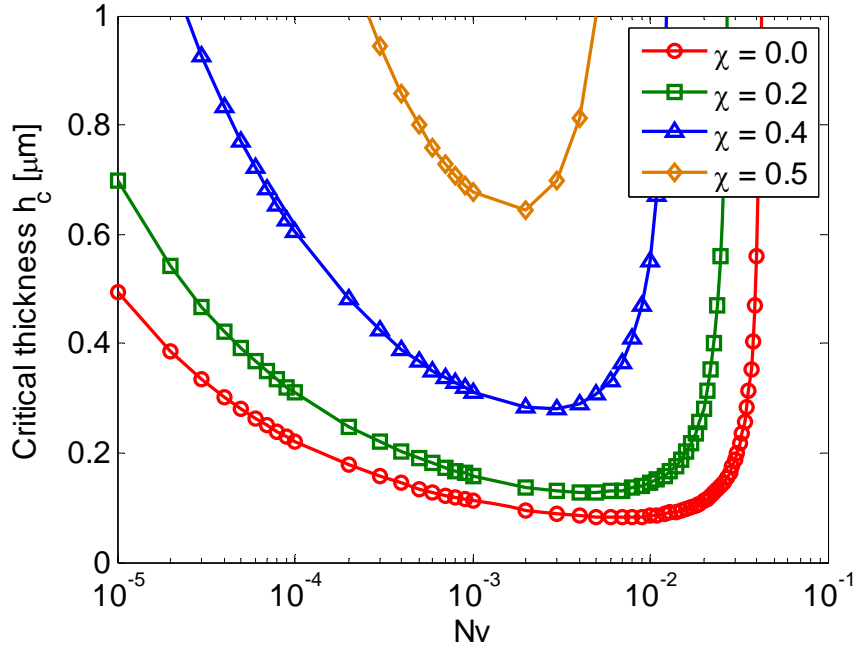


Figure 5.5: The critical thickness of substrate-confined hydrogel layers, predicted as a function of Nv for various values of χ . The length scale L' is assumed to be a constant ($L' = 0.53$ nm).

It is of interest to note that, while the surface tension has no effect on homogeneous swelling of a substrate-confined hydrogel layer, it plays a critical role in stabilizing thin hydrogel layers. In particular, the critical thickness (h_c) for a stable hydrogel layer is linearly proportional to the length scale L , which in turn is proportional to the surface tension γ . Similar critical thickness exists for surface instability of epitaxially grown crystal thin films [106]. Figure 5.5 plots the critical thickness (h_c) as a function of Nv for different values of χ , assuming a constant value for L' . The critical thickness depends on Nv through two competing factors. First, for a constant surface

tension (γ) and solvent molecular volume (v), because the length scale L decreases with increasing Nv , the critical thickness tends to decrease as well. On the other hand, since the polymer network of the hydrogel becomes increasingly stiff as Nv increases, the degree of swelling decreases. With less swelling, the hydrogel layer is more stable, and the critical thickness tends to increase. Consequently, the ratio between the critical thickness and the length scale, h_c/L , increases monotonically with increasing Nv . When Nv is relatively small, the effect of surface tension dominates, and the critical thickness decreases with increasing Nv . The trend is reversed as the elasticity of polymer network becomes significant with relatively large Nv . On the other hand, the dependence of the critical thickness on χ is simpler. As χ increases, the degree of swelling decreases and the critical thickness increases. For χ greater than a critical value ($\chi_c \sim 0.63$), the hydrogel layer remains stable at the equilibrium swelling state as shown in Fig. 3.4. For each χ less than the critical value, there exists a maximum value for Nv , beyond which the critical thickness is essentially infinity. This again is attributed to the limited degree of swelling, with which the hydrogel layer of any thickness would remain stable at the equilibrium state. Therefore, the critical condition for swell-induced surface instability of the substrate-confined hydrogel layer is largely determined by the three dimensionless parameters: h_0/L , Nv , and χ . As shown in Fig. 5.5, for typical values of Nv and χ , the critical thickness ranges between 100 nm and 1 μm . As shown in Fig. 5.3 (a), the critical thickness decreases as the length scale (L) decreases. When the hydrogel is immersed in water, the surface tension of the gel/water interface may be smaller than that of the

water/air interface [113], which then leads to a smaller length scale (L) and thus smaller critical thickness.

As noted in Chapter 3, the present stability analysis assumes a quasi-statically controlled swelling process, where the hydrogel layer swells homogeneously until the onset of surface instability. Consequently, the effect of swelling kinetics has been ignored. In experiments, when a hydrogel layer is immersed in a solvent, the transient state of swelling is typically inhomogeneous and the stability condition depends on the kinetics [6, 76]. Three scenarios may occur. First, the hydrogel layer remains stable and swells homogeneously up to the equilibrium state. This was observed for gels when the degree of swelling is relatively small [76]. Second, the hydrogel layer becomes unstable and develops surface creases during the transient swelling process. Eventually as the hydrogel layer reaches the equilibrium state, the surface creases disappear, and the equilibrium state of homogeneous swelling is stable [76]. Third, the surface creases develop and evolve during the transient process, and remain in the equilibrium state [81], suggesting that homogeneous swelling is unstable in the equilibrium state. The critical condition for surface instability as developed in the present study predicts whether the equilibrium state of homogeneous swelling is stable, but does not predict the onset of surface instability during the transient process. It is speculated that the critical swelling ratio for surface instability could be considerably lower for inhomogeneous swelling at the transient state. Detailed analysis on the effect of swelling kinetics is left for a separate study.

Another interesting point to note is the effect of temperature on the swell-induced surface instability of hydrogels. Within the present model, we see several possible effects that depend on temperature. First, in Eq. (3.6), the homogeneous swelling ratio depends on temperature through the normalized vapor pressure, $\bar{p}_0 = p_0 v / (k_B T)$, where p_0 itself is a function of temperature. In addition, the other material properties (N , χ , and ν) may all depend on temperature. Experimentally it has been observed that polymer gels may undergo continuous or discontinuous volume phase transition as the temperature changes [6], suggesting possible changes in the structure of the polymer network as well as the interaction between the polymer and solvent molecules. In the stability analysis, as the surface tension may depend on temperature, the predicted critical swelling ratio, the characteristic wavelength, and the critical layer thickness all depend on temperature. It is thus possible that a hydrogel layer is stable at one temperature but becomes unstable at a different temperature. In addition, it is well known that the kinetics of mass transport and swelling is typically sensitive to temperature. Therefore, the effect of temperature on swell-induced surface instability of hydrogels is in general complicated with the convergence of multiple effects on the material parameters and physical processes.

5.4. SUMMARY

This chapter presents a theoretical analysis of the swell-induced surface instability of substrate-confined hydrogel layers. In particular, the effect of surface tension is highlighted in comparison with a previous study in Chapter 3 that considered the effect of substrate confinement alone. With both surface tension and substrate confinement, we

show that the stability of a hydrogel layer depends on its initial thickness. A critical thickness is thus predicted, which is proportional to the surface tension and depends on the other material parameters of the hydrogel. The onset of surface instability is predicted at a characteristic wavelength with the minimum critical swelling ratio. A power-law scaling for the characteristic wavelength is obtained. The minimum critical swelling ratio decreases as the layer thickness increases, depending on the ratio between the two length scales (h_0/L) and approaching a constant at relatively large thickness.

Finally, we note that the linear perturbation analysis assumes a smooth surface perturbation in a homogeneously swollen hydrogel layer at the onset of surface instability. This is in the same spirit as Biot's analysis [84] on surface instability of a half-space rubber under mechanical compression, but different from the energetic analysis by Hong et al. [86]. As shown in the finite element simulation in Chapter 3, the smooth surface perturbation can subsequently evolve to form localized features such as grooves and creases (Fig. 5.1 (c)), as a result of nonlinear post-instability evolution. More studies, both theoretical and experimental, are needed to further elucidate the nonlinear process of surface evolution as well as the relationship between the two types of surface instability patterns.

Chapter 6

Swell-induced buckling of hydrogel lines

In Chapter 2, inhomogeneous swelling of substrate-supported hydrogel lines has been studied using two-dimensional (2D) finite-element models. The effect of substrate constraint has been discussed with respect to the aspect ratio of the cross section. The numerical simulations show swell-induced surface creasing for lines with large aspect ratio ($W/H > 10$). In an experimental study [78], swell-induced buckling was observed in polymer nanolines, as shown in Fig. 1.3 (b). By using three-dimensional (3D) finite-element models, this chapter studies swell-induced buckling of hydrogel lines.

6.1. EXPERIMENT

A brief introduction to the fabrication processes of the polymer nanolines and experimental observations is presented here. Figure 6.1 schematically shows the fabrication process [78]. A polymer solution was spin coated onto a silicon wafer. The film thickness was varied between 30 nm and 250 nm. The polymer film was then patterned by a direct-write electron-beam lithography technique. Electron-beam irradiation has been routinely used to cross-link bulk polymers. By using a focused electron-beam system, the exposed region of the polymer thin film was crosslinked while the non-irradiated regions remain uncrosslinked. The uncrosslinked polymer was then dissolved in water, leaving behind the patterned polymer lines. The crosslink density of the polymer lines can be tuned by varying the dwelling time of electron-beam exposure.

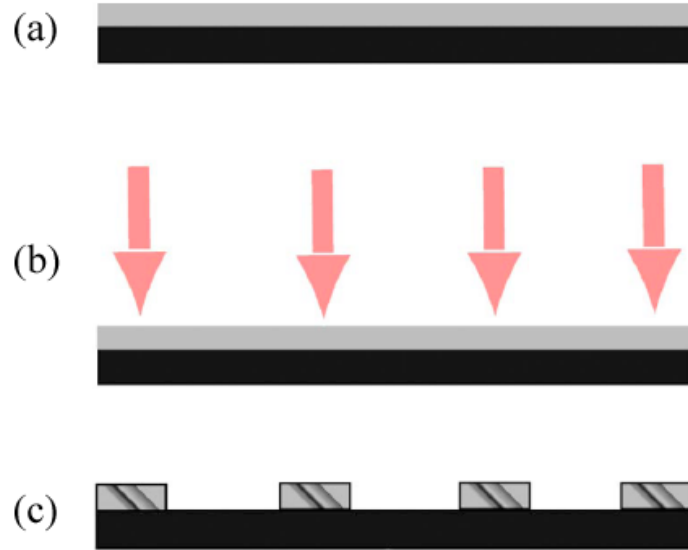


Figure 6.1: A fabrication process of hydrogel lines: (a) spin-coat, (b) e-beam exposure, (c) develop in water [78].

The polymer lines were then immersed in water until fully swollen. For the purpose of observation, the swollen lines were flash-dried using a nitrogen gun to preserve the morphology.

Figure 6.2 shows a set of swollen polymer nanolines, which were designed to study the effect of linewidth on swell-induced buckling. It was found that both the buckling wavelength and amplitude scale linearly with the linewidth. In addition, the buckling amplitude decreases with increasing crosslink density (ρ_c), while the buckling wavelength is independent of the crosslink density (ρ_c). The critical condition for the swell-induced buckling was not established experimentally. The selection of particular buckle wavelength was not well understood either.

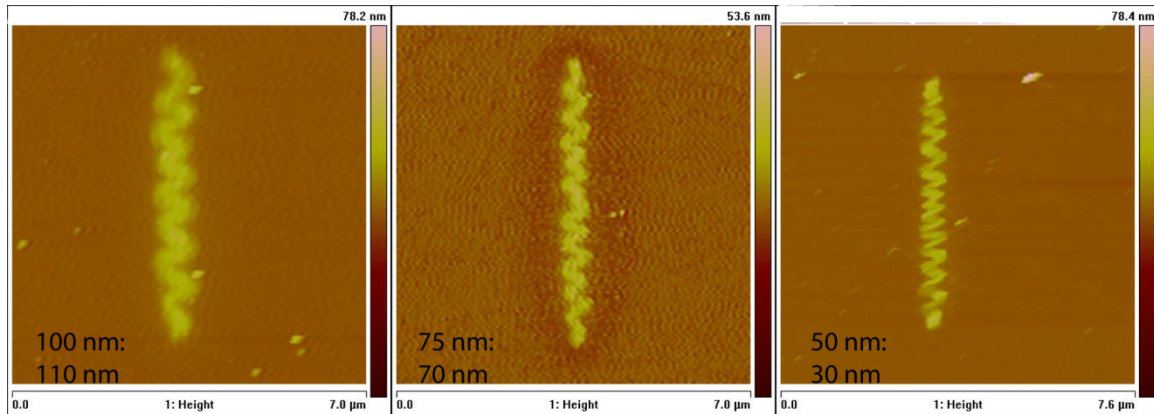


Figure 6.2: Atomic force micrographs of swollen polymer lines with the dry-state width:height dimensions as labeled in the panels. The lines were $5\ \mu\text{m}$ long before swelling. (Courtesy of Tirumala)

6.2. THREE-DIMENSIONAL FINITE-ELEMENT MODELS

Figure 6.3 shows a three-dimensional (3D) finite-element model for a hydrogel line. The 3D eight-node brick elements (C3D8) in ABAQUS are used for the hydrogel, while the substrate is modeled as a rigid surface. The same user-defined material subroutine (UMAT) as developed in Chapter 2 is used for the hydrogel. The bottom surface of the line is fixed, assuming no debonding from the substrate. Symmetric boundary conditions are applied at both ends of the line along the longitudinal direction, to eliminate the end effect and mimic an infinitely long line. The length L is arbitrarily selected to be several times of the buckle wavelength. The top and side faces of the hydrogel line are traction free. Contact between the side faces and the substrate is defined as well as the possible self-contact of the free surfaces.

The 3-D simulation procedure is similar to that depicted in Fig. 2.8 for the 2-D simulations. First, a homogeneous initial state is determined from the analytical solution for the 1-D swelling in the thickness direction, with an arbitrary initial swelling ratio (λ_0) at a finite chemical potential. Such an initial state comes with an initial pressure acting on the side faces. The first numerical step is then to relax the initial pressure while keeping the chemical potential constant. Next, the simulation continues by increasing the chemical potential till the equilibrium state ($\mu = 0$). To numerically trigger the buckling instability, a periodic imperfection of small amplitude is introduced by a cubic spline curve in the longitudinal direction of the line.

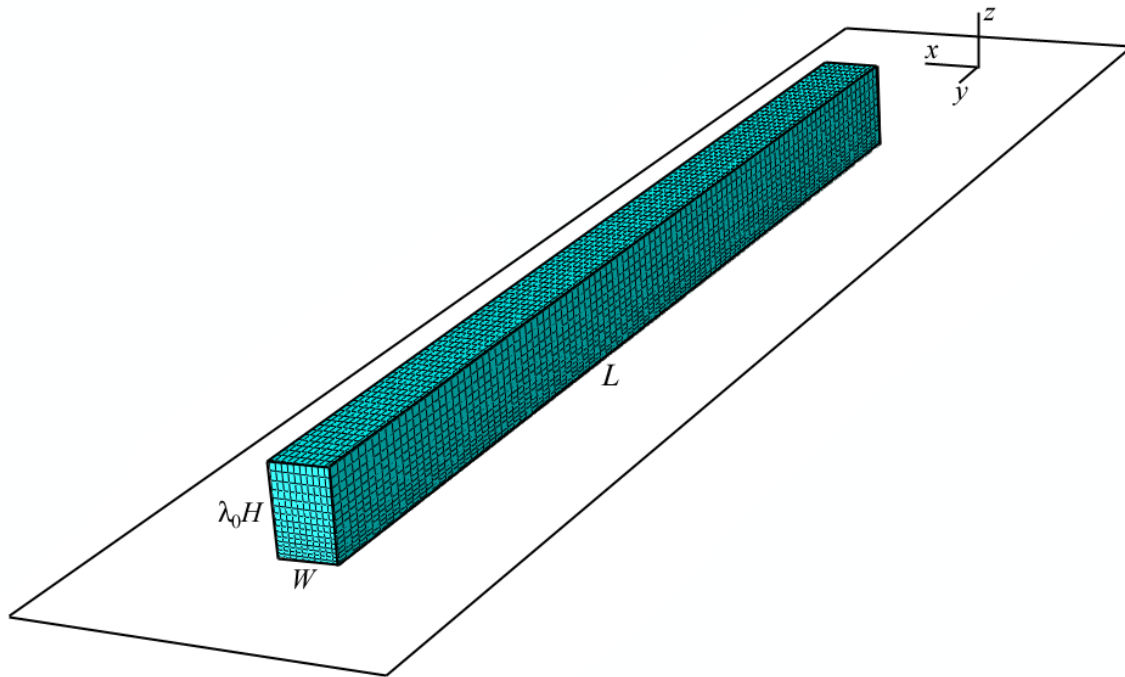


Figure 6.3: A three-dimensional finite element model of a hydrogel line attached to a rigid substrate (initially swollen state by λ_0).

6.3. RESULTS AND DISCUSSIONS

To illustrate the effects of material properties and geometry on swell-induced buckling, two sets of numerical simulations are performed. First, with identical line geometry, the material parameter (Nv) is varied in the finite-element model. The value of Nv is proportional to the crosslink density (ρ_c) of the polymer network. Figure 6.4 shows the swollen shapes for a set of hydrogel lines with $W/H = 1$ and $\chi = 0.55$. For $Nv = 0.1$,

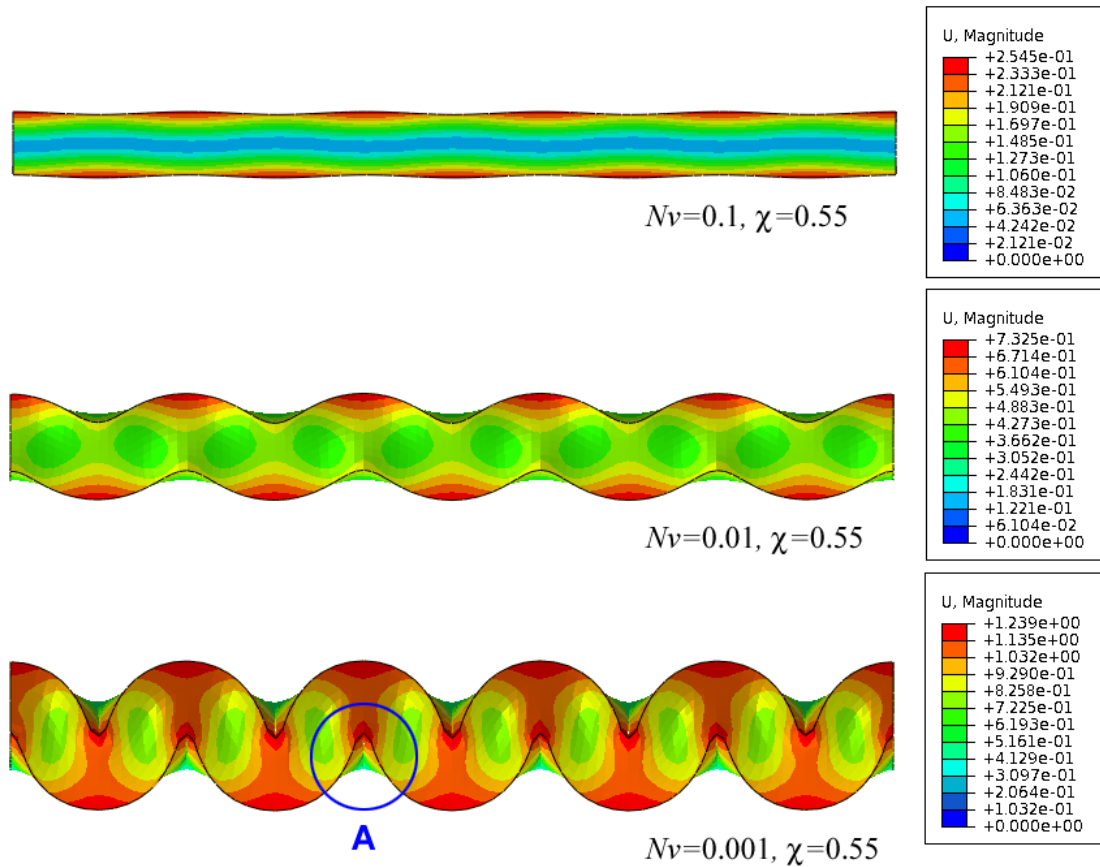


Figure 6.4: Buckling of hydrogel lines bonded to a rigid substrate for different Nv (width-to-height ratio 1). (A detail view of A is shown in Fig. 6.6)

the hydrogel is relatively stiff, with a low degree of swelling. As a result, the hydrogel line remains essentially straight, with no buckling. As $N\nu$ decreases, the hydrogel becomes softer and the degree of swelling increases. For $N\nu = 0.01$ and 0.001 , the hydrogel lines become buckled upon swelling. Note that the buckling wavelength in these simulations is arbitrarily fixed by the initial imperfection, which is four times the height (H). The physical criterion for the wavelength selection has not been established theoretically. Nevertheless, the present simulations show increasing buckle amplitude with decreasing $N\nu$, in qualitative agreement with experiments [78]. Figure 6.5 plots the buckling amplitude as a function of $N\nu$. As $N\nu$ decreases, the buckling amplitude

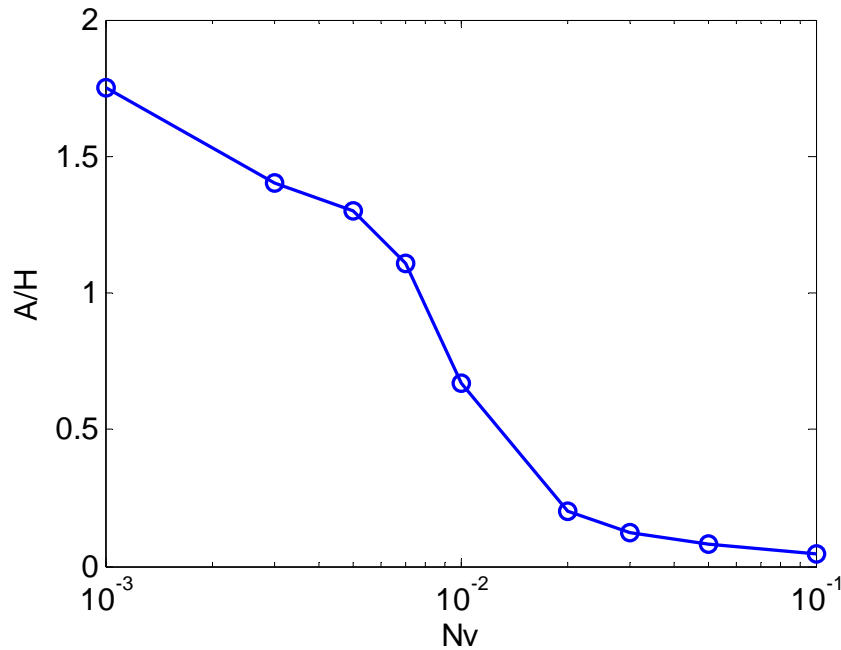


Figure 6.5: Normalized buckling amplitude as a function of $N\nu$. ($W/H = 1$, $\chi = 0.55$)

increases rapidly at a certain value of Nv , from which a critical value of Nv can be determined for swell-induced buckling of the hydrogel lines. In general, the critical value may be considered as a function of the buckle wavelength (S/H), the aspect ratio (W/H), and the parameter χ , namely

$$(Nv)_c = f(S/H, W/H, \chi) \quad (6.1)$$

Alternatively, for each hydrogel line, the buckling amplitude may be calculated as a function of the buckle wavelength, i.e.,

$$A/H = g(S/H; W/H, Nv, \chi) \quad (6.2)$$

A possible criterion for the wavelength selection may then be set up by maximizing the buckle amplitude. Such a criterion may be considered equivalent to maximizing the volume swelling ratio or to minimizing the free energy (or maximizing the entropy).

It is noted that, since the bottom surface of the hydrogel line is fixed, the swell-induced buckling deformation in general is more complicated than classical Euler buckling of a column. While the top surface appears to buckle laterally in the in-plane direction, it is also highly twisted in the out-of-plane direction. Due to relatively large deformation, the cross section of the line is highly distorted. Consequently, the kinematics of deformation is much more sophisticated than simple bending. In addition, significant swelling may lead to contact between the side faces and the substrate surface, as shown in Fig. 2.10. Swell-induced buckling can also lead to self-contact of the side faces, as shown in Fig. 6.6, where a crease-like fold is seen at the convex side of the buckled line.

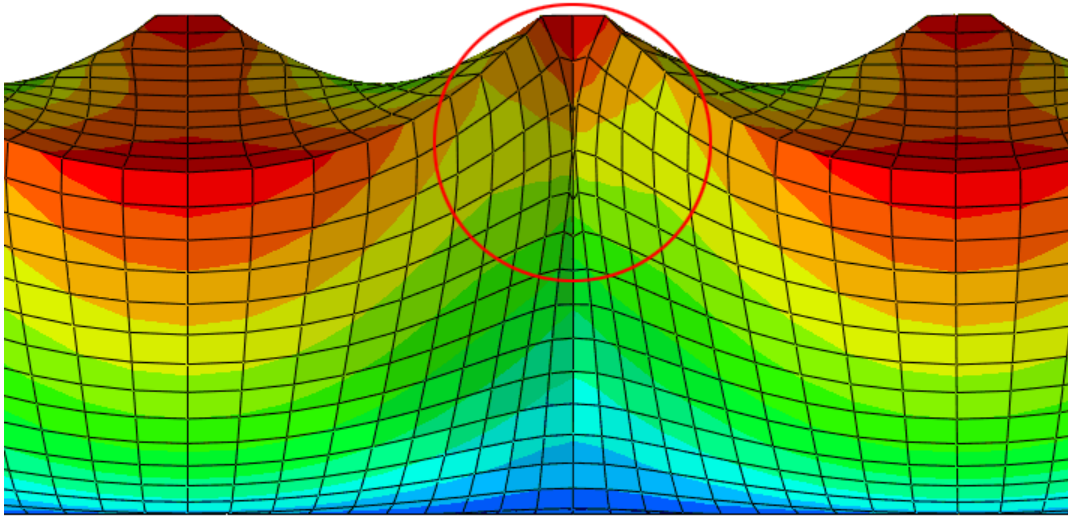


Figure 6.6: A crease-like fold evolution inside the circle, at A in Fig. 6.4 ($N\nu = 0.001$, $\chi=0.55$, $W/H = 1$).

For the second set of simulations, the material properties of the hydrogel are fixed as $N\nu = 0.01$ and $\chi = 0.55$, while the width-to-height aspect ratio (W/H) of the line is varied. As shown in Fig. 6.7, the buckle amplitude decreases as the aspect ratio (W/H) increases. For the case of $W/H = 4$, the line remains essentially straight with no buckling. The buckle amplitude as a function of aspect ratio is plotted for the given material properties in Fig. 6.8. Sudden increase of buckle amplitude indicates the critical aspect ratio (W/H). Thus, a critical aspect ratio for swell-induced buckling may be determined as a function of the material properties. Recall that a critical aspect ratio for swell-induced creasing has been suggested in Chapter 2. Together, it may be speculated that swell-induced buckling occurs for W/H less than a critical value and swell-induced creasing occurs for W/H greater than another critical value. In between of the two critical aspect ratios, the hydrogel line remains straight and stable. Yet another possible instability mode

is surface creasing due to compression in the longitudinal direction of the line, as opposed to the lateral compression considered in Chapter 2.

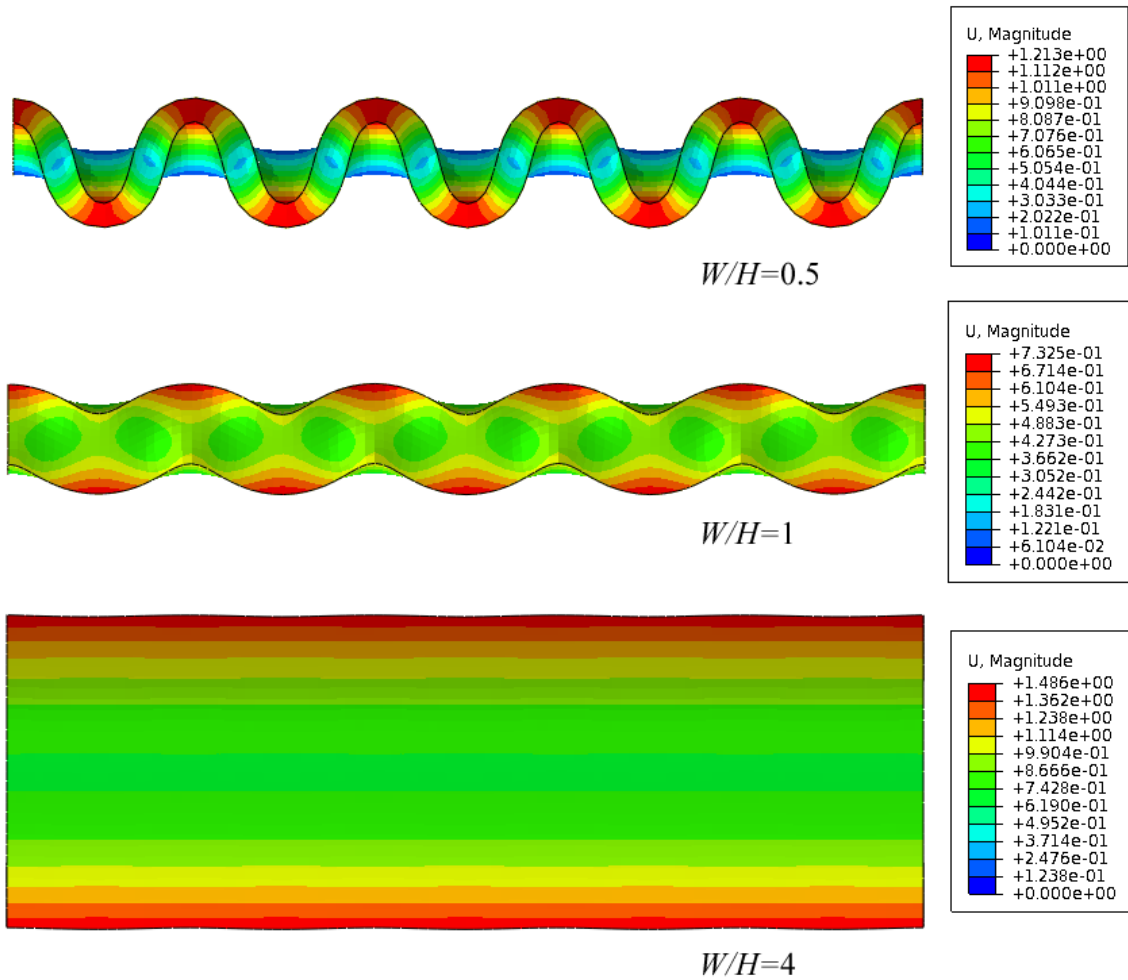


Figure 6.7: Buckling of hydrogel lines bonded to a rigid substrate for various width-to-height ratios ($N\nu = 0.01$ and $\chi = 0.55$).

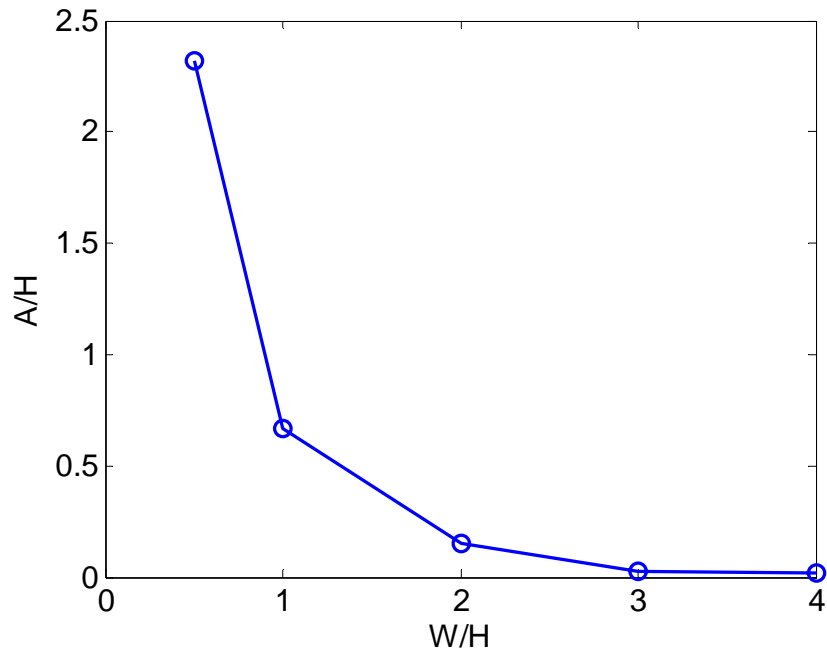


Figure 6.8: Normalized buckling amplitude as a function of W/H . ($N\nu = 0.01$, $\chi = 0.55$)

6.3. SUMMARY

This chapter presents a preliminary study on swell-induced buckling of supported hydrogel lines. By three-dimensional finite-element simulations, the effects of material properties and the geometry (width-to-height aspect ratio) are illustrated. However, further studies are needed to understand the critical condition and the selection of buckle wavelengths.

Chapter 7

Conclusions

The present study develops a general variational approach for equilibrium analysis of swelling deformation of hydrogels. The governing equations for mechanical and chemical equilibrium are obtained along with the boundary conditions. A specific material model is adopted based on a free energy density function. A finite element method for numerical analysis is developed, which allows anisotropic initial states for the study of swelling of hydrogels under constraints. As an example, inhomogeneous swelling of hydrogel lines attached to a rigid substrate is simulated, elucidating the effect of geometric constraint. Of particular interest is the formation of swelling-induced surface creases in the hydrogel lines beyond a critical aspect ratio.

A linear perturbation analysis is performed in Chapter 3 for swelling deformation of a confined hydrogel layer on a rigid substrate, which provides a theoretical understanding on the critical condition for onset of swell-induced surface instability. The predicted critical condition depends on the two dimensionless material parameters (Nv and χ) of specific hydrogel systems. In particular, the critical swelling ratio varies between 2.5 and 3.4, in good agreement with experiments. Numerical simulations are presented to show the swelling process of a confined hydrogel layer, with evolution of an initial surface perturbation followed by formation of surface creases.

The effects of biaxial pre-stretch on swell-induced surface instability are analyzed in Chapter 4. Stability diagrams are constructed for the cases of equi-biaxial pre-stretch

and plane-strain pre-stretch, unifying swell-induced surface instability with mechanically induced surface instability in rubber. Critical pre-stretches are predicted to render stable homogeneous swelling.

Next, by considering the effects of surface tension in Chapter 5, the onset of surface instability is predicted at a characteristic wavelength. Both the critical swelling ratio and the characteristic wavelength depend on the initial thickness of the hydrogel layer as well as other material properties of the hydrogel. An approximate power-law scaling for the characteristic wavelength is suggested. It is found that the hydrogel layer becomes increasingly stable as the initial layer thickness decreases. A critical thickness is predicted, below which the hydrogel layer swells homogeneously and remains stable at the equilibrium state.

The theoretical and numerical method developed in the present study can be used to study a variety of complex swelling behavior of polymeric hydrogels. The theoretical framework may be extended to study deformation of hydrogels in response to various external stimuli (e.g., temperature, pH, etc.). While the present study has focused exclusively on equilibrium analysis, the transient processes of swelling may be studied by incorporating the kinetics of molecular transport within the same theoretical framework.

Swell-induced surface instability has been studied in this dissertation primarily by the method of linear perturbation analysis. Such surface instability places a fundamental limit on the degree of swelling for hydrogels without formation of undesirable surface features in applications such as cell culture and smart surface coatings. On the other hand, the physics of surface instability may be harnessed in the design of responsive "smart"

surfaces for novel applications. In both cases, theoretical understanding on the critical condition of surface instability as well as subsequent surface pattern evolution is essential. However, it remains a challenge to numerically simulate surface evolution with folding and creases beyond the linear regime. Furthermore, it is noted from experimental observations that the swelling kinetics may play an important role in the development of surface instability.

Other types of swelling induced instability have also been observed in hydrogels. A preliminary study on swell-induced buckling of supported hydrogel lines is presented in Chapter 6. The effects of material properties and the geometry (width-to-height aspect ratio) are illustrated. However, further studies are needed to understand the critical condition and the selection of buckle wavelength. The competition between buckling and surface creasing is also an interesting topic for future studies.

Appendix A. ABAQUS User subroutines - UMAT and SIGNI

```

=====
C
C   User defined material subroutine
C   for gel with Flory-Huggins free-energy function
C   to be used in Abaqus Standard
C   Formulated and written by Min Kyoo Kang (last edited Jun. 15, 2010)
=====

      SUBROUTINE UMAT(STRESS,STATEV,DDSDDE,SSE,SPD,SCD,
1 RPL,DDSDDT,DRPLDE,DRPLDT,
2 STRAN,DSTRAN,TIME,DTIME,TEMP,DTEMP,PREDEF,DPRED,CMNAME,
3 NDI,NSHR,NTENS,NSTATV,PROPS,NPROPS,COORDS,DROT,PNEWDT,
4 CELENT,DFGRD0,DFGRD1,NOEL,NPT,LAYER,KSPT,KSTEP,KINC)
C
C   INCLUDE 'ABA_PARAM.INC'
C
      CHARACTER*80 CMNAME
      DIMENSION STRESS(NTENS),STATEV(NSTATV),
1 DDSDE(NTENS,NTENS),DDSDDT(NTENS),DRPLDE(NTENS),
2 STRAN(NTENS),DSTRAN(NTENS),TIME(2),PREDEF(1),DPRED(1),
3 PROPS(NPROPS),COORDS(3),DROT(3,3),DFGRD0(3,3),DFGRD1(3,3)

      DIMENSION DFGRD(3,3), dIdF(3,3), dJdF(3,3), FBAR(3,3), BBAR(3,3),
1 ZH(6,6)

      REAL(8) Nv, chi, lambdax0, lambday0, lambdaz0, mu_kT, AI, AJ, dUdI
1 ,dUdJ, C1, C2, dIdFF, dJdFF,lambdax0

      INTEGER matrix_size

      Nv = PROPS(1)
      chi = PROPS(2)
      lambdax0 = PROPS(3)
      lambday0 = PROPS(4)
      lambdaz0 = PROPS(5)

C   Chemical potential (mimicked by Temperature)
      mu_kT=TEMP

C   Computation of total deformation gradient from F_1
      DFGRD(1,1)=lambdax0*DFGRD1(1,1)
      DFGRD(1,2)=lambday0*DFGRD1(1,2)
      DFGRD(1,3)=lambdaz0*DFGRD1(1,3)
      DFGRD(2,1)=lambdax0*DFGRD1(2,1)
      DFGRD(2,2)=lambday0*DFGRD1(2,2)
      DFGRD(2,3)=lambdaz0*DFGRD1(2,3)
      DFGRD(3,1)=lambdax0*DFGRD1(3,1)
      DFGRD(3,2)=lambday0*DFGRD1(3,2)
      DFGRD(3,3)=lambdaz0*DFGRD1(3,3)

```

```

C      The first strain invariant
      AI=0.0d0
      do 31 ki=1,3
        do 32 kj=1,3
          AI=AI+DFGRD(ki,kj)**2.0d0
32      continue
31      continue

C      Determinant
      AJ=DFGRD(1,1)*DFGRD(2,2)*DFGRD(3,3)
      1 +DFGRD(1,3)*DFGRD(2,1)*DFGRD(3,2)
      1 +DFGRD(3,1)*DFGRD(1,2)*DFGRD(2,3)
      1 -DFGRD(1,3)*DFGRD(2,2)*DFGRD(3,1)
      1 -DFGRD(1,1)*DFGRD(2,3)*DFGRD(3,2)
      1 -DFGRD(2,1)*DFGRD(1,2)*DFGRD(3,3)

C      Deviatoric part of deformation gradient
      do 23 ki=1,3
        do 24 kj=1,3
          FBAR(ki,kj)=AJ**(-1.0d0/3.0d0)*DFGRD(ki,kj)
24      continue
23      continue

C      The Left Cauchy-Green Strain Tensor
      do 25 ki=1,3
        do 26 kj=1,3
          BBAR(ki,kj)=0.0d0
          do 30 kk=1,3
            BBAR(ki,kj)=BBAR(ki,kj)+FBAR(ki,kk)*FBAR(kj,kk)
30      continue
26      continue
25      continue

C      Derivatives of energy
      dUdI=1.0d0/2.0d0
      dUdJ=(1.0d0-Nv)/AJ-log(AJ/(AJ-1.0d0))+chi/AJ**2.0d0-mu_kT
      dUdJ=dUdJ/Nv

C      Coefficients
      C1=AJ**(-1.0d0/3.0d0)
      C2=-log(AJ/(AJ-1.0d0))+1.0d0/(AJ-1.0d0)-chi/AJ**2.0d0-mu_kT
      C2=C2/Nv

C      Derivatives of invariants
      do 27 ki=1,3
        do 28 kj=1,3
          dIdF(ki,kj)=2.0d0*DFGRD(ki,kj)
28      continue
27      continue
      dJdF(1,1)=DFGRD(2,2)*DFGRD(3,3)-DFGRD(2,3)*DFGRD(3,2)
      dJdF(1,2)=DFGRD(3,1)*DFGRD(2,3)-DFGRD(2,1)*DFGRD(3,3)

```

dJdF(1,3)=DFGRD(2,1)*DFGRD(3,2)-DFGRD(2,2)*DFGRD(3,1)

dJdF(2,1)=DFGRD(1,3)*DFGRD(3,2)-DFGRD(1,2)*DFGRD(3,3)

dJdF(2,2)=DFGRD(1,1)*DFGRD(3,3)-DFGRD(1,3)*DFGRD(3,1)

dJdF(2,3)=DFGRD(3,1)*DFGRD(1,2)-DFGRD(1,1)*DFGRD(3,2)

dJdF(3,1)=DFGRD(1,2)*DFGRD(2,3)-DFGRD(1,3)*DFGRD(2,2)

dJdF(3,2)=DFGRD(1,3)*DFGRD(2,1)-DFGRD(1,1)*DFGRD(2,3)

dJdF(3,3)=DFGRD(1,1)*DFGRD(2,2)-DFGRD(2,1)*DFGRD(1,2)

c Distinction between 3D & 2D element

if (NSHR .eq. 3) then

matrix_size=6

else

matrix_size=4

end if

CC

C Computation of true stress

do 5 iii=1,matrix_size

dIdFF=0.0d0

dJdFF=0.0d0

if (iii .le. 3) then

do 6 k=1,3

dIdFF=dIdFF+dIdF(iii,k)*DFGRD(iii,k)

dJdFF=dJdFF+dJdF(iii,k)*DFGRD(iii,k)

6

continue

else if (iii .eq. 4) then

do 7 k=1,3

dIdFF=dIdFF+dIdF(1,k)*DFGRD(2,k)

dJdFF=dJdFF+dJdF(1,k)*DFGRD(2,k)

7

continue

else if (iii .eq. 5) then

do 8 k=1,3

dIdFF=dIdFF+dIdF(1,k)*DFGRD(3,k)

dJdFF=dJdFF+dJdF(1,k)*DFGRD(3,k)

8

continue

else

do 9 k=1,3

dIdFF=dIdFF+dIdF(2,k)*DFGRD(3,k)

dJdFF=dJdFF+dJdF(2,k)*DFGRD(3,k)

9

continue

end if

STRESS(iii)=1.0d0/AJ*(dUdI*dIdFF+dUdJ*dJdFF)

5

continue

CC

CC

C Computation of tangent modulus (Jacobian)

C Initializaton of tangent modulus

do 10 ii=1,matrix_size

```

do 11 jj=1,matrix_size
  DDSDDDE(ii,jj)=0.0d0
11  continue
10  continue

C  Conversion of indexes between two tensor and four tensor
C  C(1,1)=DDSDDE(1,1) <=> i=j=n=l=1
C  C(1,2)=DDSDDE(1,2) <=> i=j=1,n=l=2
C  C(1,3)=DDSDDE(1,3) <=> i=j=1,n=l=3
C  C(1,4)=DDSDDE(1,4) <=> i=j=1,n=1,l=2
C  C(1,5)=DDSDDE(1,5) <=> i=j=1,n=1,l=3
C  C(1,6)=DDSDDE(1,6) <=> i=j=1,n=2,l=3
C  C(2,2)=DDSDDE(2,2) <=> i=j=2,n=l=2
C  C(2,3)=DDSDDE(2,3) <=> i=j=2,n=l=3
C  C(2,4)=DDSDDE(2,4) <=> i=j=2,n=1,l=2
C  C(2,5)=DDSDDE(2,5) <=> i=j=2,n=1,l=3
C  C(2,6)=DDSDDE(2,6) <=> i=j=2,n=2,l=3
C  C(3,3)=DDSDDE(3,3) <=> i=j=3,n=l=3
C  C(3,4)=DDSDDE(3,4) <=> i=j=3,n=1,l=2
C  C(3,5)=DDSDDE(3,5) <=> i=j=3,n=1,l=3
C  C(3,6)=DDSDDE(3,6) <=> i=j=3,n=2,l=3
C  C(4,4)=DDSDDE(4,4) <=> i=1,j=2,n=1,l=2
C  C(4,5)=DDSDDE(4,5) <=> i=1,j=2,n=1,l=3
C  C(4,6)=DDSDDE(4,4) <=> i=1,j=2,n=2,l=3
C  C(5,5)=DDSDDE(5,5) <=> i=1,j=3,n=1,l=3
C  C(5,6)=DDSDDE(5,6) <=> i=1,j=3,n=2,l=3
C  C(6,6)=DDSDDE(6,6) <=> i=2,j=3,n=2,l=3
do 12 ii=1,matrix_size
  do 13 jj=ii,matrix_size

    if (ii .eq. 1) then
      i=1
      j=1
    elseif (ii .eq. 2) then
      i=2
      j=2
    elseif (ii .eq. 3) then
      i=3
      j=3
    elseif (ii .eq. 4) then
      i=1
      j=2
    elseif (ii .eq. 5) then
      i=1
      j=3
    elseif (ii .eq. 6) then
      i=2
      j=3
    endif
    if (jj .eq. 1) then
      n=1
      l=1

```

```

elseif (jj .eq. 2) then
    n=2
    l=2
elseif (jj .eq. 3) then
    n=3
    l=3
elseif (jj .eq. 4) then
    n=1
    l=2
elseif (jj .eq. 5) then
    n=1
    l=3
elseif (jj .eq. 6) then
    n=2
    l=3
endif

ZH(ii,jj)=0.0d0
if (i .eq. n) ZH(ii,jj)=ZH(ii,jj)+BBAR(j,l)
if (j .eq. l) ZH(ii,jj)=ZH(ii,jj)+BBAR(i,n)
if (i .eq. l) ZH(ii,jj)=ZH(ii,jj)+BBAR(j,n)
if (j .eq. n) ZH(ii,jj)=ZH(ii,jj)+BBAR(i,l)

DDSDDE(ii,jj)=C1*0.5d0*ZH(ii,jj)

if ((i .eq. j) .and. (n .eq. l))
    DDSDDE(ii,jj)=DDSDDE(ii,jj)+C2
13     continue
12     continue

c     Generation of lower triangle matrix by using symmetry
do 18 ii=1,matrix_size
    do 19 jj=ii,matrix_size
        DDSDDE(jj,ii)=DDSDDE(ii,jj)
19     continue
18     continue

CCCCCCCCCCCCCCCCCCCCCCCCCCCCCCCCCCCCCCCCCCCCCCCCCCCCCCCCCCCC
    return
    end

C=====
C     User subroutine for initial stress definition
C=====

SUBROUTINE SIGINI(SIGMA,COORDS,NTENS,NCRDS,NOEL,NPT,LAYER,
1 KSPT,LREBAR,NAMES)
C
C     INCLUDE 'ABA_PARAM.INC'
C
C     DIMENSION SIGMA(NTENS),COORDS(NCRDS)
C     CHARACTER NAMES(2)*80

```

```

lambdax0 = 1.0d0
lambday0 = 2.0d0
lambdaz0 = 1.0d0

PII=1.0d0/(lambdax0*lambdaz0)*(lambday0-1.0d0/lambday0)

SIGMA = 0
SIGMA(1)=-((lambdax0-1.0d0/lambdax0)-PII*lambday0*lambdaz0)
1  /(lambday0*lambdaz0)
SIGMA(2)=0.0d0
SIGMA(3)=-((lambdaz0-1.0d0/lambdaz0)-PII*lambday0*lambdax0)
1  /(lambday0*lambdax0)

RETURN
END

```

Appendix B. Degenerated cases in 2-D perturbation analysis

For completeness, we present here the degenerated solutions to the eigenvalue problem in Eqs. (3.29) and (3.30). First, the eigenvalue problem is degenerated when

$$\xi_h = \frac{1}{\lambda_h} + \frac{1}{N\nu} \left(\frac{1}{\lambda_h - 1} - \frac{1}{\lambda_h} - \frac{2\chi}{\lambda_h^2} \right) = 0. \quad (\text{B.1})$$

It can be shown that this is only possible when $\chi > 0.5$. In this case, the two equilibrium equations in Eqs. (3.26) and (3.27) become uncoupled, and the eigenvalue problem becomes

$$\left[-k^2 + \lambda_h^2 q^2 \right] \bar{u}_1 = 0, \quad (\text{B.2})$$

$$\left[-k^2 + \lambda_h^2 q^2 \right] \bar{u}_2 = 0, \quad (\text{B.3})$$

which has two eigenvalues, $q_{1,2} = \pm \frac{k}{\lambda_h}$.

The complete solution then takes the form

$$\hat{u}_1(x_2; k) = A_1 \exp\left(\frac{kx_2}{\lambda_h}\right) + A_2 \exp\left(-\frac{kx_2}{\lambda_h}\right), \quad (\text{B.4})$$

$$\hat{u}_2(x_2; k) = A_3 \exp\left(\frac{kx_2}{\lambda_h}\right) + A_4 \exp\left(-\frac{kx_2}{\lambda_h}\right). \quad (\text{B.5})$$

Applying the boundary conditions in Eqs.(3.37) and (3.40), we obtain Eq. (3.45), but with the coefficient matrix as follows:

$$[D_{mn}] = \begin{bmatrix} 1 & 1 & 0 & 0 \\ 0 & 0 & 1 & 1 \\ -i\lambda_h e^{kh_0} & -i\lambda_h e^{-kh_0} & e^{kh_0} & -e^{-kh_0} \\ e^{kh_0} & -e^{-kh_0} & i\lambda_h e^{kh_0} & i\lambda_h e^{-kh_0} \end{bmatrix}. \quad (\text{B.6})$$

Setting the determinant of (B.6) to be zero, we have

$$\lambda_h = \coth(kh_0). \quad (\text{B.7})$$

Solving Eq. (B.7) gives the critical swelling ratio as a function of kh_0 , but only for the degenerated cases when Eq. (B.1) is satisfied.

A second degeneration of the eigenvalue problem occurs when

$$\beta = \sqrt{\frac{1 + \lambda_h \xi_h}{\lambda_h^2 + \lambda_h \xi_h}} = 0, \text{ or equivalently, when } \lambda_h \xi_h = -1. \text{ In this case, we have three}$$

eigenvalues instead of four in Eq. (3.33), namely

$$q_{1,2} = \pm \frac{k}{\lambda_h} \text{ and } q_3 = q_4 = 0. \quad (\text{B.8})$$

Consequently, the complete solution becomes

$$\hat{u}_1(x_2; k) = \sum_{n=1}^2 A_n \bar{u}_1^{(n)} \exp(q_n x_2) + A_3 + A_4 k x_2, \quad (\text{B.9})$$

$$\hat{u}_2(x_2; k) = \sum_{n=1}^2 A_n \bar{u}_2^{(n)} \exp(q_n x_2) - i A_4. \quad (\text{B.10})$$

where the eigenvectors for the first two eigenvalues are the same as in Eq. (3.36). Again, applying the boundary conditions in Eqs. (3.37) and (3.40), we obtain Eq. (3.45), but with the coefficient matrix as follows:

$$[D_{mn}] = \begin{bmatrix} 1 & 1 & 1 & 0 \\ -\lambda_h & \lambda_h & 0 & -1 \\ 2\lambda_h e^{kh_0} & 2\lambda_h e^{-kh_0} & \left(\lambda_h + \frac{1}{\lambda_h}\right) & (\lambda_h^2 + 1)kh_0 \\ \left(\lambda_h + \frac{1}{\lambda_h}\right)e^{kh_0} & -\left(\lambda_h + \frac{1}{\lambda_h}\right)e^{-kh_0} & 0 & 2 \end{bmatrix}. \quad (\text{B.11})$$

Setting the determinant of (B.11) gives the critical chemical potential for the second degenerated case. It is found that, for all material parameters considered in the present study, the critical swelling ratios for both the degenerated cases are greater than the maximum homogeneous swelling ratio at the equilibrium chemical potential. Therefore, the prediction of swell induced surface instability is unaffected by the degeneration in the eigenvalue problem.

Appendix C. Degenerated cases in 3-D perturbation analysis

Here, we present the degenerated solutions to the eigenvalue problem for the 3-D perturbation analysis in Eq. (4.33). First, the eigenvalue problem is de-generated when

$$\xi_h = \frac{1}{J_h} + \frac{1}{N\nu} \left(\frac{1}{J_h - 1} - \frac{1}{J_h} - \frac{2\chi}{J_h^2} \right) = 0. \quad (\text{C.1})$$

We can see that the first term is always positive and less than 1 for swelling. For ξ_h to be zero, the second term should be less than zero. This gives,

$$\frac{1}{J_h - 1} - \frac{1}{J_h} - \frac{2\chi}{J_h^2} = \frac{J_h - 2\chi(J_h - 1)}{J_h^2(J_h - 1)} < 0. \quad (\text{C.2})$$

The denominator is always positive for swelling. The numerator should be negative.

$$J_h - 2\chi(J_h - 1) < 0 \Rightarrow 2\chi > \frac{J_h}{J_h - 1} > 1. \quad (\text{C.3})$$

Therefore ξ_h can be zero only when $\chi > 0.5$. In this case, all equilibrium equations in Eq. (4.31) become uncoupled, which lead the following eigenvalue problem with only two eigenvalues.

$$\begin{aligned} \left[-(\lambda_1^2 k_1^2 + \lambda_3^2 k_3^2) + \lambda_2^2 q^2 \right] \bar{u}_1 &= 0 \\ \left[-(\lambda_1^2 k_1^2 + \lambda_3^2 k_3^2) + \lambda_2^2 q^2 \right] \bar{u}_2 &= 0, \\ \left[-(\lambda_1^2 k_1^2 + \lambda_3^2 k_3^2) + \lambda_2^2 q^2 \right] \bar{u}_3 &= 0 \end{aligned} \quad (\text{C.4})$$

with

$$q_{1,2} = \pm \frac{\sqrt{k_1^2 \lambda_1^2 + k_3^2 \lambda_3^2}}{\lambda_2}. \quad (\text{C.5})$$

The complete solution then takes the form

$$\begin{aligned}
\hat{u}_1(k_1, k_3, y) &= A_1 \exp(q_1 y) + A_2 \exp(q_2 y) \\
\hat{u}_2(k_1, k_3, y) &= A_3 \exp(q_1 y) + A_4 \exp(q_2 y). \\
\hat{u}_3(k_1, k_3, y) &= A_5 \exp(q_1 y) + A_6 \exp(q_2 y)
\end{aligned} \tag{C.6}$$

The second degenerated case can be found when

$$q_{5,6} = \pm \sqrt{\frac{k_1^2 \lambda_1^2 + k_3^2 \lambda_3^2 + J_h \xi_h (k_1^2 + k_3^2)}{\lambda_2^2 + J_h \xi_h}} = 0 \tag{C.7}$$

or equivalently,

$$\xi_h = -\frac{k_1^2 \lambda_1^2 + k_3^2 \lambda_3^2}{J_h (k_1^2 + k_3^2)}. \tag{C.8}$$

Then the corresponding eigenvalues are

$$q_{1,2} = \frac{(k_1^2 \lambda_1^2 + k_3^2 \lambda_3^2)^{1/2}}{\lambda_2}, \quad q_{3,4} = -q_{1,2} \quad \text{and} \quad q_{5,6} = 0. \tag{C.9}$$

Consequently, the complete solution becomes

$$\begin{aligned}
\hat{u}_1 &= \sum_{n=1}^4 A_n \bar{u}_1^{(n)} \exp(q_n y) + k_1 (A_5 + A_6 y) \\
\hat{u}_2 &= \sum_{n=1}^4 A_n \bar{u}_2^{(n)} \exp(q_n y) - i A_6 \\
\hat{u}_3 &= \sum_{n=1}^4 A_n \bar{u}_3^{(n)} \exp(q_n y) + k_3 (A_5 + A_6 y)
\end{aligned} \tag{C.10}$$

Since both degenerated cases are not significant in deciding the critical buckling conditions just like the 2-D degenerated cases presented in Appendix B, no further progress is necessary.

REFERENCES

1. Hirotsu, S., Hirokawa, Y., and Tanaka, T., *Volume phase transitions of ionized N isopropylacrylamide gels*. The Journal of Chemical Physics, 1987. **87**: p. 1392.
2. Tanaka, T., *Gels*. Scientific American, 1981. **244**(1): p. 124.
3. Tanaka, T., Nishio, I., Sun, S., and Ueno-Nishio, S., *Collapse of gels in an electric field*. Science, 1982. **218**: p. 467.
4. Suzuki, A. and Tanaka, T., *Phase transition in polymer gels induced by visible light*. Nature, 1990. **349**: p. 345.
5. Kuhn, W., Hargitay, B., Katchalsky, A., and Eisenberg, H., *Reversible dilation and contraction by changing the state of ionization of high-polymer acid networks*. Nature, 1950. **165**: p. 514.
6. Li, Y. and Tanaka, T., *Phase transitions of gels*. Annual Review of Materials Science, 1992. **22**(1): p. 243.
7. Tokarev, I. and Minko, S., *Stimuli-responsive hydrogel thin films*. Soft Matter, 2009. **5**(3): p. 511.
8. Galaev, I. and Mattiasson, B., *'Smart' polymers and what they could do in biotechnology and medicine*. Trends in Biotechnology, 1999. **17**(8): p. 335.
9. Jeong, B., Bae, Y., Lee, D., and Kim, S., *Biodegradable block copolymers as injectable drug-delivery systems*. Nature, 1997. **388**(6645): p. 860.

10. Peppas, N., Hilt, J., Khademhosseini, A., and Langer, R., *Hydrogels in biology and medicine: from molecular principles to bionanotechnology*. Advanced Materials, 2006. **18**(11): p. 1345.
11. Qiu, Y. and Park, K., *Environment-sensitive hydrogels for drug delivery*. Advanced Drug Delivery Reviews, 2001. **53**(3): p. 321.
12. Ulijn, R., Bibi, N., Jayawarna, V., Thornton, P., Todd, S., Mart, R., Smith, A., and Gough, J., *Bioresponsive hydrogels*. Materials Today, 2007. **10**(4): p. 40.
13. Beebe, D., Moore, J., Bauer, J., Yu, Q., Liu, R., Devadoss, C., and Jo, B., *Functional hydrogel structures for autonomous flow control inside microfluidic channels*. Nature, 2000. **404**: p. 588.
14. Konsta, A., Daoukaki, D., Pissis, P., and Vartzeli, K., *Hydration and conductivity studies of polymer-water interactions in polyacrylamide hydrogels*. Solid State Ionics, 1999. **125**(1-4): p. 235.
15. Pissis, P. and Kyritsis, A., *Electrical conductivity studies in hydrogels*. Solid State Ionics, 1997. **97**(1): p. 105.
16. Tang, Q., Wu, J., Sun, H., Fan, S., Hu, D., and Lin, J., *Superabsorbent conducting hydrogel from poly (acrylamide-aniline) with thermo-sensitivity and release properties*. Carbohydrate Polymers, 2008. **73**(3): p. 473.
17. Wu, J., Lan, Z., Wang, D., Hao, S., Lin, J., Wei, Y., Yin, S., and Sato, T., *Quasi-solid state dye-sensitized solar cells-based gel polymer electrolytes with poly (acrylamide)-poly (ethylene glycol) composite*. Journal of Photochemistry and Photobiology A: Chemistry, 2006. **181**(2-3): p. 333.

18. Lewandowski, A., Zajder, M., Frackowiak, E., and Beguin, F., *Supercapacitor based on activated carbon and polyethylene oxide-KOH-H₂O polymer electrolyte*. *Electrochimica Acta*, 2001. **46**(18): p. 2777.
19. Nohara, S., Wada, H., Furukawa, N., Inoue, H., Morita, M., and Iwakura, C., *Electrochemical characterization of new electric double layer capacitor with polymer hydrogel electrolyte*. *Electrochimica Acta*, 2003. **48**(6): p. 749.
20. Sun, X., Liu, G., Xie, J., Han, Y., and Kerr, J., *New gel polyelectrolytes for rechargeable lithium batteries*. *Solid State Ionics*, 2004. **175**(1-4): p. 713.
21. Berggren, M. and Richter-Dahlfors, A., *Organic bioelectronics*. *Advanced Materials*, 2007. **19**(20): p. 3201.
22. Bettinger, C. and Bao, Z., *Biomaterials-based organic electronic devices*. *Polymer International*, 2010. **59**: p. 563.
23. Dong, L., Agarwal, A., Beebe, D., and Jiang, H., *Adaptive liquid microlenses activated by stimuli-responsive hydrogels*. *Nature*, 2006. **442**(7102): p. 551.
24. Sidorenko, A., Krupenkin, T., Taylor, A., Fratzl, P., and Aizenberg, J., *Reversible switching of hydrogel-actuated nanostructures into complex micropatterns*. *Science*, 2007. **315**(5811): p. 487.
25. Guvendiren, M., Burdick, J., and Yang, S., *Kinetic study of swelling-induced surface pattern formation and ordering in hydrogel films with depth-wise crosslinking gradient*. *Soft Matter*, 2010. **6**(9): p. 2044.

26. Guvendiren, M., Yang, S., and Burdick, J., *Swelling-Induced Surface Patterns in Hydrogels with Gradient Crosslinking Density*. *Advanced Functional Materials*, 2009. **19**(19): p. 3038.
27. Gough, J., *A description of a property of caoutchouc*. *Proc Lit Phil Soc Manchester* (2nd ser), 1805. **1**: p. 288.
28. Kelvin, L., *Quarterly J Math*, 1857. **1**: p. 57.
29. Joule, J., *On some thermo-dynamic properties of solids*. *Philosophical Transactions of the Royal Society of London*, 1859. **149**: p. 91.
30. Staudinger, H., *Uber Polymerization (On Polymerization)*. *Ber. Dtsch. Chem. Ges*, 1920. **53**: p. 1073.
31. Meyer, K., Susich, G., and Valko, E., *The elastic properties of organic high polymers and their kinetic significance*. *Kolloid-Zeitschrift*, 1932. **59**: p. 208.
32. Busse, W., *The physical properties of elastic colloids*. *J. Phys. Chem*, 1932. **36**: p. 2862.
33. Kuhn, W., *Concerning the shape of thread shapes molecules in solution*. *Kolloid-Zeitschrift*, 1934. **68**: p. 2.
34. James, H. and Guth, E., *Theory of elastic properties of rubber*. *J. Chem. Phys*, 1943. **11**: p. 455.
35. Wall, F.T., *Statistical thermodynamics of rubber*. *J. Chem. Phys*, 1942. **10**: p. 132.
36. Flory, P. and Rehner, J., *Statistical mechanics of cross-linked polymer networks I. Rubberlike elasticity*. *J. Chem. Phys*, 1943. **11**: p. 512.

37. Treloar, L.R.G., *The elasticity of a network of long chain molecules (1 and 2)*. Trans. Faraday Soc, 1943. **39**: p. 36.
38. Treloar, L.R.G., *The Physics of Rubber Elasticity*. 1943,1958,1975, Oxford: Oxford University Press.
39. Flory, P., *Thermodynamics of high polymer solutions*. J. Chem. Phys, 1942. **10**: p. 51.
40. Huggins, M., *Some properties of long-chain compounds*. J. Phys. Chem, 1942. **46**: p. 151.
41. Flory, P. and Erman, B., *Theory of elasticity of polymer networks*. 3. Macromolecules, 1982. **15**(3): p. 800.
42. Flory, P.J., *Principles of Polymer Chemistry*. 1953, Ithaca, NY: Cornell University Press.
43. Arruda, E. and Boyce, M., *A three-dimensional constitutive model for the large stretch behavior of rubber elastic materials*. Journal of the Mechanics and Physics of Solids, 1993. **41**(2): p. 389.
44. Wu, P. and Van der Giessen, E., *On improved network models for rubber elasticity and their applications to orientation hardening in glassy polymers*. Journal of the Mechanics and Physics of Solids, 1993. **41**(3): p. 427.
45. Erman, B. and Mark, J., *Structures and Properties of Rubberlike Networks*. 1997: Oxford University Press, USA.

46. Elias-Zu iga, A. and Beatty, M., *Constitutive equations for amended non-Gaussian network models of rubber elasticity*. International Journal of Engineering Science, 2002. **40**(20): p. 2265.
47. Bechir, H., Chevalier, L., and Idjeri, M., *A three-dimensional network model for rubber elasticity: The effect of local entanglements constraints* International Journal of Engineering Science, 2010. **48**: p. 265.
48. Mooney, M., *A theory of large elastic deformation*. Journal of Applied Physics, 1940. **11**: p. 582.
49. Rivlin, R., *Large elastic deformations of isotropic materials. I. Fundamental concepts*. Philosophical Transactions of the Royal Society of London. Series A, Mathematical and Physical Sciences, 1948. **240**(822): p. 459.
50. Ogden, R., *Large deformation isotropic elasticity-on the correlation of theory and experiment for incompressible rubberlike solids*. Proceedings of the Royal Society of London. Series A, Mathematical and Physical Sciences, 1972. **326**: p. 565.
51. Yeoh, O., *Some forms of the strain energy function for rubber*. Rubber Chemistry and Technology, 1993. **66**(5): p. 754.
52. Gent, A., *A new constitutive relation for rubber*. Rubber Chemistry and Technology, 1996. **69**(1): p. 59.
53. Boyce, M. and Arruda, E., *Constitutive models of rubber elasticity: a review*, . Rubber Chemistry and Technology, 2000. **73**: p. 504.
54. Flory, P.J. and Rehner, J., *Statistical mechanics of cross-linked polymer networks II. Swelling*. J. Chem. Phys, 1943. **11**: p. 521.

55. Huang, Y., Szleifer, I., and Peppas, N., *A molecular theory of polymer gels*. *Macromolecules*, 2002. **35**(4): p. 1373.
56. Gibbs, J., *The scientific papers of J. Willard Gibbs*. 1878.
57. Hong, W., Liu, Z., and Suo, Z., *Inhomogeneous swelling of a gel in equilibrium with a solvent and mechanical load*. *International Journal of Solids and Structures*, 2009. **46**: p. 3282.
58. Tanaka, T., Hocker, L., and Benedek, G., *Spectrum of light scattered from a viscoelastic gel*. *The Journal of Chemical Physics*, 1973. **59**: p. 5151.
59. Tanaka, T. and Fillmore, D., *Kinetics of swelling of gels*. *The Journal of Chemical Physics*, 1979. **70**: p. 1214.
60. Durning, C. and Morman Jr, K., *Nonlinear swelling of polymer gels*. *The Journal of Chemical Physics*, 1993. **98**: p. 4275.
61. Barriere, B. and Leibler, L., *Kinetics of solvent absorption and permeation through a highly swellable elastomeric network*. *Journal of Polymer Science Part B: Polymer Physics*, 2003. **41**(2): p. 166.
62. Baek, S. and Srinivasa, A., *Diffusion of a fluid through an elastic solid undergoing large deformation*. *International Journal of Non-Linear Mechanics*, 2004. **39**(2): p. 201.
63. Hong, W., Zhao, X., Zhou, J., and Suo, Z., *A theory of coupled diffusion and large deformation in polymeric gels*. *Journal of the Mechanics and Physics of Solids*, 2008. **56**(5): p. 1779.

64. Doi, M., *Gel dynamics*. Journal of the Physica Society of Japan, 2009. **78**: p. 052001.
65. Duda, F., Souza, A., and Fried, E., *A theory for species migration in a finitely strained solid with application to polymer network swelling*. Journal of the Mechanics and Physics of Solids, 2010. **58**: p. 515.
66. Biot, M., *General theory of three-dimensional consolidation*. Journal of Applied Physics, 1941. **12**(2): p. 155.
67. Rice, J. and Cleary, M., *Some basic stress diffusion solutions for fluid-saturated elastic porous media with compressible constituents*. Rev. Geophys., 1976. **14**(2): p. 227.
68. Larche, F. and Cahn, J., *The interactions of composition and stress in crystalline solids*. Acta Metallurgica, 1985. **33**(3): p. 331.
69. Rajagopal, K., *Diffusion through polymeric solids undergoing large deformations*. Materials Science and Technology, 2003. **19**(9): p. 1175.
70. Birgeron, E., Li, H., and Wu, S., *Transient analysis of temperature-sensitive neutral hydrogels*. Journal of the Mechanics and Physics of Solids, 2008. **56**(2): p. 444.
71. Truesdell, C., *Rational Thermodynamics*. 1984, Springer Verlag, New York.
72. Dolbow, J., Fried, E., and Ji, H., *Chemically induced swelling of hydrogels*. Journal of the Mechanics and Physics of Solids, 2004. **52**(1): p. 51.

73. Ji, H., Mourad, H., Fried, E., and Dolbow, J., *Kinetics of thermally induced swelling of hydrogels*. International Journal of Solids and Structures, 2006. **43**(7-8): p. 1878.
74. Gurtin, M. and Struthers, A., *Multiphase thermomechanics with interfacial structure*. Archive for Rational Mechanics and Analysis, 1990. **112**(2): p. 97.
75. Southern, E. and Thomas, A., *Effect of constraints on the equilibrium swelling of rubber vulcanizates*. Journal of Polymer Science Part A General Papers, 1965. **3**(2): p. 641.
76. Tanaka, T., Sun, S., Hirokawa, Y., Katayama, S., Kucera, J., Hirose, Y., and Amiya, T., *Mechanical instability of gels at the phase transition*. Nature, 1987. **325**: p. 796.
77. Matsuo, E. and Tanaka, T., *Patterns in shrinking gels*. Nature, 1992. **358**: p. 482.
78. Tirumala, V., Divan, R., Ocola, L., and Mancini, D., *Direct-write e-beam patterning of stimuli-responsive hydrogel nanostructures*. Journal of Vacuum Science & Technology B: Microelectronics and Nanometer Structures, 2005. **23**: p. 3124.
79. Mora, T. and Boudaoud, A., *Buckling of swelling gels*. The European Physical Journal E, 2006. **20**(2): p. 119.
80. Sultan, E. and Boudaoud, A., *The buckling of a swollen thin gel layer bound to a compliant substrate*. Journal of Applied Mechanics, 2008. **75**: p. 051002.
81. Trujillo, V., Kim, J., and Hayward, R., *Creasing instability of surface-attached hydrogels*. Soft Matter, 2008. **4**(3): p. 564.

82. Zhang, J., Zhao, X., Suo, Z., and Jiang, H., *A finite element method for transient analysis of concurrent large deformation and mass transport in gels*. Journal of Applied Physics, 2009. **105**: p. 093522.
83. Tanaka, H., Tomita, H., Takasu, A., Hayashi, T., and Nishi, T., *Morphological and kinetic evolution of surface patterns in gels during the swelling process: Evidence of dynamic pattern ordering*. Physical Review Letters, 1992. **68**(18): p. 2794.
84. Biot, M., *Surface instability of rubber in compression*. Applied Science Research, Series A, 1963. **12**: p. 168.
85. Gent, A. and Cho, I., *Surface instabilities in compressed or bent rubber blocks*. Rubber Chemistry and Technology, 1999. **72**(2): p. 253.
86. Hong, W., Zhao, X., and Suo, Z., *Formation of creases on the surfaces of elastomers and gels*. Applied Physics Letters, 2009. **95**: p. 111901.
87. Onuki, A., *Theory of pattern formation in gels: Surface folding in highly compressible elastic bodies*. Physical Review A, 1989. **39**(11): p. 5932.
88. Suematsu, N., Sekimoto, K., and Kawasaki, K., *Three-dimensional computer modeling for pattern formation on the surface of an expanding polymer gel*. Physical Review A, 1990. **41**(10): p. 5751.
89. Ben Amar, M. and Ciarletta, P., *Swelling instability of surface-attached gels as a model of soft tissue growth under geometric constraints*. Journal of the Mechanics and Physics of Solids, 2010. **58**: p. 935.

90. Prigogine, I., *Introduction to Thermodynamics of Irreversible Process*. 3 ed. 1967: Wiley, New York.
91. Flory, P., *Statistical mechanics of swelling of network structures*. The Journal of Chemical Physics, 1950. **18**: p. 108.
92. Simo, J. and Pister, K., *Remarks on rate constitutive equations for finite deformation problems: computational implications*. Computer Methods in Applied Mechanics and Engineering, 1984. **46**(2): p. 201.
93. Bischoff, J., Arruda, E., and Grosh, K., *A new constitutive model for the compressibility of elastomers at finite deformations*. Rubber Chemistry and Technology, 2001. **74**(4): p. 541.
94. Ogden, R., *Volume changes associated with the deformation of rubber-like solids*. Journal of Mechanics Physics of Solids, 1976. **24**: p. 323.
95. Hermans, J., *Deformation and swelling of polymer networks containing comparatively long chains*. Transactions of the Faraday Society, 1947. **43**: p. 591.
96. Kuhn, W., Pasternak, R., and Kuhn, H., *Mechanische und optische Eigenschaften von gequollenem Kautschuk*. Helvetica Chimica Acta, 1947. **30**(6): p. 1705.
97. Huggins, M.L., *Solutions of long chain compounds*. Journal of Chemical Physics, 1941. **9**: p. 440.
98. Zhao, X., Hong, W., and Suo, Z., *Stretching and polarizing a dielectric gel immersed in a solvent*. International Journal of Solids and Structures, 2008. **45**(14-15): p. 4021.

99. Belytschko, T., Liu, W.K., and Moran, B., *Nonlinear Finite Elements for Continua and Structures*. 2000: John Wiley & Sons.
100. *ABAQUS (version 6.8)*. 2008, Providence, RI, USA: Dassault Systemes Simulia Corp.
101. Tanaka, H. and Sighuzi, T., *Surface-pattern evolution in a swelling gel under a geometrical constraint: Direct observation of fold structure and its coarsening dynamics*. Physical Review E, 1994. **49**(1): p. 39.
102. Hartschuh, R., Kisliuk, A., Novikov, V., Sokolov, A., Heyliger, P., Flannery, C., Johnson, W., Soles, C., and Wu, W., *Acoustic modes and elastic properties of polymeric nanostructures*. Applied Physics Letters, 2005. **87**: p. 173121.
103. Ghatak, A. and Das, A., *Kink instability of a highly deformable elastic cylinder*. Physical review letters, 2007. **99**(7): p. 076101.
104. Hohlfeld, E., *Creasing, point-bifurcations, and the spontaneous breakdown of scale-invariance*. 2008, HARVARD UNIVERSITY.
105. Gee, G., *The interaction between rubber and liquids. IX. The elastic behaviour of dry and swollen rubbers*. Transactions of the Faraday Society, 1946. **42**: p. 585.
106. Pang, Y. and Huang, R., *Nonlinear effect of stress and wetting on surface evolution of epitaxial thin films*. Physical Review B, 2006. **74**(7): p. 75413.
107. Yang, W. and Srolovitz, D., *Surface morphology evolution in stressed solids: surface diffusion controlled crack initiation*. Journal of the Mechanics and Physics of Solids, 1994. **42**(10): p. 1551.

108. Chan, E., Smith, E., Hayward, R., and Crosby, A., *Surface wrinkles for smart adhesion*. *Advanced Materials*, 2008. **20**(4): p. 711.
109. Huang, R., *Kinetic wrinkling of an elastic film on a viscoelastic substrate*. *Journal of the Mechanics and Physics of Solids*, 2005. **53**(1): p. 63.
110. Huang, R. and Im, S., *Dynamics of wrinkle growth and coarsening in stressed thin films*. *Physical Review E*, 2006. **74**(2): p. 26214.
111. Huang, R. and Suo, Z., *Wrinkling of a compressed elastic film on a viscous layer*. *Journal of Applied Physics*, 2002. **91**: p. 1135.
112. Kundu, S. and Crosby, A., *Cavitation and fracture behavior of polyacrylamide hydrogels*. *Soft Matter*, 2009. **5**(20): p. 3963.
113. Joanny, J., Johner, A., and Vilgis, T., *Gels at interfaces*. *The European Physical Journal E: Soft Matter and Biological Physics*, 2001. **6**(3): p. 201.

Vita

Min Kyoo Kang was born in Taegu, South Korea on September 9, 1976. He is a son of Jae Won Kang and Keun Sook Lee. In March 1995, He enrolled in Mechanical, Precision, Design, & Automotive Engineering at Hanyang University in Seoul, South Korea. He received his Bachelor of Science degree in the same department in February 2000. Later he received his Master of Science degree in Machine Design & Production Engineering also from Hanyang University in August 2002. He started his Ph. D. study in Mechanical Engineering at The University of Texas at Austin in September 2002. One year later, he transferred to Engineering Mechanics program and continued his Ph. D. study in Professor Rui Huang's group. During his graduate study, he worked as both teaching assistant and graduate research assistant in department of Aerospace Engineering & Engineering Mechanics.

E-mail address: minkyu0909@gmail.com

This dissertation was typed by Min Kyoo Kang.